

Copyright  
by  
Kimberly Ann Putkonen  
2015

THE DISSERTATION COMMITTEE FOR KIMBERLY ANN  
PUTKONEN CERTIFIES THAT THIS IS THE APPROVED  
VERSION OF THE FOLLOWING DISSERTATION:

**The Magnetic Anisotropy of a  
Three-Dimensional Honeycomb Iridate**

*Committee:*

---

John MARKERT, *Supervisor*

---

Ross McDONALD, *Co-Supervisor*

---

Chih-Kang SHIH

---

Alex DE LOZANNE

---

Brad RAMSHAW

THE MAGNETIC ANISOTROPY OF A  
THREE-DIMENSIONAL HONEYCOMB IRIDATE

BY

KIMBERLY ANN PUTKONEN, B.S.PHY.

**Dissertation**

Presented to the Faculty of the Graduate School  
of the University of Texas at Austin  
in Partial Fulfillment  
of the Requirements  
for the Degree of

**Doctor of Philosophy**

**The University of Texas at Austin**

**December 2015**

## *Acknowledgements*

I have the most appreciation for three advisors of my PhD research: Ross McDonald, Brad Ramshaw, and Arkady Shekhter, whose complementary scientific abilities have tremendously enriched my PhD experience. I can't even imagine a better learning environment for a graduate student. You all have different science questions and an even more unique "MO". Whether it's working through a problem using your intuition and every tool you have, your in-depth physics discussions, or the way you set up an experiment (paying attention to every single detail or taking the "just break things" approach), you all do things differently, inspiring me to think! Science-wise, I of course have the greatest respect for all of you, but what I find even more impressive is your character. You are all honest, ambitious, and selfless: there has never been a time that you wouldn't drop everything to help me and for that, I'm incredibly grateful. I don't really know how I got so lucky, but I couldn't hand-pick three people that I'd rather work with more. Your desire to understand and your excitement about physics have made this experience so much more enjoyable and rewarding than I ever could have imagined it to be. Ross - even though my eyes glaze over when you try to explain things to me and it actually pains me when you're right (which is pretty much always), I know that I couldn't ask for a better physicist to look up to - you always know what questions to ask and more importantly, how to answer them. I'm super thankful that I got an advisor I can trust and that I know has the best intentions for me. Somehow, you've even *managed* to create a very relaxed, but productive and fun atmosphere for a graduate student and I will miss everything about it. I just hope someone keeps you young (as I have tried) until I return! Brad - as a careful experimentalist, you set the bar high. Your persistence and dedication to making every experiment, not just work, but produce data of the highest-quality is inspiring and I feel privileged to learn from you each day. Somehow, you always

enter the room at just the right moment with a “never quit, never give up (and never depend on Ross)” attitude that I love! There are very few people that I could spend SO much time with and yet still be excited to see every morning at coffee time. You are an exceptional friend and I hope we always figure out a way to work closely together. Arkady - there is no doubt in my mind that this thesis could be greatly improved by your familiarity and in-depth knowledge of this subject, but I couldn't bear to get an edited version painted red with your comments *after* I submit. The months we spent working side by side on the iridate were by far the most valuable of my scientific career. From our first time experimenting with a new technique (ramping the magnet at 10 T/min, exactly as Ross instructed us to) to analyzing data (to death!) and writing and discussing together (not to mention your hour-long lectures twice daily on our commute), I have learned the most from you. Your patience and ability to explain physics, your unparalleled generosity, your physical insights, and your “charm” make you truly one of a kind!

I want to thank the Magnet Lab Pulsed Field Facility and the University of Texas, particularly my committee members Drs. John Markert, Ken Shih, and Alex DeLozanne. I would also like to express the sincerest appreciation to Drs. James Analytis, Nicholas Breznay, Fivos Drymiotis, Charles Mielke, Philip Moll, Albert Migliori, Neil Harrison, Jon Betts, James Smith, and Mun Chan for their guidance, support, and friendship. I am extremely grateful for the constant love and support from my parents Mariann, Dave, Nick, and Trish – thank you for being there for me *always*. Thank you, thank you, thank you Erik. You are always planning the next adventure and you constantly keep me smiling. I never thought life could be so fun, even when working on a PhD! Oh and last, but not least I can't forget to thank my dogs, Bear and Cub, for providing just the right amount of distraction during this entire process.

# The Magnetic Anisotropy of a Three-Dimensional Honeycomb Iridate

by

Kimberly Ann Putkonen, Ph.D.

UNIVERSITY OF TEXAS AT AUSTIN 2015

Supervisors: John Markert and Ross McDonald

One of the most sought-after, yet elusive ground states in condensed matter physics is the quantum spin liquid. The spin liquid is a strongly interacting spin system with exchange frustration and quantum fluctuations that prevent it from ordering magnetically as usual. Despite the theoretical introduction of this intriguing state of matter in the 1970's, it has lacked experimental backing until insights by Kitaev flourished in 2006. By considering a model honeycomb lattice with directionally dependent exchange anisotropy, he showed that a spin liquid ground state emerges as the limiting case of purely anisotropic exchange interactions. The design and availability of new strongly correlated materials has since lead to a persuasive experimental advance towards realization of this new state of matter, with the results presented herein at the forefront. In this thesis, one of the most promising spin liquid candidates,  $\text{Li}_2\text{IrO}_3$ , is studied in magnetic fields up to 100 tesla. A highly-sensitive torque magnetometry technique is developed to directly probe the magnetic anisotropy of  $\text{Li}_2\text{IrO}_3$  in both pulsed and DC magnets. The torque measurements confirm a transition to a complex magnetic order at  $T_N = 38$  K, in agreement with susceptibility data. At low magnetic fields, the ratio of the torque to the applied magnetic field has a linear response with an angle dependence that yields the principle components of magnetic anisotropy. At temperatures greater than  $\sim 150$  K, the observed magnetic anisotropy can be described by a  $g$ -factor

anisotropy that is constrained by the crystal structure, with the easy axis along the crystallographic  $c$  direction. At  $\sim 75$  K, the torque reveals a crossover to an exchange-dominated anisotropy, highlighted by an order of magnitude increase in the  $b$  component of susceptibility at temperatures within the magnetically ordered state. The temperature evolution of the magnetic anisotropy suggests that the extreme magnetic anisotropy observed at low temperatures must be driven by spin-anisotropy in the exchange interactions, as opposed to spatial anisotropy. This thorough investigation of the anisotropic susceptibility provided the first experimental evidence for highly spin-anisotropic exchange interactions to exist in  $\text{Li}_2\text{IrO}_3$  – the essential ingredient for realizing Kitaev’s quantum spin liquid ground state.

# Contents

<b>List of Figures</b>	<b>x</b>
<b>Abbreviations</b>	<b>xiii</b>
<b>Physical Constants</b>	<b>xv</b>
<b>Symbols</b>	<b>xvi</b>
<b>1 Introduction</b>	<b>1</b>
1.1 Progression of Quantum Materials Research . . . . .	2
1.2 Strongly Spin-Orbit Coupled Mott Insulators . . . . .	4
<b>2 Review of Magnetism</b>	<b>10</b>
2.1 Paramagnetism . . . . .	10
2.2 Exchange Interactions . . . . .	13
2.2.1 One electron in a solid . . . . .	15
2.2.2 The two electron problem . . . . .	17
2.3 The Ising Model . . . . .	21
2.4 The Heisenberg Model . . . . .	22
2.5 The Hubbard Model . . . . .	25
2.6 The Weiss Model of an Antiferromagnet . . . . .	26
2.7 Superexchange . . . . .	31
2.8 Spin-Anisotropic Exchange Interactions . . . . .	31
<b>3 The Honeycomb Iridates</b>	<b>34</b>
3.1 Background . . . . .	34
3.2 Three-Dimensional Honeycomb Structure of $\text{Li}_2\text{IrO}_3$ . . . . .	37
3.3 Crystal Field and Spin Orbit Effects . . . . .	45

<b>4</b>	<b>Experimental Techniques</b>	<b>53</b>
4.1	Pulsed Magnetic Fields . . . . .	53
4.1.1	Temperature Control . . . . .	56
4.1.2	Data Acquisition . . . . .	56
4.1.3	Field and Angle Control . . . . .	58
4.1.4	100 T Rotator Probe . . . . .	61
4.2	Torque Magnetometry . . . . .	65
4.3	SQUID Magnetometry . . . . .	71
4.4	Proximity Detector Oscillator (PDO) Measurements . . . . .	71
4.5	Electron Paramagnetic Resonance (EPR) . . . . .	73
<b>5</b>	<b>Torque Data Analysis</b>	<b>74</b>
5.1	Angle Dependent Torque Data . . . . .	75
<b>6</b>	<b>Magnetic Anisotropy of <math>\text{Li}_2\text{IrO}_3</math></b>	<b>96</b>
6.1	Temperature Dependent Magnetic Anisotropy . . . . .	98
6.2	High Temperature Magnetic Anisotropy . . . . .	103
6.3	Deviation from Curie-Weiss Behavior . . . . .	109
6.4	Low Temperature Magnetic Properties . . . . .	112
<b>7</b>	<b>High Magnetic Field Properties of <math>\text{Li}_2\text{IrO}_3</math></b>	<b>119</b>
7.1	Temperature Dependent Torque in the 65 T Pulsed Field Magnet . . . . .	119
7.2	Angle Dependent Torque in the 65 T Pulsed Field Magnet . . . . .	122
7.3	Angle Dependent Torque in the 100 T Pulsed Field Magnet . . . . .	126
7.4	Concluding Discussion and Unanswered Questions . . . . .	132
<b>8</b>	<b>Bose-Einstein Condensation in a Molecular Magnet</b>	<b>135</b>
8.1	Structural Properties of $[\text{Cu}(\text{pyz})(\text{gly})](\text{ClO}_4)$ . . . . .	135
8.2	Spin and Bosonic Representations of Spin Dimer Systems . . . . .	137
8.3	Temperature-Magnetic Field Phase Diagram . . . . .	139
8.4	EPR Results . . . . .	142
<b>A</b>	<b>Ir with a <math>5d^4</math> Electron Configuration</b>	<b>151</b>
<b>B</b>	<b>One Electron on the Ir <math>d</math>-shell in Empty Space</b>	<b>155</b>
	<b>Bibliography</b>	<b>160</b>

## List of Figures

1.1	Phase diagram for electronic materials . . . . .	5
1.2	Geometrically frustrated lattices . . . . .	8
2.1	Hybridized wavefunctions . . . . .	16
2.2	Two-electron energy spectrum for a diatomic pair . . . . .	20
2.3	The Weiss model of antiferromagnetism . . . . .	29
2.4	The Curie-Weiss dependence . . . . .	30
2.5	Exactly solvable Kitaev model . . . . .	32
3.1	Phase diagram of the Kitaev-Heisenberg model . . . . .	36
3.2	The magnetic susceptibility of polycrystalline $\text{Na}_2\text{IrO}_3$ and $\text{Li}_2\text{IrO}_3$ . . . . .	38
3.3	Three dimensional honeycomb structure of $\text{Li}_2\text{IrO}_3$ . . . . .	39
3.4	Octahedral environment of iridium-iridium bonds in $\text{Li}_2\text{IrO}_3$ . . . . .	40
3.5	Superexchange pathway between nearest neighbor iridium . . . . .	41
3.6	Orbital geometries for corner-sharing and edge-sharing octahedra . . . . .	42
3.7	The harmonic honeycomb structural family . . . . .	44
3.8	$\text{IrO}_6$ octahedral environment . . . . .	47
3.9	5 electrons on the Ir $d$ -shell . . . . .	52
4.1	Magnetic field profile for the 65 T short-pulse magnet . . . . .	54
4.2	Magnet field profile for the 100 T pulsed field magnet . . . . .	55
4.3	Data acquisition with synchronous lock-in processing . . . . .	58
4.4	Projection coil pickup voltage as a function of time . . . . .	60
4.5	Magnetic field profile as a function of axial distance in the 65 T pulsed magnets . . . . .	61
4.6	Cantilever view of 100 T rotator . . . . .	62
4.7	Rotating projection coil and thermometer view of 100 T rotator . . . . .	63
4.8	Side view of 100 T rotator . . . . .	64
4.9	Schematic of a magnetically anisotropic sample oriented on a cantilever in an external magnetic field . . . . .	66
4.10	Commercial silicon piezoresistive microcantilever . . . . .	69

4.11	Wheastone bridge circuit diagram . . . . .	70
4.12	Pictures of a PDO coil . . . . .	72
5.1	Orientation of crystallographic axes with respect to lever position and external field . . . . .	76
5.2	Raw torque signal of $\text{Li}_2\text{IrO}_3$ as a function of magnetic field . . . . .	77
5.3	Angular dependence of torque signal of $\text{Li}_2\text{IrO}_3$ for an arbitrary plane of rotation . . . . .	78
5.4	Angular dependence of torque divided by magnetic field . . . . .	79
5.5	Wheastone bridge circuit diagram . . . . .	80
5.6	Schematic of quadrants representing lever position and the expected sign of measured contributions to the signal . . . . .	82
5.7	Schematic of quadrants representing lever position and the expected sign of measured contributions to the signal . . . . .	84
5.8	Angle dependent magnetoresistance of the lever and the reference lever . . . . .	85
5.9	Schematic of the bridge circuit and the effect of each resistor on the measured output voltage . . . . .	86
5.10	Simulation of a magnetoresistive background added to a parabolic torque signal . . . . .	88
5.11	Slope of linear regime of $\tau/H$ as a function of angle . . . . .	90
5.12	$\tau/H$ as a function of field for the $a$ - $c$ plane of rotation . . . . .	91
5.13	Orientation of crystal for $a$ - $c$ plane of rotation, kink field and low field slope plotted as a function of angle . . . . .	92
5.14	$\tau/H$ as a function of field for the $a$ - $b$ plane of rotation . . . . .	93
5.15	Orientation of crystal for $a$ - $b$ plane of rotation, kink field and low field slope plotted as a function of angle . . . . .	94
6.1	Temperature dependence of magnetic anisotropy in the $a$ - $c$ plane . . . . .	97
6.2	Temperature dependence of magnetic anisotropy in the $a$ - $b$ plane . . . . .	99
6.3	Temperature dependence of magnetic anisotropy in the $b$ - $c$ plane . . . . .	100
6.4	Magnetic anisotropy as a function of temperature . . . . .	101
6.5	Magnetic susceptibility as a function of temperature . . . . .	102
6.6	$\hat{c}$ axis view of $\text{Li}_2\text{IrO}_3$ crystal structure . . . . .	104
6.7	Schematic of the equidistant susceptibility . . . . .	107
6.8	Ratio of the magnetic anisotropies at high temperatures . . . . .	108
6.9	Sign change of $\alpha_{bc} = \chi_b - \chi_c$ . . . . .	110
6.10	Inverse susceptibility as a function of temperature . . . . .	111
6.11	$\tau/H$ with field applied along the crystallographic $\hat{b}$ direction . . . . .	114
6.12	The magnetic structure of $\text{Li}_2\text{IrO}_3$ . . . . .	115

6.13	The angle dependence of the low field slope and $H^*$ for all components of anisotropy . . . . .	116
6.14	The Ir-O <sub>2</sub> -Ir Planes in Li <sub>2</sub> IrO <sub>3</sub> . . . . .	117
7.1	Li <sub>2</sub> IrO <sub>3</sub> crystal mounted on a fixed angle probe . . . . .	120
7.2	Temperature dependence of torque in 65 T pulsed field magnet . . . . .	121
7.3	SEM images of Li <sub>2</sub> IrO <sub>3</sub> crystal during the FIB cutting process . . . . .	123
7.4	$\tau/H$ as a function of field for the $b$ - $c$ plane of rotation . . . . .	124
7.5	Orientation of crystal for $b$ - $c$ plane of rotation, kink field and low field slope plotted as a function of angle . . . . .	125
7.6	Magnetic anisotropy in the $a$ - $c$ plane for magnetic fields up to 90 T . . . . .	130
7.7	Magnetic anisotropy in the $b$ - $c$ plane for magnetic fields up to 90 T . . . . .	131
8.1	Cu(py <sub>2</sub> z)(gly)(ClO <sub>4</sub> ) structural characteristics . . . . .	136
8.2	Energy spectrum of a weakly interacting spin dimer system . . . . .	138
8.3	Magnetic phase boundary of Cu(py <sub>2</sub> z)(gly)(ClO <sub>4</sub> ) . . . . .	140
8.4	The temperature-field phase diagram for Cu(py <sub>2</sub> z)(gly)(ClO <sub>4</sub> ) . . . . .	141
8.5	Frequency-magnetic field scaling of EPR spectra of Cu(py <sub>2</sub> z)(gly)(ClO <sub>4</sub> ) . . . . .	143
8.6	Angle-dependent EPR spectra . . . . .	144
8.7	Angle dependent $g$ -factor . . . . .	145
8.8	$g$ -factor along high symmetry directions . . . . .	146
8.9	Temperature dependence of $g$ -factor . . . . .	147
8.10	Temperature dependence of the EPR intensity . . . . .	149

## Abbreviations

<b>ARPES</b>	<b>A</b> ngle <b>R</b> esolved <b>P</b> hoto <b>E</b> mission <b>S</b> pectroscopy
<b>BCS</b>	<b>B</b> ardeen <b>C</b> ooper <b>S</b> chrieffer
<b>BEC</b>	<b>B</b> ose <b>E</b> instein <b>C</b> ondensate
<b>BEDT-TFF</b>	<b>B</b> is <b>E</b> thylene <b>D</b> i <b>T</b> hio - <b>T</b> etra <b>T</b> hia <b>F</b> ulvalene
<b>BKT</b>	<b>B</b> erezinsky <b>K</b> osterlitz <b>T</b> houless
<b>CINT</b>	<b>C</b> enter for <b>I</b> ntegrated <b>N</b> ano <b>T</b> echnologies
<b>DC</b>	<b>D</b> irect <b>C</b> urrent
<b>DFT</b>	<b>D</b> ensity <b>F</b> unctional <b>T</b> heory
<b>EPR</b>	<b>E</b> lectron <b>P</b> aramagnetic <b>R</b> esonance
<b>FIB</b>	<b>F</b> ocused <b>I</b> on <b>B</b> eam
<b>GLY</b>	<b>GLY</b> cine
<b>LANL</b>	<b>L</b> os <b>A</b> lamos <b>N</b> ational <b>L</b> aboratory
<b>MRXD</b>	<b>M</b> agnetic <b>R</b> esonant <b>X</b> -ray <b>D</b> iffraction
<b>NHMFL</b>	<b>N</b> ational <b>H</b> igh <b>M</b> agnetic <b>F</b> ield <b>L</b> aboratory
<b>NiO</b>	<b>N</b> ickel <b>O</b> xide
<b>PDO</b>	<b>P</b> roximity <b>D</b> etector <b>O</b> scillator
<b>PYZ</b>	<b>PY</b> ra <b>Z</b> ine
<b>SNL</b>	<b>S</b> andia <b>N</b> ational <b>L</b> aboratory
<b>STM</b>	<b>S</b> canning <b>T</b> unneling <b>M</b> icroscopy
<b>SQUID</b>	<b>S</b> uperconducting <b>Q</b> uantum <b>I</b> nterference <b>D</b> evice

*Abbreviations*

---

<b>SXD</b>	<b>S</b> ingle-crystal <b>X</b> -ray <b>D</b> iffraction
<b>TDO</b>	<b>T</b> unnel <b>D</b> iode <b>O</b> scillator
<b>TI</b>	<b>T</b> opological <b>I</b> nsulator

## Physical Constants

Bohr magneton	$\mu_B = 9.274 \times 10^{-24} \text{ J T}^{-1}$
Boltzmann constant	$k_B = 1.381 \times 10^{-23} \text{ J K}^{-1}$
electron charge	$e = 1.602 \times 10^{-19} \text{ C}$
electron mass	$m_e = 9.109 \times 10^{-31} \text{ kg}$
permeability of free space	$\mu_o = 4\pi \times 10^{-7} \text{ N A}^{-2}$
Planck's constant	$h = 6.626 \times 10^{-34} \text{ J s}$
reduced Planck's constant	$\hbar = 1.055 \times 10^{-34} \text{ J s}$

## Symbols

$\Psi$	atomic wavefunctions
$B_J(y)$	Brillouin function
$U$	Coulomb repulsion
$J_D$	direct exchange
$\mu_{\text{eff}}$	effective magnetic moment
$g$	electronic $g$ -factor
$E$	energy
$J$	exchange constant
$\nu$	frequency
$\mathcal{H}$	Hamiltonian
$g_J$	Landau $g$ -factor
$H$	magnetic field
$m$	magnetic moment
$\chi$	magnetic susceptibility
$M$	magnetization
$L$	orbital angular momentum
$S$	overlap intergral
$Z$	partition function
$R$	resistance
$M_S$	saturation magnetization

## *Symbols*

---

$S$	spin angular momentum
$\lambda$	spin orbit coupling
$T$	temperature
T	Tesla
$\tau$	torque
$J$	total angular momentum
$t$	transfer integral
$V$	voltage

## Introduction

A central concept in condensed matter research is strongly correlated electron physics. Materials with strong correlations exhibit unusual electronic and magnetic properties which cannot accurately be described by the single-particle behavior of electrons. Electronic correlations are at the heart of a plethora of phenomena, including local Mott-Hubbard moment formation and magnetism, non Fermi-liquid behavior in correlated metallic states, quantum criticality, and superconductivity [1]. The road towards understanding the extraordinary properties arising from correlations in these materials has been paved by over 90 years of theoretical and experimental advancements, which started with the discovery and formalization of quantum mechanics in the mid-1920's. In this introduction, I will outline a brief history of condensed matter research that leads us into the active areas of material interests today.  $\text{Li}_2\text{IrO}_3$ , the main focus of this thesis, is then presented as a strongly spin-orbit coupled and magnetically frustrated Mott insulator, which is the foundation for its curious magnetic behavior.

## 1.1 Progression of Quantum Materials Research

The concepts of quantum mechanics were applied as the band theory of solids to successfully explain the metallic, semiconducting, and insulating behavior observed in many materials. Band theory relies on the periodic nature of a solid to construct smoothly evolving bands (or levels) of energy states that are occupied by the electrons. The physical properties of the system are then determined by those states with energy near the chemical potential, which can be visualized as a surface of constant energy in momentum space known as the Fermi surface. Importantly, band theory provided a verifiable test for the quantum mechanical considerations upon which it was founded, and stimulated an advance in experimental techniques widely used today to map out the Fermi surface of metals by directly observing, for example, the de Haas-van Alphen and Shubnikov-de Haas effects [2]. As time unfolded, this single-particle treatment of electrons in a static potential, without considering interactions with other electrons, phonons, photons, etc., became a major limitation for band theory applied to more complex systems.

The breakdown of band theory was evident by the late 1930's when insulating behavior was discovered in many of the transition-metal oxides which were expected to be metals by conventional band theory. An explanation given by Nevil Mott in 1949 used repulsive electron-electron interactions to capture the insulating behavior in the expected metal NiO [3, 4]. The underlying mechanism can be understood as a competition between a strong on-site Coulomb repulsion  $U$ , which prevents electrons from occupying the same orbitals, and the kinetic energy described by the transfer integral  $t$  of electrons hopping between neighboring atoms. The diverse properties arising from these 'Mott insulators' started an investigation into what have become known as strongly correlated materials, where a physical picture that includes electronic interactions is invoked to describe the

material properties. The most notable example is the attractive electron-pairing driven by phonons in the 1957 BCS theory of superconductivity [5]. Other significant examples of strongly correlated systems include the manganites and the nickelates, which exhibit remarkable properties of microscopic origins that are still under debate today. One key observation, which was initially missed, was that almost all of these materials have local magnetic moments that order antiferromagnetically at low enough temperatures. This includes the high-temperature superconducting cuprates in their undoped state, which debuted in 1987. Despite large computational advances in the 70's and 80's, band structure calculations mistakingly found the ground state of most of these materials to be ferromagnetic metals, stimulating a push for a theoretical framework that could elucidate the physics of correlated materials. Perhaps as profound as the discovery of high temperature superconductivity, the drive to understand such emergent phenomena hugely advanced experimental techniques that are used today in condensed matter physics, including STM (scanning tunneling microscopy), ARPES (angle resolved photoemission spectroscopy), and neutron and x-ray diffraction.

A new chapter in materials research started with the discovery of the quantum Hall effect, bringing topological ground states into focus. In the fractional quantum Hall effect, the Hall conductance of a two-dimensional electron gas at very low temperatures and in extreme magnetic fields becomes quantized into fractional values of the fundamental conductance quantum  $2e^2/h$ . The theory behind this many-body problem produces quantitatively accurate and experimentally confirmed results [6–8]. Details aside, symmetry alone does not characterize the different fractional states. This means that the longstanding Landau symmetry breaking theory is insufficient to describe the fractional states, implying the presence of a new kind of order – topological order [9].

The existence of topological order has defined a new and ongoing direction in

condensed matter physics, which blossomed with the prediction of symmetry protected topological insulators (TI) – bulk insulators with conducting surface states. Symmetry-protected surface states were first observed in quantum wells of mercury telluride in 2007 [10]. This was quickly followed by the first realization of a bulk topological insulator in bismuth antimonide in 2008 after it was suggested that large spin-orbit interactions  $\lambda$  could naturally support these topological states [11]. Up to this point, most of these topological states require only a single-particle picture, analogous to the band theory of solids. The spin-orbit coupled and topological era of materials has been greatly enriched by the emergence of many-body systems, such as topological Mott and Kondo insulators [12, 13]. Even more non-trivial states of matter, such as the quantum spin liquid, are expected to emerge by introducing strongly correlated electrons into the mix. Importantly, the mesoscopic studies of such materials is bridging the gap between fundamental research and application and is contributing to major advancements in device fabrication and epitaxial growth.

### 1.2 Strongly Spin-Orbit Coupled Mott Insulators

In recent years, an increasing number of experimental systems displaying a wide variety of complex phenomena are appearing in the strongly correlated and strongly spin-orbit coupled region of the materials phase diagram (Figure 1.1). This includes the Ruddlesdon-Popper series of pseudo-cubic and planar perovskites  $\text{Sr}_{n+1}\text{Ir}_n\text{O}_{3n+1}$  (where  $n=1,2, \infty$ ) and a large family of pyrochlores  $\text{R}_2\text{Ir}_2\text{O}_7$  ( $\text{R}$  = rare-earth), as well as many (Os, Rh, Ru)-based oxides that are exploited due to their similarly large spin-orbit coupling. The focus of this thesis remains on the hexagonal iridium-based insulators with the chemical formula  $(\text{Li, Na})_2\text{IrO}_3$ , often referred to as ‘the honeycomb iridates’.

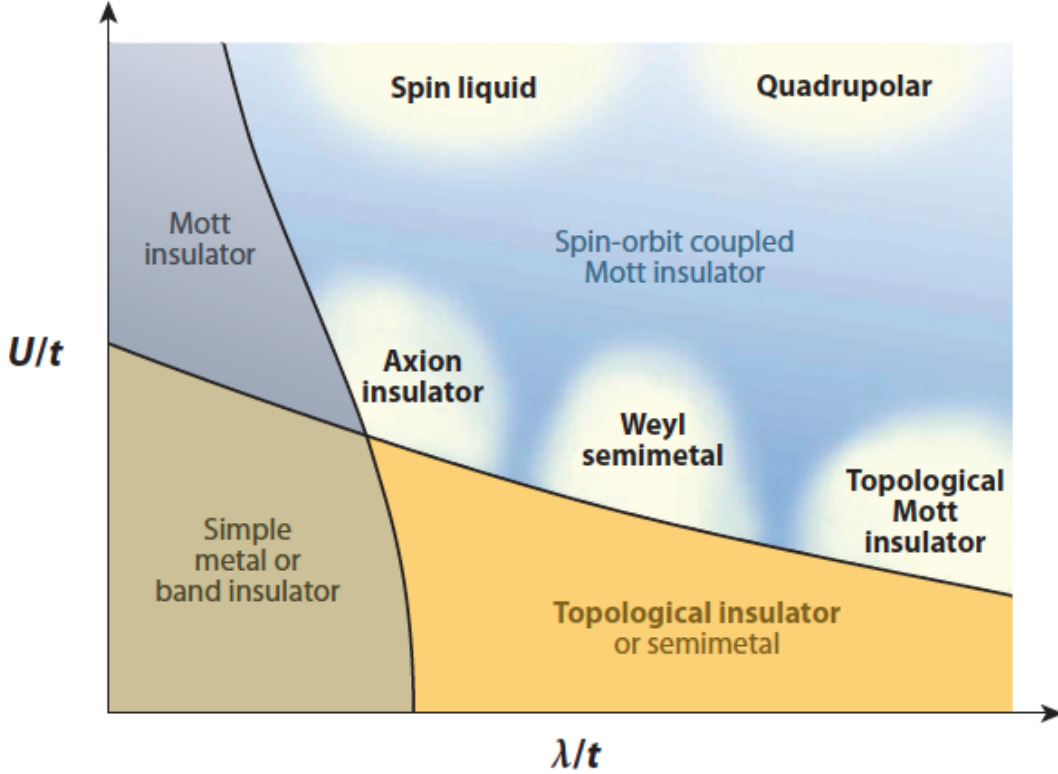


FIGURE 1.1: Sketch of a phase diagram for electronic materials in terms of the interaction strength  $U/t$  and spin-orbit coupling  $\lambda/t$ . Figure and caption reproduced from [1].

The story of  $\text{Li}_2\text{IrO}_3$  – a strongly spin-orbit coupled Mott insulator – picks up where the brief history of condensed matter research concludes. The combined influence of strongly correlated electrons and strong spin-orbit coupling on its honeycomb lattice make it an ideal candidate to search for frustrated magnetism and a spin liquid ground state. Despite the fact that  $\text{Li}_2\text{IrO}_3$  and its closely related analogue  $\text{Na}_2\text{IrO}_3$  order magnetically at low temperatures, the honeycomb iridates are continuing to attract considerable attention, both theoretically and experimentally [14–21], as an insightful path towards engineering and understanding exotic magnetism. More recently, they have sparked a resurgence of interest in

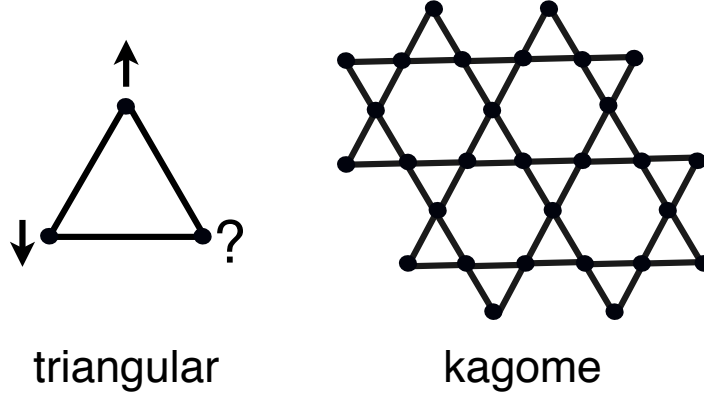
the structurally similar  $\text{RuCl}_3$  [22–25], as well as an investigation into the newly-synthesized honeycomb ruthenates  $(\text{Li}, \text{Na})_2\text{RuO}_3$  [26]. This intense interest is mostly due to an intriguingly complex magnetic order observed in the honeycomb iridates that supports a connection to the Kitaev model – an exactly solvable model on a honeycomb lattice, where only orthogonal components of spin couple on the three nearest neighbors bonds [27–34]. Such extreme anisotropy in the exchange interactions on a honeycomb lattice that depends upon the spatial direction of each bond has a ground state solution that is a highly-degenerate spin liquid [27]. This observation prompted the exploration to implement Kitaev’s model in strongly spin-orbit coupled Mott insulators, such as  $\text{Li}_2\text{IrO}_3$ , where a superexchange mechanism expected to enhance the anisotropy in the spin-exchange is dependent upon an edge-shared octahedral environment [28].

In this thesis, the magnetic properties of  $\text{Li}_2\text{IrO}_3$  are studied using a cantilever torque magnetometry technique in DC and pulsed magnetic fields up to 100 Tesla. Analysis of these high-precision measurements reveal details about the magnetic anisotropy which would otherwise be unobtainable with conventional magnetometry methods. The results presented herein provided the first experimental evidence for highly anisotropic exchange interactions – a compelling manifestation of Kitaev’s model – to exist in  $\text{Li}_2\text{IrO}_3$  [35], placing theoretical predictions on firm experimental ground. The connection between the honeycomb iridates and the Kitaev model has since been further substantiated by evidence for dominant bond-directional exchange interactions in  $\text{Na}_2\text{IrO}_3$  [36] and  $\beta\text{-Li}_2\text{IrO}_3$  (the hyper-honeycomb structure) [37].

One of the key players in producing anisotropy in exchange interactions is the spin-orbit coupling, whereby the electron spin interacts with the magnetic field produced by its orbital motion. This effect becomes increasingly important upon descending the periodic table and certainly for the extended  $5d$  orbitals of iridium,

it cannot be ignored. Extended orbitals increase the separation between electrons, which decreases the Coulomb repulsion  $U$  and typically reduces correlations between the electrons. At least this is the case for the heavier  $s$ - and  $p$ - electron elements, where the intensified role of spin-orbit coupling is accompanied by a somewhat weakened correlation effect, leading to the possibility of topologically insulating materials (Figure 1.1). However, in some systems, particularly those with high symmetry, spin-orbit coupling and the Coulomb interaction can cooperate to enhance electronic correlations. The octahedral environment of the heavier transition metal oxides are a common place to look for this unique influence: strong correlations result from orbital degeneracies, which the spin-orbit coupling splits into multiple narrow bands. The narrow bands are more susceptible to Mott localization and a reduction in kinetic energy that offsets the decrease in Coulomb repulsion due to the extended orbitals [1].

Exotic ground states, such as the spin liquid, are expected to arise when there is a conflict – or frustration – between the magnetic interactions in the lattice as a result of the underlying crystal geometry. The simplest way to think about magnetic frustration is by considering three antiferromagnetically coupled spins on a triangular arrangement (Figure 1.2). To minimize the energy of this system, each of the spins wants to be antialigned with its nearest neighbors. This condition, which cannot be simultaneously satisfied by all three nearest neighbors, leads to a degeneracy of ground state spin configurations and the magnetic analogue of a liquid in an extended state. The kagome lattice is another example of a lattice geometry which inhibits the simultaneous energy minimization of all antiferromagnetic interactions (Figure 1.2). By considering a spin on each of the lattice points of this structure, it is easy to see why it naturally leads to frustration; the antiferromagnetic interaction between neighboring spins cannot be simultaneously satisfied because a third spin cannot point in a direction opposite to two others if



---

FIGURE 1.2: (Left) The triangular arrangement of spins with antiferromagnetic interactions that cannot be simultaneously satisfied by all nearest neighbors. (Right) The kagome lattice made up of vertex-sharing triangles.

they have already aligned antiferromagnetically.

In the honeycomb iridates, the observed insulating behavior is due to an energy gap created by a large  $U$ . Thus, it is sufficient to regard the electrons as localized so they can be ascribed to local spin and orbital degrees of freedom at each iridium site of the honeycomb lattice (Chapter 3). The localized treatment of the spins make the geometric arrangement of the iridium very important. The iridium in  $\text{Li}_2\text{IrO}_3$  form a three-dimensional honeycomb structure, where each iridium has the same local environment as in the layered honeycomb structure (Chapter 3). The magnetic frustration in the honeycomb lattice is not a direct result of the lattice geometry alone, but rather arises from orbital and spin frustrations that are introduced by the spin-orbit interaction. In the strong Mott limit, the strength of this interaction should be compared with the exchange interaction  $J$ , which is proportional to  $t^2/U$  (Chapter 2). When the spin-orbit coupling is large, the local moments acquire a large orbital component and the presence of several equivalent

bond directions in the highly symmetric octahedral environment of each iridium gives rise to strongly frustrated magnetism.

This thesis includes a short review of magnetism in the next chapter, emphasizing the physics relevant to  $\text{Li}_2\text{IrO}_3$ . In Chapter 3, I will discuss the current progress in this field of research; briefly reviewing previous work on similar compounds before transitioning to  $\text{Li}_2\text{IrO}_3$  specifically. The experimental techniques used to study both  $\text{Li}_2\text{IrO}_3$  and  $[\text{Cu}(\text{pyz})(\text{gly})](\text{ClO}_4)$  (a molecular magnet considered in Chapter 8) is presented in Chapter 4. The techniques include torque magnetometry and magnetic susceptibility measurements using a PDO (proximity detector oscillator) circuit in pulsed magnetic fields, as well as EPR (electron paramagnetic resonance) measurements using a cavity perturbation method in a superconducting magnet. Chapter 5 presents the magnetic torque of  $\text{Li}_2\text{IrO}_3$ , as well as a detailed analysis of the measurements. The significance of the results, in regards to understanding the magnetic anisotropy from the low field response, will be considered in Chapter 6. In Chapter 7, more recent high field data is shown and the results are discussed in the context of open questions and future work. Chapter 8 explores the temperature-magnetic field phase diagram of an organic magnet comprised of weakly coupled Cu dimer units. All of the data contained within was taken at the Pulsed Field Facility (PFF) of the National High Magnetic Field Laboratory (NHMFL) in Los Alamos, New Mexico. Here, the typical “workhorse” magnet creates a 65 Tesla (T) magnetic field that lasts for less than a tenth of a second and requires 300 megawatts of power, posing a unique challenge for sensitive measurements. Appropriately, a large portion of this thesis is devoted to the experimental details of the torque magnetometry technique performed in this challenging environment.

## 2

### Review of Magnetism

#### 2.1 Paramagnetism

One of the simplest ways to introduce magnetism in solids is through consideration of a paramagnetic gas of noninteracting electrons. This describes a collection of independent magnetic moments which, in the absence of a magnetic field, orient themselves in random directions [38]. The application of a magnetic field tilts the moments along the field direction and the degree to which they align – the induced magnetization – depends upon the strength of the applied field. The source of the magnetism for each magnetic moment  $m = \mu_B S$  is the intrinsic spin  $S$  of each electron and is typically represented in units of the Bohr magneton  $\mu_B = \frac{e\hbar}{2m_e}$ . Here,  $e$  is the charge of the electron,  $m_e$  is the electron mass, and  $\hbar$  is the reduced Planck constant. In an applied magnetic field  $H$ , the energy associated with a magnetic moment is  $E = -g\mu_o\vec{m} \cdot \vec{H}$ , where  $\mu_o = 4\pi \times 10^{-7}$  N/A<sup>2</sup> represents the permeability of free space and  $g$  is the g-factor – a quantum mechanical correction to a magnetic moment in a solid due to relative contributions of spin and orbital angular momentum. First, consider each spin to be in one of its two eigenstates in an external field  $S = \pm\frac{1}{2}$ , which correspond to alignment with the applied field ( $+\frac{1}{2}$  = spin up) or anti-alignment ( $-\frac{1}{2}$  = spin down). As a function of the strength

of the applied field, the energy of one spin state will increase linearly while the energy of the other will decrease, known as Zeeman splitting. The Hamiltonian  $\mathcal{H}$  describing the effect of an applied magnetic field on each spin is therefore

$$\mathcal{H}_Z = -g\mu_o\mu_B\mathbf{H} \cdot \mathbf{S}, \quad (2.1)$$

which suggests that the energy of the system will be minimized when the spins align with the external field.

For such a gas, Maxwell-Boltzmann statistics can be used to find the probability of each spin configuration in thermal equilibrium

$$p_{\pm} = \frac{1}{Z} \exp\left(\frac{-E_{\pm}}{k_B T}\right), \quad (2.2)$$

where  $T$  is the temperature and  $k_B$  is the Boltzmann constant. The partition function is  $Z = \exp\left(\frac{E_-}{k_B T}\right) + \exp\left(\frac{E_+}{k_B T}\right)$ . For a spin  $\frac{1}{2}$  system with  $g \approx 2$ , the energy of each spin configuration is approximately  $E_{\pm} = \mp\mu_o\mu_B H$  and the average or net moment  $\langle m \rangle$  can be found from the expectation value (difference in the two probabilities for spin  $\frac{1}{2}$  case)

$$\langle m \rangle = \mu_B \tanh\left(\frac{\mu_o\mu_B H}{k_B T}\right). \quad (2.3)$$

This equation describes full spin polarization in an external magnetic field at low temperatures, where  $\tanh(x) \rightarrow \pm 1$  depending on the orientation of the magnetic field. It also captures a decrease in the average moment with increasing temperature. At thermal energies large compared to the energy scale of the applied magnetic field, the argument is small and can be approximated as  $\tanh(x) \approx x$  and the Curie susceptibility  $\chi = M/H = n\langle m \rangle/H$  of a noninteracting system with

two possible spin states is found

$$\chi = \frac{n\mu_o\mu_B^2}{k_B T}. \quad (2.4)$$

The letter  $n$  is used to denote the number of magnetic moments per unit volume [39].

The more general form of the Curie law, where the total angular momentum  $J$  can take any integer or half integer value, can be found from a description of the magnetization which involves the Brillouin function  $B_J(y)$

$$M = M_S B_J(y), \quad (2.5)$$

where the saturation magnetization  $M_S = ng_J\mu_B J$  [39]. The Brillouin function, which results from a geometric progression of the partition function for all  $M = 2J + 1$  states, is given below without the full derivation

$$B_J(y) = \frac{2J+1}{2J} \coth\left(\frac{2J+1}{2J}y\right) - \frac{1}{2J} \coth\frac{y}{2J}, \quad (2.6)$$

where  $y = g_J\mu_B\mu_o H J/k_B T$  [39]. At small applied magnetic fields or high temperatures, the general features of the susceptibility remain the same as found for the spin 1/2 case, but the Maclaurin expansion of the small coth arguments result in a factor of 3 in the denominator in the Brillouin function

$$B_J(y) = \frac{(J+1)y}{3J} + O(y^3), \quad (2.7)$$

where  $O$  represents higher order terms. By extension, the 1/3 factor also appears in the Curie law [39]. In the limit of small  $y$ , the susceptibility  $\chi = M/H =$

$ng_J\mu_B JB_J(y)/H$  is written as

$$\chi = \frac{n\mu_o\mu_{\text{eff}}^2}{3k_B T}, \quad (2.8)$$

where  $\mu_{\text{eff}} = g_J\mu_B\sqrt{J(J+1)}$ , the Lande g-value  $g_J = \frac{3}{2} + \frac{S(S+1)-L(L+1)}{2J(J+1)}$ , and  $L$  is the total orbital angular momentum [39]. At thermal energies large compared to the energy of the applied magnetic field, Equation 2.8 suggests that a measurement of the susceptibility can be used to find the effective magnetic moment (Chapter 6).

## 2.2 Exchange Interactions

In some materials, such as iron, a net magnetization can occur in the absence of an applied magnetic field. This spontaneous ‘ferromagnetism’, among many other types of long range magnetic order, is created and stabilized by the exchange interactions between the magnetic moments [38]. The fate of the magnetic order is determined by the competition between the Coulomb interactions, an electrostatic force that is inversely proportional to the distance  $r$  squared between two charged particles, and their kinetic energies. The exchange interaction is then a many electron effect which is dependent upon the density of electrons [38]. Quantum mechanically, the exchange interaction occurs between identical particles whose wavefunctions are subject to overlap. The Pauli exclusion principle, which forbids two electrons from occupying the same state, is the necessary starting point [38]. Simply put, it says that two electrons can occupy the same orbital wavefunction, but only if they have opposite spin or anti-align. More rigorously, it requires that the overall wavefunction must be antisymmetric – or change sign – when two electrons are interchanged with respect to both spatial and spin coordinates. To

satisfy this condition, the symmetry of the spatial wavefunction must be opposite the symmetry of the spin wavefunction [38].

Before blindly calculating the exchange interaction, it is helpful to have some intuition of how the separation between electrons affects the exchange. Because of the Pauli principle, electrons which have the same spin cannot be at the same position, and thus they tend to avoid each other. The probability of finding like spins close to each other is lower than that for opposite spins. By this argument, the Coulomb interaction will usually be larger for opposite spins making it more energetically favorable for the spins to align parallel to one another. Thus, it is generally true that two electrons residing on the same orbital will try to minimize their Coulomb interaction by increasing separation between them and aligning parallel to one another [38]. When neighboring atoms (inter-atomic) are involved, the separation between the electrons can be further increased by allowing electrons to hop to neighboring atoms [38]. The kinetic energy can be minimized by forming bands – states that are a superposition of the states centered at each atom. As the hopping is increased, the lowest energy state will be a spatially symmetric (bonding) state on which two spins will align opposite to one another – antiferromagnetically [38]. For a parallel spin alignment to occur in this case, one of the electrons must acquire energy via the Coulomb interaction to move to the excited antibonding state [38]. The exchange interaction

$$J = \frac{E_{AFM} - E_{FM}}{2} \quad (2.9)$$

is directly related to the difference between the energy of the lowest lying antiferromagnetic and ferromagnetic states [38]. The desire for the system to minimize its energy tells us that the ferromagnetic state has lower energy for the case of intra-atomic exchange and therefore, the exchange interaction  $J$  (Equation 2.9) must be positive [38]. By a similar argument, it is common for inter-atomic exchange to

result in a negative exchange integral and antiferromagnetic ordering. Thus, the Pauli principle implies that spatially symmetric and antisymmetric wavefunctions describe antiferromagnetic and ferromagnetic spin configurations, respectively [38]. In this section, the effective coupling between the magnetic moments in a solid are understood by considering the Pauli exclusion principle in combination with the Coulomb repulsion and the hopping of electrons.

### 2.2.1 One electron in a solid

Before understanding the exchange interaction between two electrons, it is instructive to start by considering just one electron in a solid containing only two atoms [38]. If the atoms are well separated, the electron on one of the atoms can be described by the atomic wavefunctions  $\Psi$  given by the Schrödinger equation

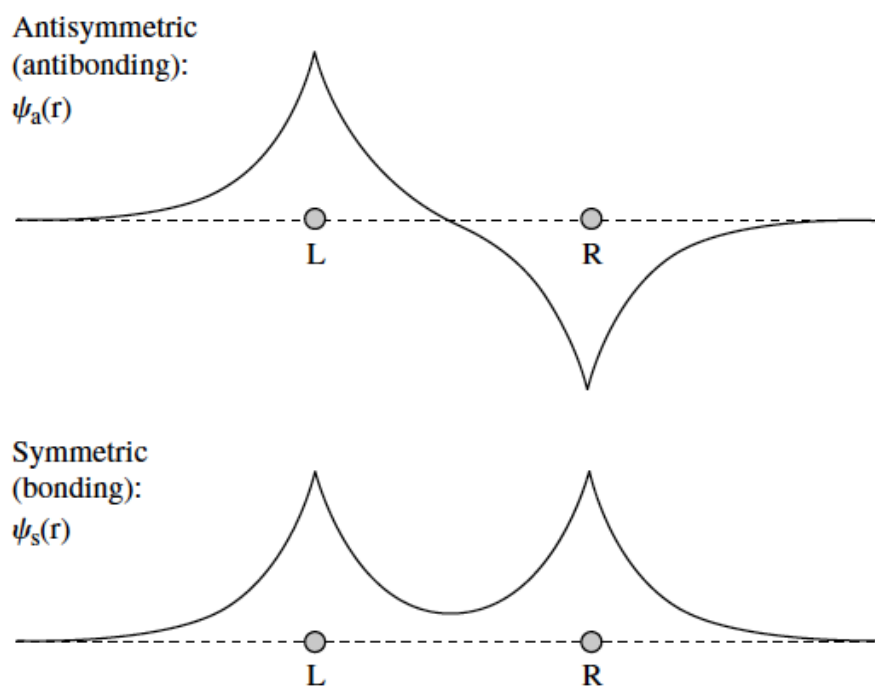
$$E\Psi = -\frac{\hbar^2}{2m} \nabla^2 \Psi + V_o(r)\Psi, \quad (2.10)$$

where  $V_o(r)$  describes the attractive potential from the nucleus [38]. However, in a solid where two atoms are separated by a distance  $R$ , it is more realistic that the wavefunctions will overlap rendering the atomic wavefunctions no longer representative of the system [38]. In this case, the electron feels a potential from both atoms and can be described by

$$E\Psi = -\frac{\hbar^2}{2m} \nabla^2 \Psi + V_o(r)\Psi + V_o(|r - R|)\Psi, \quad (2.11)$$

where the solutions to this equation are perturbed wavefunctions that can be approximated as linear combinations of the atomic wavefunctions  $\phi_1(r), \phi_2(r)$  [38]. The two nearby atoms are denoted as 1 and 2. The hybridized wavefunctions are the spatially symmetric state  $\psi_s(r) \sim \phi_1(r) + \phi_2(r)$  and the spatially antisymmetric

state  $\psi_a(r) \sim \phi_1(r) - \phi_2(r)$  (Figure 2.1), the latter of which is higher in energy [38].




---

FIGURE 2.1: The hybridized wavefunctions that are formed from linear combinations of the atomic wavefunctions. Figure reproduced from [38].

The mixing or hybridization of the atomic orbitals allows the electron to hop to nearby atoms and this plays an important role in determining the exchange interaction. The kinetic-energy operator  $T = -\frac{\hbar^2 \nabla^2}{2m}$  [38] can be used to define a hopping integral

$$t = - \int \phi_1^*(r) T \phi_2(r) dV. \quad (2.12)$$

This describes the hopping of the electron initially centered at atom 2 to the position centered at atom 1 by the operator  $T$ . Technically, the non-orthogonality of the atomic wavefunctions requires the involvement of an overlap integral

$$S = \int \phi_1^*(\mathbf{r})\phi_2(\mathbf{r})d\mathbf{r} \quad (2.13)$$

for proper normalization of the hybridized wavefunctions [38]. Wannier functions are a convenient alternative basis because they are orthogonal and so there is no overlap, unlike the atomic wavefunctions [38]. Because the basis set of wavefunctions is arbitrary, they will be chosen such that in the discussion of exchange to follow, only the hopping integral comes into play.

Hybridization of the wavefunctions is responsible for the energy difference between the bonding and antibonding states. Since the hybridization, which is proportional to the hopping, decreases with increasing interatomic distance, the level splitting is smallest for well-separated atoms [38]. Increased hopping causes a larger level splitting making it more favorable for two electrons to occupy the bonding state with an antiparallel spin configuration. A real solid will contain more than two atoms, but the basic construction remains the same. In the discussion to follow, the interaction between two electrons will be considered for a parallel spin configuration to occur.

### 2.2.2 The two electron problem

To explain exchange, another electron must be introduced into the problem. The two-electron wavefunction can be expanded into products of orthogonal one-electron states resulting in four wavefunctions: one where both electrons occupy the bonding orbital, one where both electrons occupy the anti-bonding orbital, and the two possibilities where one electron occupies each orbital. The Hamiltonian will be a

$4 \times 4$  matrix where the inclusion of the second electron leads to the observation of two new integrals; the direct exchange

$$J_D = \int \int \phi_1^*(\mathbf{r})\phi_2^*(\mathbf{r}')V_C(\mathbf{r}, \mathbf{r}')\phi_2(\mathbf{r})\phi_1(\mathbf{r}')dVdV' \quad (2.14)$$

between electrons on neighboring atoms and the Coulomb integral

$$U = \int \int \phi_1^*(\mathbf{r})\phi_1^*(\mathbf{r}')V_C(\mathbf{r}, \mathbf{r}')\phi_1(\mathbf{r})\phi_1(\mathbf{r}')dVdV', \quad (2.15)$$

describing an interaction between electrons occupying the same site [38]. Here,  $\mathbf{r}$  and  $\mathbf{r}'$  represent the positions of the two electrons and the subscripts 1 and 2 are used to differentiate between any two orthogonal one-electron wavefunctions. These can be the Wannier functions discussed previously or the superposition of these functions to yield the bonding and anti-bonding states. Diagonalization of the two-electron energy matrix gives four eigenfunctions, only the first of which is antisymmetric in space (symmetric in spin – ferromagnetic) [38]

$$\begin{aligned} |\psi_1\rangle &= \frac{1}{\sqrt{2}}|12\rangle - \frac{1}{\sqrt{2}}|21\rangle \\ |\psi_2\rangle &= \frac{1}{\sqrt{2}}|11\rangle - \frac{1}{\sqrt{2}}|22\rangle \\ |\psi_3\rangle &= \frac{\sin\chi}{\sqrt{2}}(|11\rangle + |22\rangle) + \frac{\cos\chi}{\sqrt{2}}(|12\rangle + |21\rangle) \\ |\psi_4\rangle &= \frac{\cos\chi}{\sqrt{2}}(|11\rangle + |22\rangle) - \frac{\sin\chi}{\sqrt{2}}(|12\rangle + |21\rangle), \end{aligned} \quad (2.16)$$

where  $\tan(2\chi) = -4t/U$  and the respective energies as a function of  $U$ ,  $J_D$ , and  $t$  are [38]

$$\begin{aligned}
 E_1 &= 2E_o - J_D \\
 E_2 &= 2E_o + U - J_D \\
 E_3 &= 2E_o + \frac{U}{2} + J_D - \sqrt{4t^2 + \frac{U^2}{4}} \\
 E_4 &= 2E_o + \frac{U}{2} + J_D + \sqrt{4t^2 + \frac{U^2}{4}}.
 \end{aligned} \tag{2.17}$$

The direct exchange – similar to an on-site Coulomb interaction, but between electrons centered at different atoms – is typically two orders of magnitude less than the on-site repulsive energy. The hopping integral – stemming from wavefunction overlap – competes with the Coulomb energy so that the lowest lying ferromagnetic (spatially antisymmetric) and antiferromagnetic (spatially symmetric) states are  $E_1$  and  $E_3$  respectively (Figure 2.2) [38].

The exchange interaction  $J$  is determined by a direct comparison of these states

$$J = \frac{E_1 - E_3}{2}. \tag{2.18}$$

The consideration of a solid with two nearby atoms where one electron resides on each atom results in the exchange constant [38]

$$J = J_D + \frac{U}{4} - \sqrt{t^2 + \frac{U^2}{16}}. \tag{2.19}$$

It is convenient to consider the exchange as a function of the hopping integral, which is dependent upon the radius of the orbital and the interatomic distance [38]. As previously discussed, a small value for the hopping integral can be associated with well localized orbitals whereas large hopping requires electrons to lie

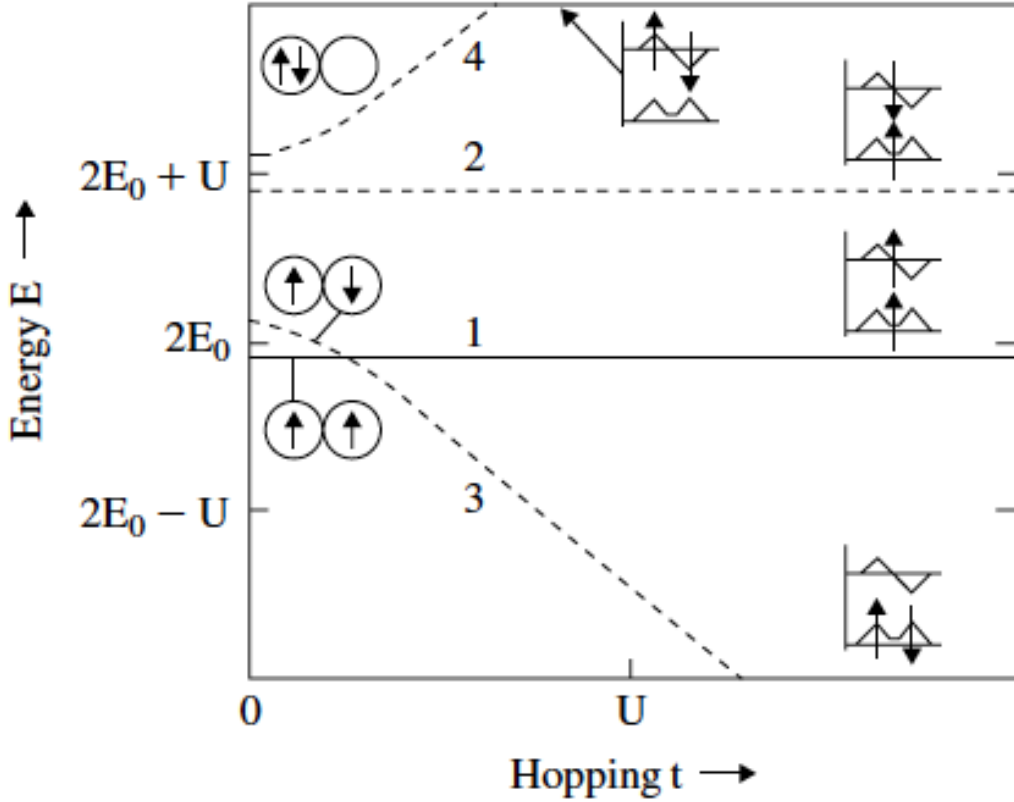


FIGURE 2.2: The two-electron energy spectrum for a diatomic pair as a function of hopping. The two-electron wavefunctions are symmetric with respect to interchanging left and right atoms, but for clarity, only some of the configurations are shown. Figure reproduced from [38].

in the bonding or antibonding states. Also, a positive value for  $J$  indicates ferromagnetism, whereas a negative number implies antiferromagnetism. Increased hopping has the tendency to alter the system from a ferromagnetic to an antiferromagnetic state and the exchange interaction  $J$  reflects the relative strength of the Coulomb integral to the hopping integral. Therefore, it is the competition between the kinetic energy (favoring inter-site anti-parallel alignment of the spins) and the Coulomb energy (favoring on-site parallel alignment) that determines the

ground state of the system. The exchange interaction is the key ingredient in modeling the behavior of magnetic materials. However, modeling the behavior of three-dimensional spins in a three-dimensional space is a difficult problem to solve. Some models which simplify this problem are presented in the following sections.

### 2.3 The Ising Model

In the Ising model, only one component of spin is considered, which for example may be labeled as  $s_z$  to denote the  $z$  component of coupling between each spin at each lattice site. It then represents an extreme case of spin anisotropy in which the spins can only point along or against one direction. The Hamiltonian can be written as

$$\mathcal{H}_I = - \sum_{i,j} J_{i,j} S_i S_j - g\mu_o\mu_B \sum_i H_i S_i, \quad (2.20)$$

which includes the exchange interaction  $J_{ij}$  between two nearest neighbor spins labelled  $i$  and  $j$  and in the case of an external field, a term representing the effect of the local magnetic field  $H_i$  acting on the  $i$ th spin [38]. The Ising model is the simplest model that can describe a finite-temperature magnetic transition occurring in the absence of an applied magnetic field.

Extensions of the Ising model include the classical XY model, where each spin is treated as a two-dimensional vector and the coupling between spins is denoted with  $x$  and  $y$  components. Physically though, a spin will precess about a field applied along the  $z$  direction, requiring a three component spin operator with  $2S + 1$  discrete orientations. The Heisenberg model, which describes three-dimensional spins, is discussed next.

## 2.4 The Heisenberg Model

The Heisenberg model is the isotropic equivalent of the Ising model with a Hamiltonian that includes an interaction term for each of its three components of spin. The general form of the Heisenberg Hamiltonian is

$$\mathcal{H}_H = - \sum_{i,j} J_{i,j} \mathbf{S}_i \cdot \mathbf{S}_j - g\mu_o\mu_B \sum_i \mathbf{H}_i \cdot \mathbf{S}_i \quad (2.21)$$

and the motivation for the spin form of the Ising and Heisenberg Hamiltonians is discussed below.

The Heisenberg model can be used to describe systems with a fixed number of well-localized electrons per atom, which arises from a large Coulomb repulsion that prevents double occupancy of electrons. The basic idea is to consider the interactions between electrons, but ignore the temporary ionic states resulting from inter-atomic hopping [38]. In reference to the two electron problem discussed above, the ionic configurations  $|11\rangle$  and  $|22\rangle$  are ignored by assuming a large Coulomb repulsion ( $U \rightarrow \infty$ ). Thus, only the  $|12\rangle$  and  $|21\rangle$  states remain. Diagonalization of the energy matrix yields the antisymmetric state  $|12\rangle - |21\rangle$  and the symmetric state  $|12\rangle + |21\rangle$  resulting in an exchange interaction  $J = J_D$ .

The large Coulomb interaction localizing the electrons allows us to describe the system using only spin degrees of freedom. The individual electrons can be treated as spins with the spin part of the wavefunction introduced in a way to preserve the overall asymmetry of the wavefunction. Therefore, an antisymmetric singlet state  $\chi_S$  ( $S=0$ ) is required for the spatially symmetric state and a symmetric triplet state  $\chi_T$  ( $S=1$ ) is necessary for the spatially antisymmetric state. The wavefunctions

are then

$$\begin{aligned}\Psi_S &= \frac{1}{\sqrt{2}}[\psi_1(\mathbf{r})\psi_2(\mathbf{r}') + \psi_1(\mathbf{r}')\psi_2(\mathbf{r})]\chi_S \\ \Psi_T &= \frac{1}{\sqrt{2}}[\psi_1(\mathbf{r})\psi_2(\mathbf{r}') - \psi_1(\mathbf{r}')\psi_2(\mathbf{r})]\chi_T,\end{aligned}\quad (2.22)$$

where  $\mathbf{r}$  and  $\mathbf{r}'$  represent the spatial coordinates of the two electrons [39]. The energy for each state is

$$\begin{aligned}E_S &= \int \Psi_S^* \mathcal{H} \Psi_S \, d\mathbf{r} \, d\mathbf{r}' \\ E_T &= \int \Psi_T^* \mathcal{H} \Psi_T \, d\mathbf{r} \, d\mathbf{r}'\end{aligned}\quad (2.23)$$

with the assumption that the spin parts of the wavefunction  $\chi_S$  and  $\chi_T$  are normalized [39]. The difference between the two energies is

$$E_S - E_T = 2 \int \psi_1^*(\mathbf{r})\psi_2^*(\mathbf{r}')\mathcal{H}\psi_1(\mathbf{r}')\psi_2(\mathbf{r}) \, d\mathbf{r} \, d\mathbf{r}',\quad (2.24)$$

where the right hand side without the prefactor 2 is the exact form of the direct exchange  $J_D$  (Equation 2.14), suggesting that  $J = J_D$  [39].

To parameterize in terms of two spin  $\frac{1}{2}$  particles where the total spin is represented by the operator  $\hat{\mathbf{S}}_{tot} = \hat{\mathbf{S}}_1 + \hat{\mathbf{S}}_2$  [39], the square of this operator is needed

$$(\hat{\mathbf{S}}_{tot})^2 = (\hat{\mathbf{S}}_1)^2 + (\hat{\mathbf{S}}_2)^2 + 2\hat{\mathbf{S}}_1 \cdot \hat{\mathbf{S}}_2.\quad (2.25)$$

The eigenvalue of  $(\hat{\mathbf{S}}_{tot})^2$  is  $s(s+1)$ , where  $s$  represents the spin quantum number resulting from the possible combinations of two spin  $\frac{1}{2}$  particles. With  $s = 0$  or  $1$ , the eigenvalues are  $0$  or  $2$ , respectively. For each spin, the operator  $\hat{\mathbf{S}}^2 = \hat{\mathbf{S}}_x^2 + \hat{\mathbf{S}}_y^2 + \hat{\mathbf{S}}_z^2$  acting on any spin state gives the eigenvalue  $(\pm\frac{1}{2})^2 + (\pm\frac{1}{2})^2 + (\pm\frac{1}{2})^2 = \frac{3}{4}$ . Now, the eigenvalue for the operator  $\hat{\mathbf{S}}_1 \cdot \hat{\mathbf{S}}_2$  can be calculated for each state  $s =$

0, 1. An effective Hamiltonian can be written in terms of  $\hat{\mathbf{S}}_1 \cdot \hat{\mathbf{S}}_2$

$$\mathcal{H} = \frac{1}{4}(E_S + 3E_T) - (E_S - E_T)\hat{\mathbf{S}}_1 \cdot \hat{\mathbf{S}}_2, \quad (2.26)$$

such that the energy of the spin triplet state is found when  $\hat{\mathbf{S}}_1 \cdot \hat{\mathbf{S}}_2 = \frac{1}{4}$  and similarly, when  $\hat{\mathbf{S}}_1 \cdot \hat{\mathbf{S}}_2 = -\frac{3}{4}$  the energy of the spin singlet state remains [39]. The first term is just a constant, which can be absorbed into other constant energy terms, but the second term is related to the exchange interaction  $J = \frac{E_S - E_T}{2}$  [39]. Thus, the spin-dependent term in the effective Hamiltonian can be written in terms of the exchange interaction

$$\mathcal{H} = -2J\mathbf{S}_1 \cdot \mathbf{S}_2. \quad (2.27)$$

The interactions between all nearest neighbors can be included to describe a system with more than two electrons, which motivates the Hamiltonian for the Heisenberg model [39]

$$\mathcal{H} = - \sum_{ij} J_{ij} \mathbf{S}_i \cdot \mathbf{S}_j. \quad (2.28)$$

Because the summation double counts each pair of spins, the equation must be multiplied by  $\frac{1}{2}$ . Thus, the first term of the spin Hamiltonian comes about by mapping the electronic quantities, such as the direct exchange, onto spin variables [38], where  $J$  can now be considered in the context of the two electron discussion in Section 2.2.2.

Because of the large Coulomb repulsion and well-localized electrons assumed in the Heisenberg model, it is often used to model the magnetic behavior of insulators. In such cases, the interatomic hopping can be treated as a small perturbation to the exchange coupling and Equation 2.19 can be expanded with respect to the

small parameter  $t/U$ , yielding

$$J = J_D - \frac{2t^2}{U}. \quad (2.29)$$

This exchange constant, useful in describing the behavior of Mott insulators such as  $\text{Li}_2\text{IrO}_3$ , indicates that the direct exchange gives a ferromagnetic contribution, while the hopping contributes antiferromagnetically [38]. Also, the competition between the Coulomb repulsion and the interatomic hopping determines the magnitude of the antiferromagnetic component.

## 2.5 The Hubbard Model

When the Coulomb interaction is not quite large enough to localize electrons, hopping occurs and the hybridized wavefunctions may become doubly occupied by electrons. In this limit, an on-site Coulomb interaction will be orders of magnitude more significant than an inter-atomic direct exchange. The idea behind the Hubbard model is to ignore the direct exchange altogether. In which case, it will be the competition between the Coulomb repulsion and the inter-atomic hopping which will determine the exchange interaction

$$\begin{aligned} J &= -\frac{2t^2}{U} && \text{for large } U \\ J &= \frac{U}{4} - |t| && \text{for small } U. \end{aligned} \quad (2.30)$$

The exchange interaction for small Coulomb interactions is determined by an independent electron approximation, where  $U$  and  $J_D$  are treated as small perturbations and the interacting wavefunction is a Slater determinant  $|\psi_1\sigma_1\rangle|\psi_2\sigma_2\rangle - |\psi_2\sigma_2\rangle|\psi_1\sigma_1\rangle$  where  $\psi$  represents the real space part and  $\sigma$  represents the spin.

[38]. This approach allows mapping of the electronic interactions onto a mean interaction field using second quantization and works best for itinerant magnets [38]. When the Coulomb interaction exceeds some threshold value, a transition from conducting to Mott insulating behavior is observed [38] so the Hubbard model is often used to investigate correlation effects. For example, in the undoped cuprates, electron hopping is limited due to the absence of holes on neighboring sites ( $t$  is small compared to  $U$ ), and exchange  $\propto t^2/U$  is discussed.

## 2.6 The Weiss Model of an Antiferromagnet

The previous models can be used to describe the ground state resulting from magnetic interactions on two interpenetrating or bipartite lattices, as encountered in systems such as  $\text{Li}_2\text{IrO}_3$ . The resulting order is an antiferromagnetic ground state where the spins on one sublattice point up and the spins on the other point down. The temperature dependence of this situation can simply, but not always correctly, be considered using the Ising model and a mean field approximation.

The Ising-like antiferromagnetic order on a bipartite lattice can be understood using Equation 2.20, which includes the energy corresponding to exchange between each Ising spin configurations and the energy due to an external field. However, the thermal average of the magnetization of the  $i$ -th spin  $\langle S \rangle$  requires summing over all spin configurations

$$\langle S \rangle = \frac{1}{Z} \sum_{\mu} \exp\left(\frac{-E_{\mu}}{k_B T}\right), \quad (2.31)$$

and this can very quickly become a complicated problem [38]. To simplify matters, the exchange interactions can be incorporated into an effective or mean field on

the  $i$ -th site

$$H_{mf} = \frac{2}{g\mu_o\mu_B} \sum_j J_{ij} S_j \quad (2.32)$$

produced by the neighboring spins. By replacing the exchange interaction with the effective field, the mean field hamiltonian takes the form

$$\mathcal{H}_{MF} = -g\mu_o\mu_B(H + H_{mf}) \sum_i S_i, \quad (2.33)$$

which looks similar to the Hamiltonian of the paramagnet (Equation 2.1), but in a magnetic field  $H + H_{mf}$  [39].

Temperature tends to randomize the spin configurations, whereas the magnetic field acting on each spin due to the neighboring sublattice and an externally applied field act to align spins either with or against the field direction. The magnetization (and the magnetic susceptibility  $\chi = dM/dH$ ) as a function of field and temperature, determined by these competing effects, are now found using the Brillouin function. For a bipartite lattice, the effective field for each sublattice (+ versus -) is entirely due to the magnetization  $M$  resulting from the ordering of the other sublattice

$$\begin{aligned} H_{mf+} &= -|\lambda|M_- \\ H_{mf-} &= -|\lambda|M_+, \end{aligned} \quad (2.34)$$

where  $\lambda$  parameterizes the strength of the effective field and is negative in the case of an antiferromagnet [39]. Because the two sublattices are equivalent except for the direction of the magnetic moments  $|M_+| = |M_-| = M$ , the magnetization

$$M = M_S B_J(y) = M_S B_J \left( \frac{gJ\mu_B J |\lambda| M}{k_B T} \right) \quad (2.35)$$

can be described by the Brillouin function (Equation 2.5) with the effective field incorporated [39]. The form of Equation 2.35 results from considering the case when  $H = 0$ . In this limit, the argument  $y$  is small and  $B_J(y)$  can be approximated using Equation 2.7. The Brillouin Function is plotted in Figure 2.3 for a large value of  $J$ . The equation for  $y$  which incorporates the effective magnetic field

$$y = \frac{g_J \mu_B J (\mu_o H + |\lambda| M)}{k_B T} \quad (2.36)$$

can be used to find  $M$  as a function of  $y$ . For three different transition temperatures  $T$  (different slopes),  $M$  versus  $y$  is plotted in Figure 2.3. The transition temperature can be determined by equating the gradient of the line  $M/M_S$  versus  $y$  with the Brillouin Function at small applied magnetic fields, where  $M_S = n g_J \mu_B J$  is the saturation magnetization. The Néel ordering temperature

$$T_N = \frac{g_J \mu_B (J + 1) |\lambda| M_S}{3k_B} = \frac{n |\lambda| \mu_{eff}^2}{3k_B} \quad (2.37)$$

is found [39]. At temperatures below the ordering temperature, three graphical solutions exist: one unstable solution at  $M_S = 0$  and two stable solutions at non zero values for  $M_S$  corresponding to the ordering of each sublattice in absence of an applied magnetic field (Figure 2.3) [39]. As the temperature is increased, thermal fluctuations start to destroy the magnetization. The order is completely destroyed at  $T = T_N$ . At high temperatures, only one simultaneous solution occurs at  $y = 0$  implying that no magnetic order exists [39]. Above the transition temperature, a small magnetic field can be applied while still maintaining the small  $y$  approximation in the Brillouin function leading to

$$\frac{M}{M_S} \approx \frac{g_J \mu_B (J + 1)}{3k_B} \left( \frac{\mu_o H + |\lambda| M}{T} \right) \approx \frac{T_N}{|\lambda| M_S} \left( \frac{\mu_o H + |\lambda| M}{T} \right). \quad (2.38)$$

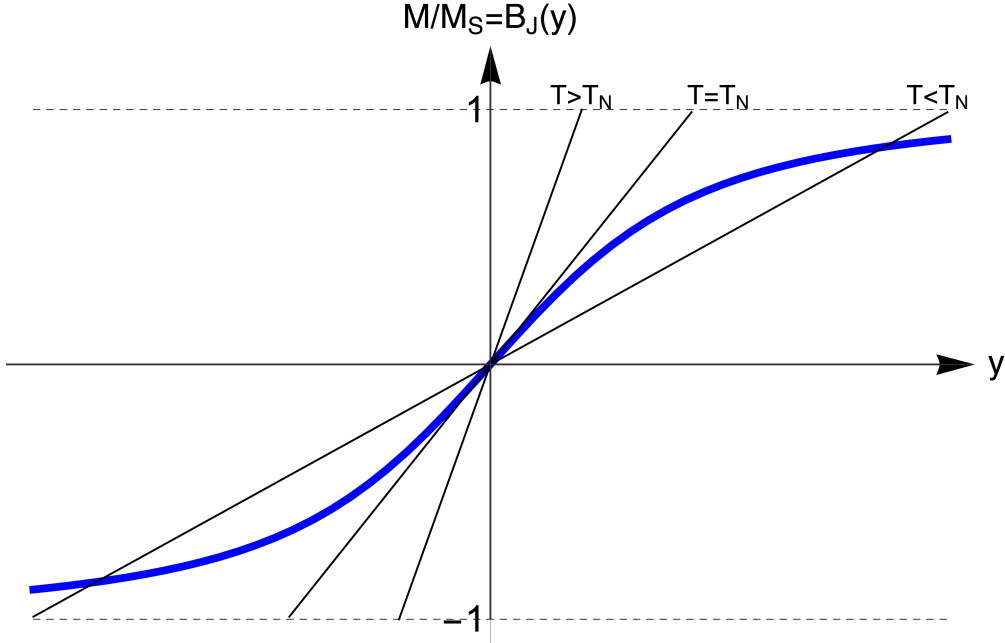


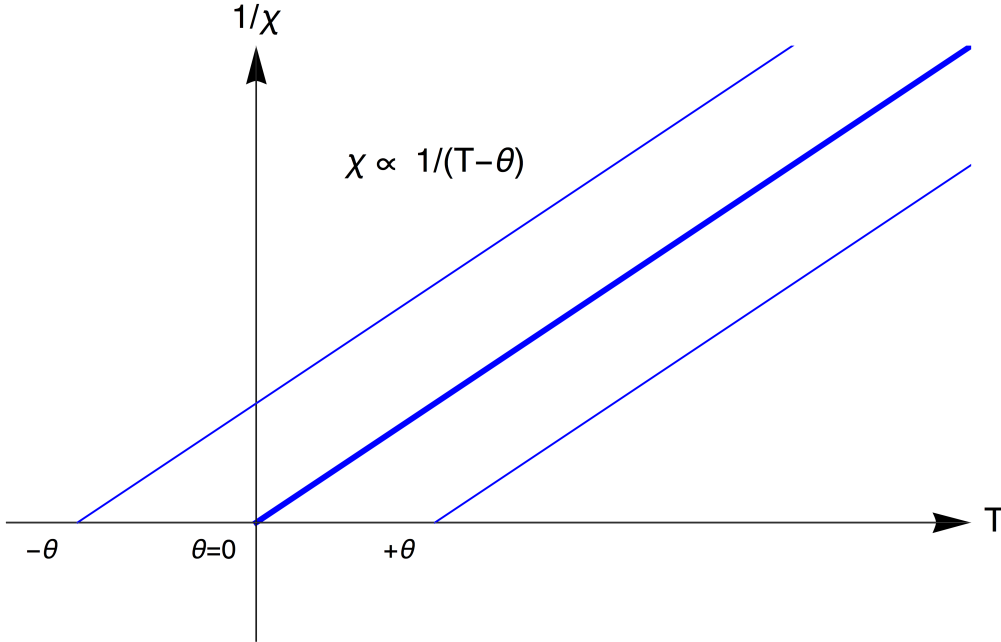
FIGURE 2.3: The Brillouin Function for  $J = 5$  (solid blue curve) and  $M = k_B T y / g_J \mu_B J \lambda$  for varying temperatures (black lines) to show graphically the solutions (points of intersection between black and blue curves) to the two equations. Above the ordering temperature, one solution at  $M = 0$  exists. Below the transition temperature, two stable solutions with a finite magnetization exist in the absence of an applied magnetic field. Figure modified from [39].

At high temperatures and at small applied magnetic fields, the magnetic susceptibility of an antiferromagnet is given by the Curie Weiss law

$$\chi = \lim_{H \rightarrow 0} \frac{M}{H} \propto \frac{1}{T + \theta}, \quad (2.39)$$

where  $\theta$  is known as the Curie temperature [39]. This describes the susceptibility above the ordering temperature, in the paramagnetic regime, so that a fit to the high temperature behavior in  $1/\chi$  versus  $T$  gives a straight line with a temperature intercept (Figure 2.4). In Section 2.1, we found the temperature dependence of the magnetic susceptibility for a noninteracting paramagnet (Equation 2.8). In the case of the paramagnet at high temperatures,  $\chi$  behaves as  $1/T$  with a zero

temperature intercept. A positive temperature intercept is indicative of ferromagnetism with  $\theta = T_C$ , the Curie temperature. A negative temperature intercept implies antiferromagnetism with  $\theta = -T_N$  [39].




---

FIGURE 2.4: The Curie Weiss dependence is shown for three cases: the paramagnet ( $\theta = 0$ ), the ferromagnet ( $\theta > 0$ ), and the antiferromagnet ( $\theta < 0$ ). The temperature intercept gives the Curie temperature  $\theta$ . Figure and caption modified from [39].

The Curie temperature represents a quantitative deviation from paramagnetic behavior providing some insight about the magnitude of the exchange interactions. However, the assumption in this model is that all spins experience the same effective field, which is entirely due to the neighboring sublattice. Second nearest neighbor interactions often result in experimentally determined values of the Curie temperature that can be far from  $-T_N$  so it is not a “smoking gun” [39]. Importantly, the difference between  $|\theta|$  and  $T_N$  are an indication that long range order is suppressed, which could also be due to increased frustration in the exchange interactions or low dimensionality caused by spatially anisotropic exchange. In

any case, in the context of searching for suppressed order and a spin liquid state, a large value of  $|\theta|$  is anticipated.

## 2.7 Superexchange

Superexchange, which was first postulated by Anderson in 1950 [40], is a mechanism which presents the possibility of preferred directionality in the exchange. It describes an indirect interaction between the magnetic atoms via an intervening non-magnetic ion, where the directionality of the exchange is a result of the orientation of the orbitals on the intervening ion. The most common intervening ion is oxygen because it strongly attracts electrons and its bands usually reside below the Fermi energy. Oppositely aligned spins can spread onto the non-orthogonal overlapping  $p$ -orbitals of oxygen to minimize their energy. The mechanism for superexchange is discussed in detail in reference [41] for poorly-conducting transition-metals, suggesting a clear relationship between superexchange and Mott physics. Whenever the Coulomb repulsion dominates and prevents metallic conduction, the opposite tendency to delocalize causes a necessarily antiferromagnetic interaction [41] that is related to the local environment of the magnetic ion. Superexchange is responsible for creating spatial anisotropies in the exchange interactions, and in extreme cases, it resembles a reduced dimensionality of the system.

## 2.8 Spin-Anisotropic Exchange Interactions

In 2005, Doucot *et al.* [42] considered the quantum analog of the compass model on a square lattice, where the coupling takes different values along different spatial directions, and found that all eigenstates must be at least twofold degenerate. Attention placed on this prototypical model has shown that a large degree of exchange anisotropy results in a highly degenerate ground state. The details of

the exact diagonalization, using Monte Carlo simulations and high-order perturbation theory, leading to this conclusion are given in reference [43]. The Kitaev model equivalently considers strong exchange anisotropy as in the quantum compass model, but on a honeycomb lattice with bond-specific Ising spins. The model requires that the three nonequivalent links of the honeycomb lattice, labeled as  $x$ ,  $y$  and  $z$ , couple only those corresponding components of spin [27] (Figure 2.5). For example, only  $S_i^x S_j^x$  couples on the  $x$ -links, and similarly for the  $y$  and  $z$  links (Figure 2.5). Because the direction of the coupling is orthogonal for the three different

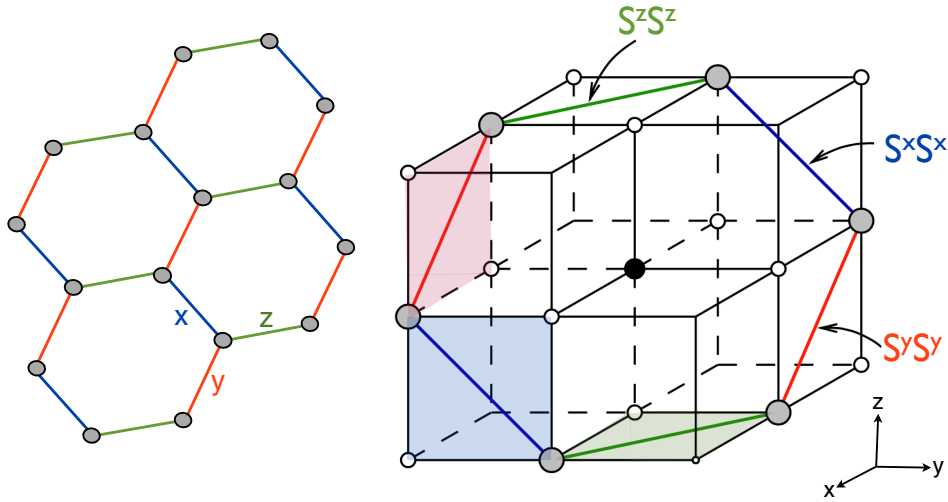


FIGURE 2.5: (Left) The layered honeycomb lattice with three different links labeled as  $x$ ,  $y$ , and  $z$ . (Right) The interactions on the neighboring links of the honeycomb lattice are of  $XX$ ,  $YY$  or  $ZZ$  type, depending upon the direction of the link [27] as presented in the exactly solvable spin model by Kitaev. The coupling on each bond is perpendicular to its corresponding cubic axes. The gray circles (white circles) represent the magnetic (non-magnetic) ions. Figure modified from [28].

links, we call the exchange bond-specific in the Kitaev model, unlike the quantum compass model which considers anisotropy in the exchange interactions that are the same for all spins. The honeycomb lattice with anisotropic, bond-specific exchange interactions can be described with an Ising-like or “Kitaev” term  $S_i^\gamma S_j^\gamma$  in

the Hamiltonian, where  $\gamma = x, y, z$  represent the different links of the honeycomb lattice. For real materials, further interactions will inevitably be present and the spins will not be entirely Ising-like and one might expect that isotropic Heisenberg interactions will compete with the anisotropic Kitaev couplings [30]. This is the essence of what is called the Kitaev model – in the context of spin liquid physics – where contributions from a rotationally symmetric  $\mathbf{S}_i \cdot \mathbf{S}_j$  Heisenberg term and an anisotropic Kitaev term result in the Kitaev-Heisenberg Hamiltonian

$$\mathcal{H}_{ij}^{(\gamma)} = 2K S_i^\gamma S_j^\gamma + J \mathbf{S}_i \cdot \mathbf{S}_j. \quad (2.40)$$

Depending upon the particular lattice geometry under consideration, the extrapolation from the isotropic Heisenberg model to a quantum compass or Kitaev model can be made in Mott systems which have large spin-orbit coupling [28]. In systems where spin-orbit coupling plays a major role, the anisotropy of the coupling in spin space can be related to the orientation of the bonds in real space. For example, by embedding strongly spin-orbit coupled atoms (gray circles in Figure 2.5) on a honeycomb lattice into a face-centered cubic lattice with the relative orientation shown, a bond dependent exchange anisotropy can be engineered if the superexchange is mediated via the two intermediary atoms (white circles) on the face-centered cube. In such a scenario, a plane can be defined by the magnetic atoms on each honeycomb link and the intervening non-magnetic atoms. The resulting planes for the three different bond directions of the honeycomb lattice are orthogonal. In the case of large spin-orbit coupling, the directional dependency of the atomic orbitals can lead to anisotropy in the exchange that depends upon the spatial direction of each particular bond on the honeycomb lattice (Figure 2.5).

## 3

### The Honeycomb Iridates

#### 3.1 Background

The iridates offer an interesting playground to search for novel phases of matter that emerge from the collective behavior of local moments that are strongly influenced by spin-orbit coupling. Some intriguing examples of this interplay include the Mott insulating state originally observed in the layered perovskite  $\text{Sr}_2\text{IrO}_4$  [44] and the topological semimetal realized in the pyrochlore iridate  $\text{Y}_2\text{Ir}_2\text{O}_7$  [45]. The Kitaev model, describing highly anisotropic exchange on a honeycomb lattice, brought the honeycomb iridates into the limelight. Depending upon the spatial anisotropy of the exchange couplings, the model harbors three of the currently most sought-after collective states in condensed matter physics: a gapless spin liquid with emergent Majorana fermion excitations, a gapped spin liquid, and a topologically ordered phase with non-Abelian quasiparticle statistics [30].

Most experimental attention was first placed on  $\text{Na}_2\text{IrO}_3$ , the layered honeycomb structure which was originally predicted to be a quantum spin Hall system [46]. It was quickly established that  $\text{Na}_2\text{IrO}_3$  orders antiferromagnetically at 15 K, a much lower temperature than the paramagnetic Curie temperature of -125 K, implying

that the underlying interactions are strongly frustrated [34, 47, 48]. This type of behavior is expected in the so called Kitaev-Heisenberg model where long range magnetic order is suppressed due to its close proximity to the Kitaev spin liquid state [29]. However, single-crystal neutron and x-ray diffraction data confirmed a “zigzag” magnetic order, an arrangement of ferromagnetic zigzag chains that are antiferromagnetically coupled to each other [48], which was not originally captured within the model. To explain the magnetic order, Chaloupka *et al.* extended the parameter space by allowing  $\phi$  – the relative strength of the Kitaev and Heisenberg-like contributions – to vary from 0 to  $2\pi$  in the Kitaev-Heisenberg Hamiltonian

$$\mathcal{H}_{ij}^{(\gamma)} = A (2 \sin\phi S_i^\gamma S_j^\gamma + \cos\phi \mathbf{S}_i \cdot \mathbf{S}_j). \quad (3.1)$$

Equation 3.1 is the same Kitaev-Heisenberg Hamiltonian of Chapter 2 (Equation 2.40), but with the energy scale  $A = \sqrt{K^2 + J^2}$  and the angle  $\phi$  introduced via  $K = A\sin\phi$  and  $J = A\cos\phi$  [31]. As in Chapter 2,  $\gamma$  represents the three distinct orientations of nearest neighbor bonds on the honeycomb lattice. The phase diagram of the extended Kitaev-Heisenberg model, containing 2 spin liquid and 4 spin ordered phases [31], reveals the zigzag order as a natural ground state (Figure 3.1). Most importantly, the observed zigzag magnetic order lies in close proximity to the spin liquid state, provoking further interest in tuning the anisotropy in the exchange interactions.

Focus turned to the lithium analogue, where the substitution of  $\text{Na}^+$  with  $\text{Li}^+$  was expected to maintain the same local honeycomb structure of the  $\text{Ir}^{4+}$  ions responsible for the exotic magnetism. The smaller ionic radius of the lithium ions was believed to result in smaller octahedral distortions (Section 3.2) and an enhancement of the exchange anisotropy. The successful synthesis of  $\text{Li}_2\text{IrO}_3$  in pure single crystal form posed some difficulties causing most of the earlier measurements to be done through a doping series ( $0 \leq x \leq 0.9$ ) of  $\text{Na}_{1-x}\text{Li}_x\text{IrO}_3$

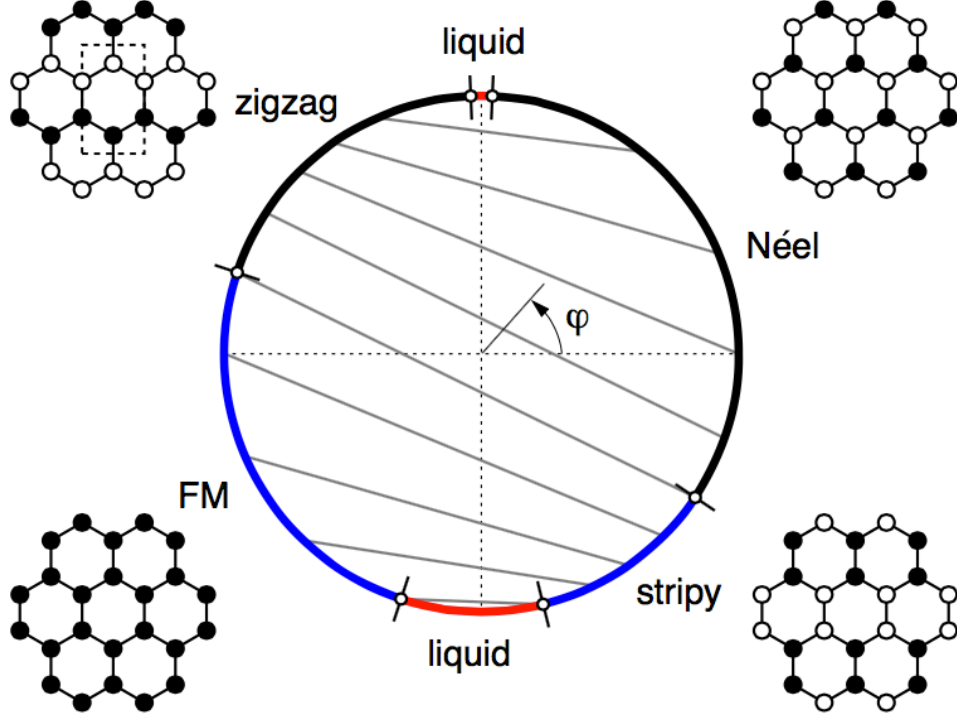


FIGURE 3.1: Phase diagram of the Kitaev-Heisenberg model containing 2 spin liquid and 4 spin ordered phases depending upon the relative strength of the Kitaev and Heisenberg exchange couplings, as represented by the parameter  $\phi$ . Open/solid circles in the insets indicate up/down spins. The rectangular box in zigzag pattern (top-left) shows the magnetic unit cell of  $\text{Na}_2\text{IrO}_3$ . Figure reproduced by [31].

single crystals [49] or on polycrystals of  $\text{Li}_2\text{IrO}_3$  [30]. The magnetic susceptibility of high quality polycrystalline samples of  $\text{A}_2\text{IrO}_3$  ( $\text{A} = \text{Na}, \text{Li}$ ) show an increase in the Curie-Weiss temperature from  $\theta \approx -125\text{K}$  for  $\text{Na}_2\text{IrO}_3$  to  $\theta \approx -33\text{K}$  for  $\text{Li}_2\text{IrO}_3$  with a bulk antiferromagnetic ordering temperature at  $T_N = 15\text{K}$  for both materials (Figure 3.2) [30]. Naively, the reduction in the frustration parameter  $f \approx |\theta|/T_N$  implies that the magnetic interactions are weaker in the lithium compound. However, the two terms in the Kitaev-Heisenberg Hamiltonian (Equation

3.1) enter with opposite coupling signs, suggesting that the effective antiferromagnetic (Heisenberg-like) exchange interactions have weakened when compared to the  $\text{Na}_2\text{IrO}_3$  system [30]. By including further than nearest neighbor antiferromagnetic interactions, which are expected to enhance the geometric frustration, the anomalously large frustration parameter observed in  $\text{Na}_2\text{IrO}_3$  is captured within the Kitaev-Heisenberg model [30]. Furthermore, by modelling the evolution of the Curie-Weiss temperature scale, more support is given that  $\text{Na}_2\text{IrO}_3$  is deep in a magnetically ordered state, while  $\text{Li}_2\text{IrO}_3$  is considerably closer to the spin liquid regime [30].

The preliminary work on  $\text{Na}_2\text{IrO}_3$  and polycrystalline  $\text{Li}_2\text{IrO}_3$  gave a major boost to the synthesis community to successfully produce  $\text{Li}_2\text{IrO}_3$  in single crystal form. This resulted in the simultaneous surfacing of two different three-dimensional honeycomb structures (Section 3.2). It was soon established that both structures order magnetically at  $T_N \approx 38$  K, presumably owing to their higher dimensionality [35, 50]. The Mermin-Wagner theorem states that long-range fluctuations are favored in systems of dimension  $d \leq 2$  so that no phase transition will occur at finite temperature. Despite the confirmed phase transition in the  $\text{Li}_2\text{IrO}_3$  structures, no previous measurements explored the magnetic anisotropy, particularly in the search for bond-dependent Kitaev-type exchange interactions. This thesis studies one of the three-dimensional honeycomb structures of  $\text{Li}_2\text{IrO}_3$ , the exact details of which are given in the next section.

### 3.2 Three-Dimensional Honeycomb Structure of $\text{Li}_2\text{IrO}_3$

The single crystals of  $\text{Li}_2\text{IrO}_3$ , making up a large portion of the work studied in this thesis, were synthesized by James Analytis and his group at UC Berkeley and the crystallographic x-ray data was done by Radu Coldea and his group at the

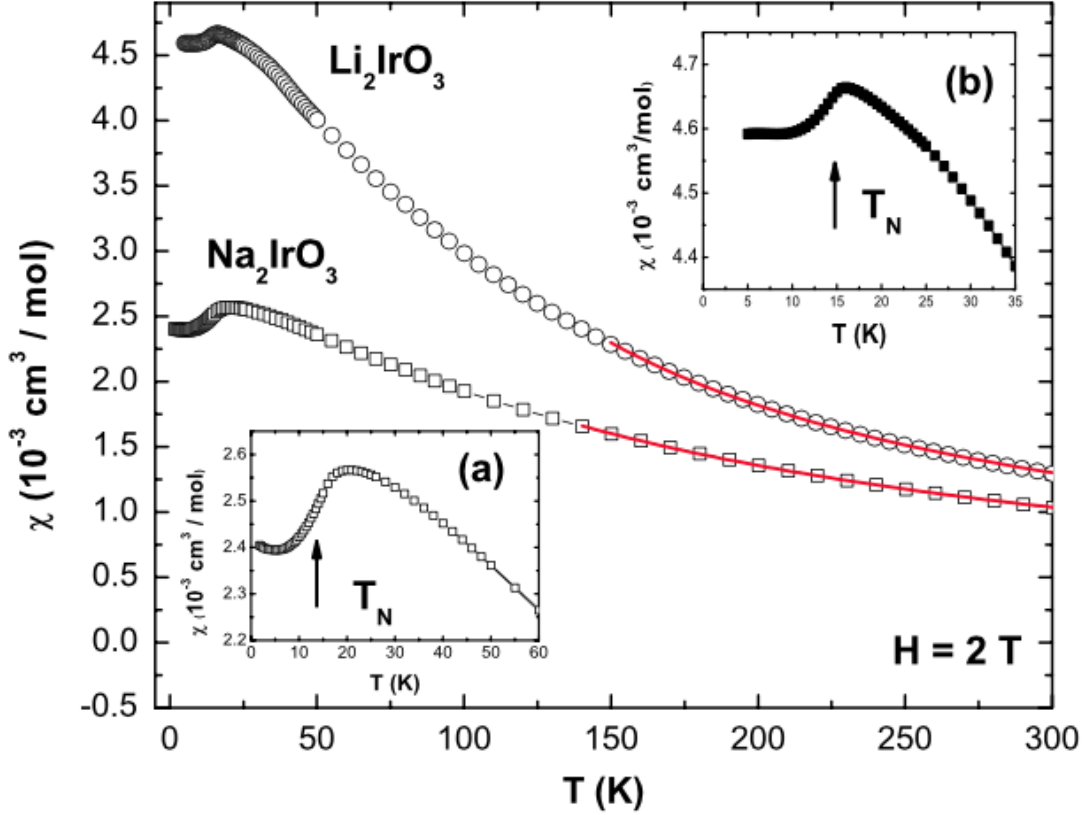
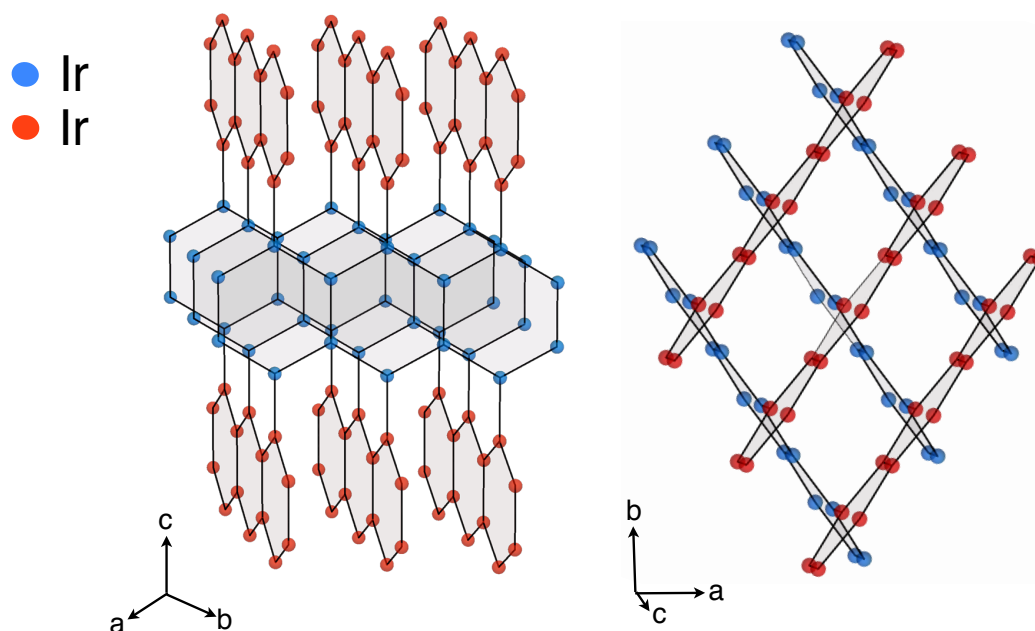


FIGURE 3.2: Magnetic susceptibility  $\chi$  versus temperature  $T$  for  $A_2\text{IrO}_3$  ( $A = \text{Na}, \text{Li}$ ). The fit by the Curie-Weiss expression  $\chi = \chi_o + C/(T - \theta)$  is shown as the curve through the data. The insets (a) and (b) show the anomaly at the antiferromagnetic ordering for the Na and Li systems, respectively. Figure and caption reproduced by [30].

University of Oxford. The synthesis methods and the details of solving the crystal structure are contained in the supplementary information of reference [35].

The structural findings are that  $\text{Li}_2\text{IrO}_3$  is an orthorhombic crystal belonging to the non-symmorphic space group  $C_{2cm}$ . The lattice parameters are  $a = 5.9119(3) \text{ \AA}$ ,  $b = 8.4461(5) \text{ \AA}$ , and  $c = 17.8363(10) \text{ \AA}$ , with 16 iridium atoms occupying the unit cell [35]. The iridium atoms (red and blue spheres in Figure 3.3) maintain the same local connectivity as a layered honeycomb structure, but they make up

a three-dimensional framework. There are two interlaced honeycomb planes with




---

FIGURE 3.3: Two different views of the three-dimensional honeycomb structure of  $\text{Li}_2\text{IrO}_3$ . The colored spheres represent the hexagonal arrangement of the iridium atoms with the red and blue colors used to show that alternating rows of honeycombs along the crystallographic  $c$  axis lie in different crystal planes.

an alternating orientation along the crystallographic  $c$  axis (honeycomb planes distinguished by the red and blue colors). If one considers only the vertical link that connects a red and blue iridium and the nearest neighbors of each, some key features of this three-dimensional honeycomb structure become apparent. First, each iridium lies in a three-fold, planar environment with three equidistant nearest neighbor iridium. This is illustrated by the red and blue shaded triangles in Figure 3.4. Second, the three-fold coordination of neighboring  $\text{IrO}_6$  octahedra share an edge, as highlighted by the solid red and blue lines in Figure 3.4. Finally and

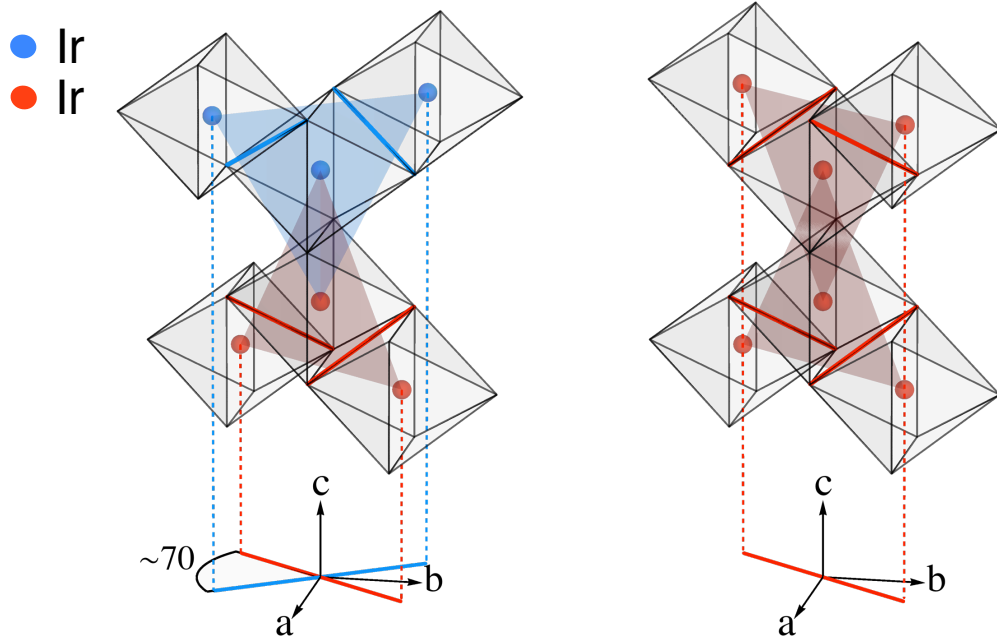
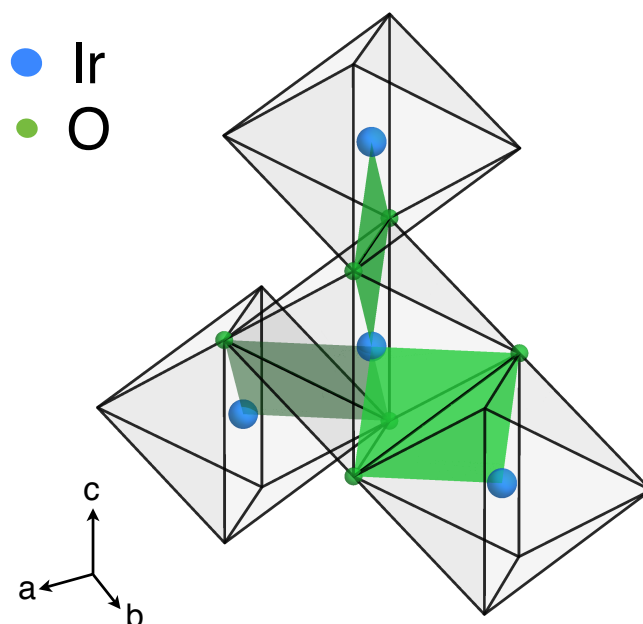


FIGURE 3.4: Left: Edge shared octahedral environment of the three-fold, planar iridium-iridium bonds in  $\text{Li}_2\text{IrO}_3$ . The octahedra are nearly undistorted giving rise to a  $70^\circ$  angle separating the two honeycomb planes, distinguished by red and blue colors. Right: Edge shared octahedral environment of the iridium-iridium bonds that constitute the layered honeycomb structure.

perhaps most importantly, the octahedra are nearly perfect and have negligible distortion [51] unlike the layered  $\text{Na}_2\text{IrO}_3$  structure, which experiences a substantial trigonal distortion of its octahedral complexes [34, 48]. This significant departure from ideal  $90^\circ$  Ir-O-Ir bonds in  $\text{Na}_2\text{IrO}_3$  is believed to be the cause for the deviation from dominant Kitaev exchange, where the spin liquid state is expected to emerge [28]. For all purposes of our understanding, we assume the octahedra in the  $\text{Li}_2\text{IrO}_3$  structure to be undistorted and this has several important consequences.

The edge shared property of the undistorted octahedra fixes the angle separating




---

FIGURE 3.5: The undistorted octahedra create Ir-O<sub>2</sub>-Ir exchange pathways (green planes) between all nearest neighbor iridium.

the two honeycomb planes due to the possibility of two locally indistinguishable Ir-Ir bonds. For example, if the vertical link between the red and blue atom is made (left side of Figure 3.4), the top two iridium atoms have the option to link to the center blue iridium in one of two ways: through the solid blue edges of the top center octahedra in the left panel of Figure 3.4 or through the two opposing edges of the top center octahedra on the right of the figure. The latter option continues the orientation of the honeycombs in the same plane, constituting the layered honeycomb structure. In the three-dimensional structure, the geometry of the undistorted, edge shared octahedra constrains the angle separating the two honeycomb planes to be  $\sim 70^\circ$ , as shown by the red and blue lines drawn on the

axes in Figure 3.4. This angle separating the honeycomb planes manifests itself in the crystal morphology and is responsible for the high temperature anisotropy in the magnetic susceptibility (Chapter 6).

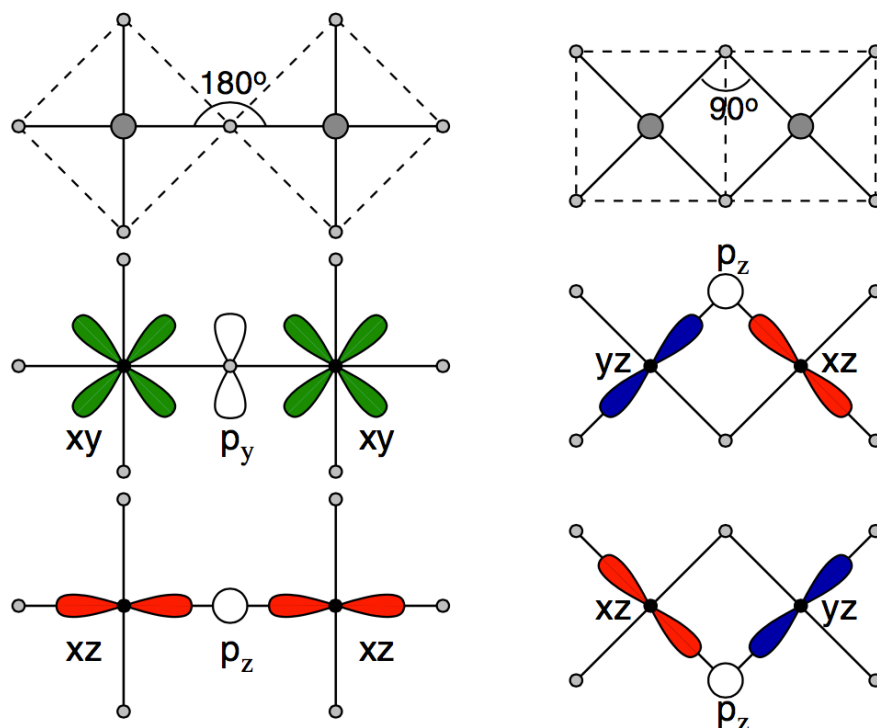


FIGURE 3.6: The possible geometries of a TM (transition metal)-O-TM bond with corresponding orbitals active along these bonds. The large (small) dots represent the transition metal (oxygen) ions. (Left): A  $180^\circ$  bond formed by corner-shared octahedra, and (right) a  $90^\circ$  bond formed by edge-shared octahedra. Figure and caption reproduced from [28].

The undistorted octahedral environment is also responsible for maintaining equidistance between all nearest neighbor iridium and requires that the exchange pathways between each is the same. The superexchange pathway between neighboring iridium is mediated by two oxygen which make up an Ir-O<sub>2</sub>-Ir plane (Figure 3.5) between all nearest neighbor iridium. There are only two active *d*-orbitals for any

given Ir-Ir bond in the edge-shared octahedral environment. The right side of Figure 3.6 shows that a  $90^\circ$  Ir-O-Ir bond will have hopping matrix elements which are nondiagonal because the  $d_{yz}$ -orbital on one atom is active with the  $d_{xz}$ -orbital on the other atom in one exchange pathway, whereas in the corner-sharing octahedra (left side), the interactions take place between the same orbitals on each magnetic atom.

The two transfer amplitudes in the edge-sharing octahedra, via the upper and lower oxygen, will interfere in a destructive manner [28]. In the limiting case, the only non-vanishing interaction is for the spin component normal to the Ir-O<sub>2</sub>-Ir plane, leading to extreme spin-anisotropy of the exchange coupling. The most important observation to notice is that the exchange interaction depends upon the spatial orientation of each of the three different bonds and the undistorted property of the octahedra causes the normals of the Ir-O<sub>2</sub>-Ir planes to define three orthogonal directions on the nearest neighbor bonds that coincide with the direction of the spin-exchange on each bond. This observation is the key ingredient of the Kitaev model [28] and will play an integral role in understanding the low temperature magnetic properties of Li<sub>2</sub>IrO<sub>3</sub> (Chapter 6).

Finally, the extent to which the iridium bond according to the two possibilities in Figure 3.4 suggests the possibility of an entire family of honeycomb structures (Figure 3.7) [35]. Each member of this structural family is denoted by the  $c$  axis extent of complete honeycomb rows which have the same orientation. The Li<sub>2</sub>IrO<sub>3</sub> structure studied in this thesis has been referred to as  ${}^{\mathcal{H}}\langle N \rangle$ -Li<sub>2</sub>IrO<sub>3</sub>, with  $N = 1$ , implying that there is one complete honeycomb row which is linked along the  $c$  axis to another complete honeycomb row that lies in a different plane as the first [35]. It has also been labelled as the “stripyhoneycomb” and  $\gamma$ -Li<sub>2</sub>IrO<sub>3</sub>. The end members of this series include the layered honeycomb,  ${}^{\mathcal{H}}\langle \infty \rangle$ -Li<sub>2</sub>IrO<sub>3</sub> [51] and the hyperhoneycomb structure,  ${}^{\mathcal{H}}\langle 0 \rangle$ -Li<sub>2</sub>IrO<sub>3</sub>. It is important to note that each member of this

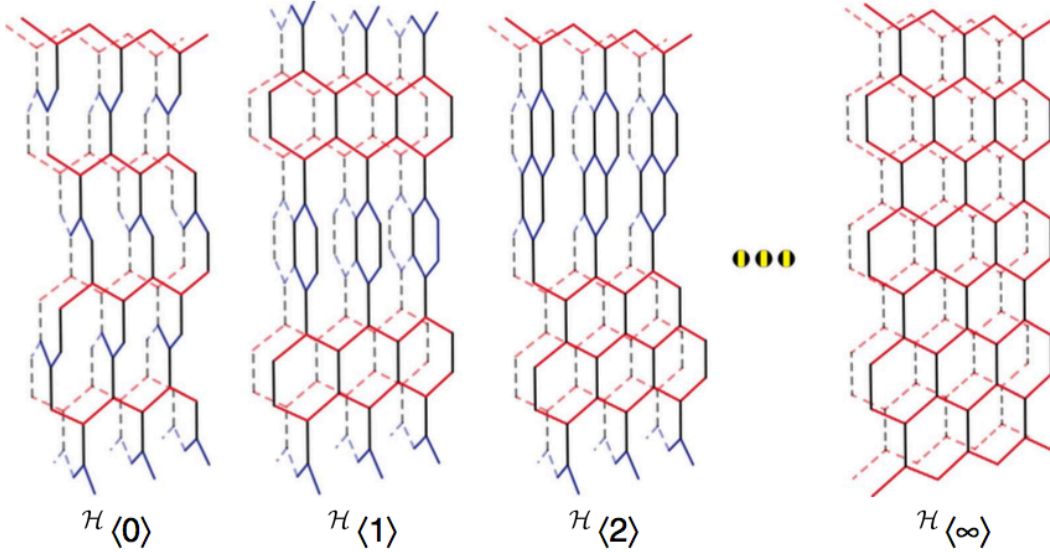


FIGURE 3.7: The locally indistinguishable Ir-Ir bonds due to the undistorted octahedra can be used to construct a series of structures  $\mathcal{H}\langle N \rangle$ - $\text{Li}_2\text{IrO}_3$ , where  $N$  counts the number of complete honeycomb rows along the  $c$  axis before the orientation of the honeycomb plane switches. Figure and caption reproduced by [35].

family preserves the edge shared and undistorted octahedral environment, making the  $70^\circ$  angle between the honeycomb planes a universal feature. Each member of the structural series, however, will be affected by next nearest neighbor exchange differently, offering a route to search for new and unusual magnetic structures.

The edge sharing property of the octahedra in this structural family is analogous to the corner-sharing octahedra in the Ruddlesden-Popper family. Despite the fact that each member of the Ruddlesden-Popper family is locally identical in structure (each iridium is in a planar environment with its three nearest neighbors separated by  $120^\circ$  degrees), there is a rich variety of exotic states which emerge, including superconductivity and ferromagnetism in the ruthenates, colossal magnetoresistance

in the manganites and multiferroic behavior in the titanates [35]. Not only does this family of honeycomb structures provide an opportunity to explore strongly spin-orbit coupled Mott insulators in the search for new states of matter, but the edge sharing geometry of the octahedra is the integral property of the Kitaev model making each member a material candidate for the realization of a quantum spin liquid. The implications of the structural characteristics of  $\mathcal{H}\langle 1 \rangle$ - $\text{Li}_2\text{IrO}_3$  referred to hereafter as  $\text{Li}_2\text{IrO}_3$ , are discussed in the following section.

### 3.3 Crystal Field and Spin Orbit Effects

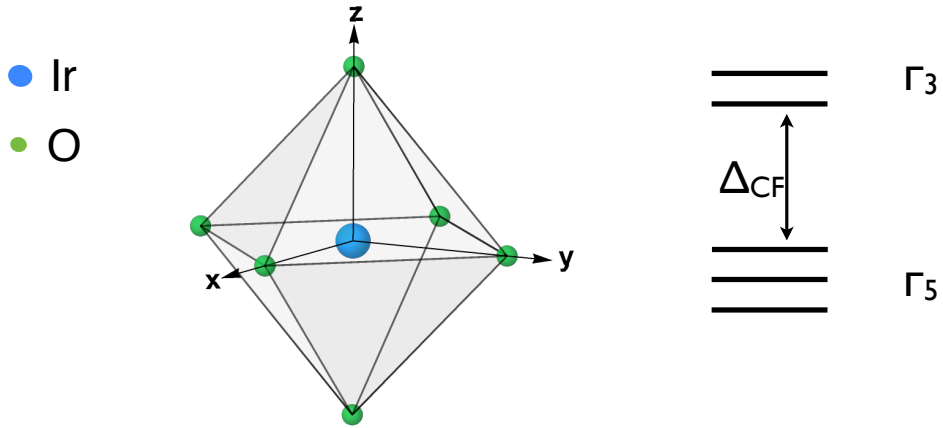
In addition to the intrinsic spin ( $S = 1/2$ ) of each electron, another source of magnetism is the induced magnetic moment arising from the orbital motion of each electron about its nucleus. This can be visualized as a loop of current, which can be affected by the electric field produced by a surrounding charge distribution in the crystal – the ‘crystal field’. The orbital and spin contributions can often lead to an “effective” magnetic moment of the electron, allowing it to take values other than  $1/2$ . The crystal field then, and consequently the magnetic properties, are critically dependent upon the symmetry of the local environment.

The symmetry of the local environment alone can provide a tremendous amount of information about the electronic structure and its interaction with a magnetic field. The mathematical tool for extracting that information is the theory of group representations. In this section, it will be used to find the lowest energy eigenstates of  $\text{Li}_2\text{IrO}_3$  and determine qualitatively the effects of the spin-orbit interaction and the Coulomb interaction. A brief interlude is first taken to familiarize the reader with the key terms and concepts used in group and representation theory that will aid in the discussion that follows.

Abstractly, a group is defined as a set of distinct elements which satisfy the following properties; 1) a law of composition (such as addition, multiplication, matrix multiplication etc.) of two elements in a group result in an element which also belongs to the group 2) an identity element belongs to the group whose composition with each element does not change the element 3) there exists an inverse for each element of the group and the composition of that element and its inverse results in the identity and 4) the law of composition of the group elements is associative (e.g.  $a(b + c) = ab + ac$ ) [52]. A simple example of a group are the real numbers 1 and -1, with multiplication as the law of composition. The groups of particular interest to the discussion of the iridates are symmetry transformations, such as rotations, reflections, and translations that leave the physical system invariant [52]. This group of transformations which act on the physical system can be represented by a collection of matrices, known as a representation of the group. By means of a similarity transformation, unitary matrices can be found along with an orthonormal set of basis functions, which can characterize a state of the system. The matrices that represent all of the transformations in the group are referred to as a representation of the group. To remove any extraneous information about the symmetry of the system, the representation can be expressed as a linear combination of its irreducible representations. Thus, the irreducible representations are the smallest necessary subsets of information which can completely describe the system based on symmetry arguments alone. Each irreducible representation can be expressed as a matrix or as in our case, a set of orthonormal basis functions and every state of the system can be described as a linear combinations of these eigenfunctions.

As discussed in the previous section, each iridium is positioned at the center of an octahedra with oxygen at each vertex. This octahedral environment, familiar to many transition metal complexes, lifts the degeneracy of the  $d$ -shell ( $l = 2$ )

orbitals on iridium. The octahedron, which is the dual polyhedron of a cube, can be described by the cubic group  $O$ . For a cubic environment, the  $d$ -orbitals split into two irreducible representations or multiplets; the first are most commonly known as the  $t_{2g}$  orbitals with lobes which point *between* the  $x$ ,  $y$  and  $z$  axes and the second are referred to as the  $e_g$  orbitals which point *along* the same axes [39]. For the remainder of this discussion, the notation of Abragam and Bleaney [53] will be used so that  $t_{2g}$  will be called  $\Gamma_5$  and  $e_g$  will be referred to as  $\Gamma_3$ . The crystal field is mainly due to the  $p$ -orbitals of oxygen, which in an octahedral environment, extend along the direction of the  $\Gamma_3$  orbitals. Thus, the  $\Gamma_3$  multiplet has a greater Coulomb repulsion with the  $p$ -orbitals and is less energetically favorable. Therefore, in an octahedral environment, the  $\Gamma_5$  triplet is lower in energy than the  $\Gamma_3$  doublet (Figure 3.8). The difference in energy between the  $d$ -orbital multiplets – the crystal field splitting – is denoted as  $\Delta_{CF}$ . The stoichiometric compound  $\text{Li}_2\text{IrO}_3$  has an  $\text{Ir}^{4+}$  ion in a  $5d^5$  configuration, which




---

FIGURE 3.8: The  $\text{IrO}_6$  coordination splits the orbital degeneracy of the iridium  $d$ -shell by some energy  $\Delta_{CF}$ . The energy level schematic shows the  $\Gamma_5$  triplet lower in energy than the  $\Gamma_3$  doublet.

leads to a single hole in the  $\Gamma_5$  multiplet. For the discussion of the iridates, a large crystal field splitting is assumed and attention can now be restricted to  $\Gamma_5$ . A

basis for the three orbital wavefunctions that span  $\Gamma_5$  can be chosen as  $\eta_x$ ,  $\eta_y$  and  $\eta_z$ , transforming as the  $d_{yz}$ ,  $d_{zx}$  and  $d_{xz}$  orbitals, respectively. Again, following the notation of Abragam and Bleaney [53], a “fictitious angular momentum” basis can be defined

$$\begin{aligned} |\widetilde{+1}\rangle &= \eta_{+1} = \frac{-\eta_x - i\eta_y}{\sqrt{2}} \\ |\widetilde{0}\rangle &= \eta_0 = \eta_z \\ |\widetilde{-1}\rangle &= \eta_{-1} = \frac{\eta_x - i\eta_y}{\sqrt{2}}. \end{aligned} \quad (3.2)$$

Inclusion of the two possible spin states  $|\uparrow\rangle = |+1/2\rangle$  and  $|\downarrow\rangle = |-1/2\rangle$ , which form the irreducible representation  $\Gamma_6$ , results in six single-electron states in the  $\Gamma_5$  multiplet. In a cubic environment, this product is reducible and separates into a doublet and a quadruplet [53]

$$\Gamma_5 \times \Gamma_6 = \Gamma_7 + \Gamma_8, \quad (3.3)$$

where  $\Gamma_8$  transforms as a spin  $\frac{3}{2}$  and  $\Gamma_7$  transforms under rotations of a cube as a “fake” spin  $\frac{1}{2}$ . The wavefunctions in  $\Gamma_7$  and  $\Gamma_8$  are defined via Clebsch-Gordan

coefficients for the cubic group

$$\begin{aligned}
 |\Gamma^7\rangle_2 &= -i\sqrt{\frac{1}{3}}|\eta_x \downarrow\rangle + \sqrt{\frac{1}{3}}|\eta_y \downarrow\rangle - i\sqrt{\frac{1}{3}}|\eta_z \uparrow\rangle \\
 |\Gamma^7\rangle_1 &= -i\sqrt{\frac{1}{3}}|\eta_x \uparrow\rangle - \sqrt{\frac{1}{3}}|\eta_y \uparrow\rangle + i\sqrt{\frac{1}{3}}|\eta_z \downarrow\rangle \\
 \\ 
 |\Gamma^8\rangle_4 &= i\sqrt{\frac{1}{6}}|\eta_x \uparrow\rangle + \sqrt{\frac{1}{6}}|\eta_y \uparrow\rangle + i\sqrt{\frac{2}{3}}|\eta_z \downarrow\rangle \\
 |\Gamma^8\rangle_3 &= -i\sqrt{\frac{1}{2}}|\eta_x \downarrow\rangle - \sqrt{\frac{1}{2}}|\eta_y \downarrow\rangle \\
 |\Gamma^8\rangle_2 &= i\sqrt{\frac{1}{2}}|\eta_x \uparrow\rangle - \sqrt{\frac{1}{2}}|\eta_y \uparrow\rangle \\
 |\Gamma^8\rangle_1 &= -i\sqrt{\frac{1}{6}}|\eta_x \downarrow\rangle + \sqrt{\frac{1}{6}}|\eta_y \downarrow\rangle + i\sqrt{\frac{2}{3}}|\eta_z \uparrow\rangle. \tag{3.4}
 \end{aligned}$$

The spin orbit interaction  $\mathcal{H}_{SO} = \lambda_{SO}\vec{S}\cdot\vec{L}$  (where  $\vec{S}$  and  $\vec{L}$  are angular momentum operators acting on the spin and orbital parts of the wavefunctions respectively) lifts the degeneracy of the  $\Gamma_7$  and  $\Gamma_8$  multiplets. To determine which multiplet is lower in energy, the matrix elements must be calculated using the operator  $\vec{S}\cdot\vec{L} = S_xL_x + S_yL_y + S_zL_z = \frac{S_-L_+ + S_+L_-}{2} + S_zL_z$ . The operators  $S_+, S_-, L_+, L_-$  are the raising and lowering operators, which entered from

$$\begin{aligned}
 S_x &= \frac{S_+ + S_-}{2} \\
 S_y &= \frac{S_+ - S_-}{2i}
 \end{aligned} \tag{3.5}$$

and can be written similarly for  $L_x$  and  $L_y$ . As an example, the wavefunction  $|\Gamma^8\rangle_4$  can be rewritten as

$$|\Gamma^8\rangle_4 = -i\frac{1}{\sqrt{3}}|1\rangle|\uparrow\rangle + i\frac{1}{\sqrt{3}}|2\rangle|\downarrow\rangle - i\frac{1}{\sqrt{3}}|-2\rangle|\downarrow\rangle, \tag{3.6}$$

with use of Equation 3.2 and the following  $\Gamma_5$  states

$$\begin{aligned} |\widetilde{+1}\rangle &= |-1\rangle \\ |\widetilde{0}\rangle &= \frac{|2\rangle - |-2\rangle}{\sqrt{2}} \\ |\widetilde{-1}\rangle &= -|1\rangle \end{aligned} \quad (3.7)$$

which correspond to the decomposition of the cubic representation of  $l = 2$  [53].

The matrix element

$${}_4\langle\Gamma^8|\lambda_{SO}\vec{S}\cdot\vec{L}|\Gamma^8\rangle_4 = -\frac{\lambda_{SO}}{2} \quad (3.8)$$

is found using the eigenvalues of  $J_z = m$ , along with those of the raising and lowering operators

$$\begin{aligned} J_+|j\ m\rangle &= \hbar\sqrt{j(j+1)-m(m+1)}|j\ m+1\rangle \\ J_-|j\ m\rangle &= \hbar\sqrt{j(j+1)-m(m-1)}|j\ m-1\rangle. \end{aligned} \quad (3.9)$$

Calculation of the matrix elements for each state

$$\begin{aligned} {}_i\langle\Gamma^7|\lambda_{SO}\vec{S}\cdot\vec{L}|\Gamma^7\rangle_j &= \lambda_{SO} \begin{bmatrix} 1 & 0 \\ 0 & 1 \end{bmatrix} \\ {}_i\langle\Gamma^8|\lambda_{SO}\vec{S}\cdot\vec{L}|\Gamma^8\rangle_j &= -\lambda_{SO}\frac{1}{2} \begin{bmatrix} 1 & 0 & 0 & 0 \\ 0 & 1 & 0 & 0 \\ 0 & 0 & 1 & 0 \\ 0 & 0 & 0 & 1 \end{bmatrix} \end{aligned} \quad (3.10)$$

yields the spin orbit splitting  $\Delta E_{SO} = 3/2\lambda_{SO}$ . Thus, four electrons will occupy the lower  $\Gamma_8$  multiplet with a single electron occupying  $\Gamma_7$ . Both the  $\Gamma_7$  and  $\Gamma_8$  multiplets will split under the action of a magnetic field due to the Zeeman

interaction  $\mathcal{H}_{\text{Zeeman}} = \vec{M} \cdot \vec{H} = (g_L \vec{L} + g_S \vec{S}) \cdot \vec{H}$ , where  $g_L$  and  $g_S$  represent the orbital and spin contributions to the  $g$ -factor, respectively. The effective  $g$ -factors calculated for each multiplet are

$$\begin{aligned} g_{\Gamma^7} &= \frac{4g_L + g_S}{3} \\ g_{\Gamma^8} &= \frac{-2g_L + g_S}{3}. \end{aligned} \quad (3.11)$$

Alternatively, the  $d^5$  configuration can be considered as a single hole in the  $\Gamma_5$  (six electron states) multiplet. Now, the spin orbit interaction will have opposite sign to the above discussion causing  $\Gamma_7$  to be lower in energy than  $\Gamma_8$ . Either way, the result is a singly occupied  $\Gamma_7$  state (which effectively transforms as a spin  $\frac{1}{2}$ ). This effective spin  $\frac{1}{2}$  state on iridium is responsible for the magnetism in both the sodium and lithium iridate compounds. In  $\text{Li}_2\text{IrO}_3$ , the possibility of lithium deficiency would lead to an  $\text{Ir}^{5+}$  valence state with four electrons on the  $d$  shell. This scenario is treated in Appendix A. It is encouraging to note that the same  $\Gamma_7$  and  $\Gamma_8$  wavefunctions of Equation 3.4 were obtained by first considering five electrons on the  $d$ -shell of iridium in empty space where the wavefunctions of the 3/2 and 5/2 multiplets are well-defined by the Clebsch Gordan coefficients. Then, the octahedral environment further reduces the 5/2 representation into  $\Gamma_7$  and  $\Gamma_8$  (Figure 3.9). This exercise is carried out in Appendix B and is instructive in understanding how the symmetry of irreducible representations constrain the mixing of electronic states.

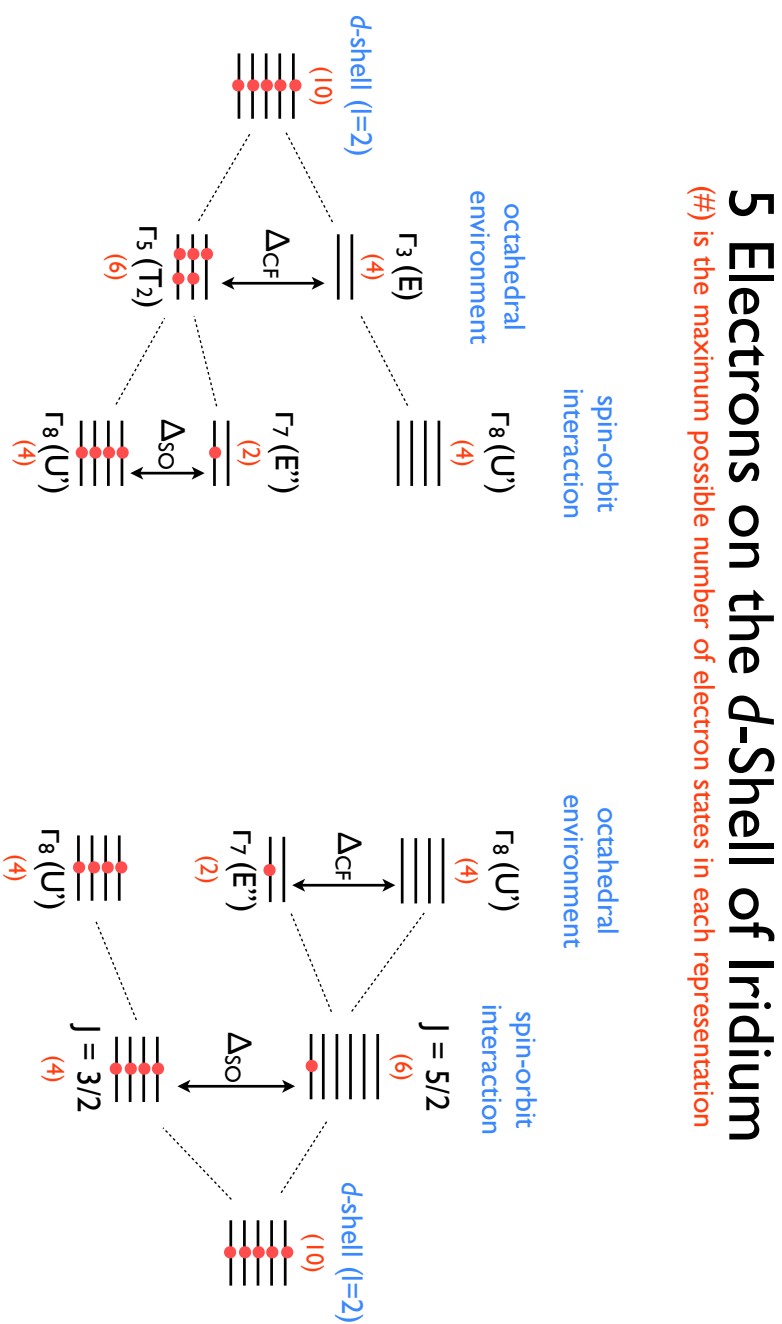


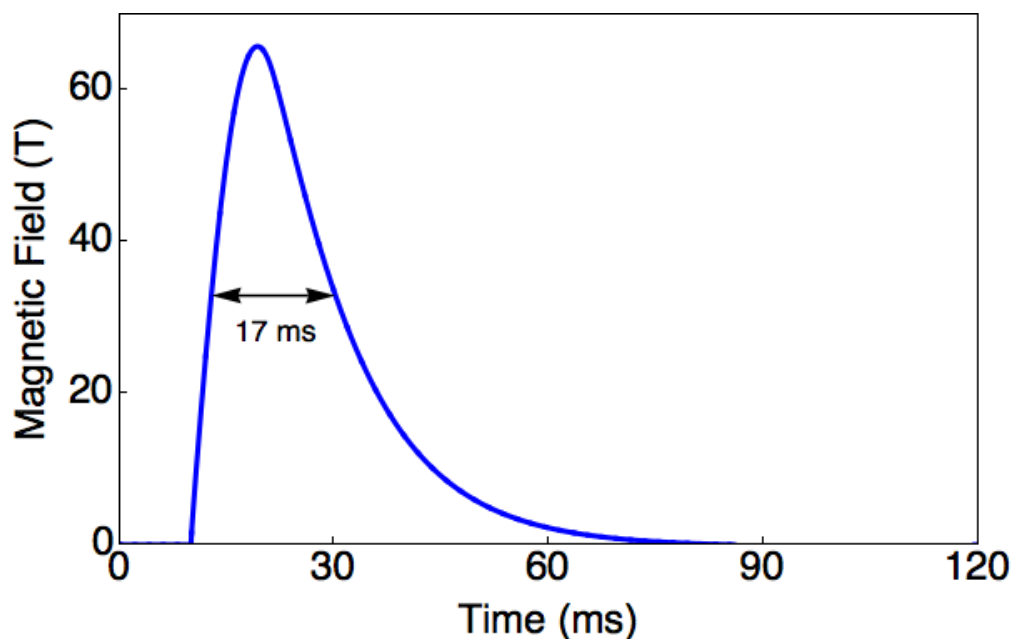
FIGURE 3.9: The irreducible representations that arise due to the symmetry of the octahedral environment and the spin-orbit interaction. The red dots represent the occupied states of five electrons on the  $d$ -shell of iridium.

## Experimental Techniques

### 4.1 Pulsed Magnetic Fields

As most of the data was taken at the Pulsed Field Facility of the National High Magnetic Field Laboratory, it is appropriate to discuss some of the experimental advances and challenges in the specialized work of pulsed magnetic field measurements. High pulsed magnetic fields are achieved by discharging a large capacitor bank through a resistive coil of copper wire. Magnetic fields of 65 T are regularly obtained by charging the capacitor bank to 8.11 kV, at which point a mechanical switch closes to make electrical contact from the capacitors to the copper coil. 1.6 MJ of energy is discharged to the coil whose resistive and inductive elements create a sinusoidal magnetic field profile (Figure 4.1). At about 20 ms into the pulse, the maximum magnetic field is reached and the switch disconnects the coil from the capacitor bank and shortcircuits the coil to a shunt. The current decays exponentially to zero for the remainder of the pulse. This behavior is typical of a simple LR circuit and is well represented in the magnetic field profile (Figure 4.1).

The world record setting non-destructive magnet at the NHMFL at LANL was used to measure  $\text{Li}_2\text{IrO}_3$  to magnetic fields up to 90 T. The magnetic field profile for



---

FIGURE 4.1: The magnetic field profile for the 65 T short-pulse magnet with an 8 ms rise time. The total duration of the magnetic field pulse is about 90 ms.

the 100 T pulsed field magnet is shown in Figure 4.2. The total pulse duration is 3 seconds, with much of this time spent ramping up the outer coil set of the magnet to a field of 39 T with 300 MJ of energy that is delivered by a 1.4 GJ generator. Inside of the generator-driven magnet, a capacitor bank-driven 65 T short-pulse magnet is housed. Once a magnetic field of 39 T is reached, at approximately 1.5 seconds into the pulse, the capacitor bank is discharged to reach fields above 100 T in about 8 ms. To significantly reduce the stress on the magnet, it is routinely operated to fields of 90 T.

The large discharge of energy used to create such high magnetic fields causes mechanical vibration and heating and makes it very challenging to reduce noise in the electrical circuitry of the experiments. This, along with the fact that the entire 65 T magnetic field pulse is over in 100 ms, makes clean data acquisition

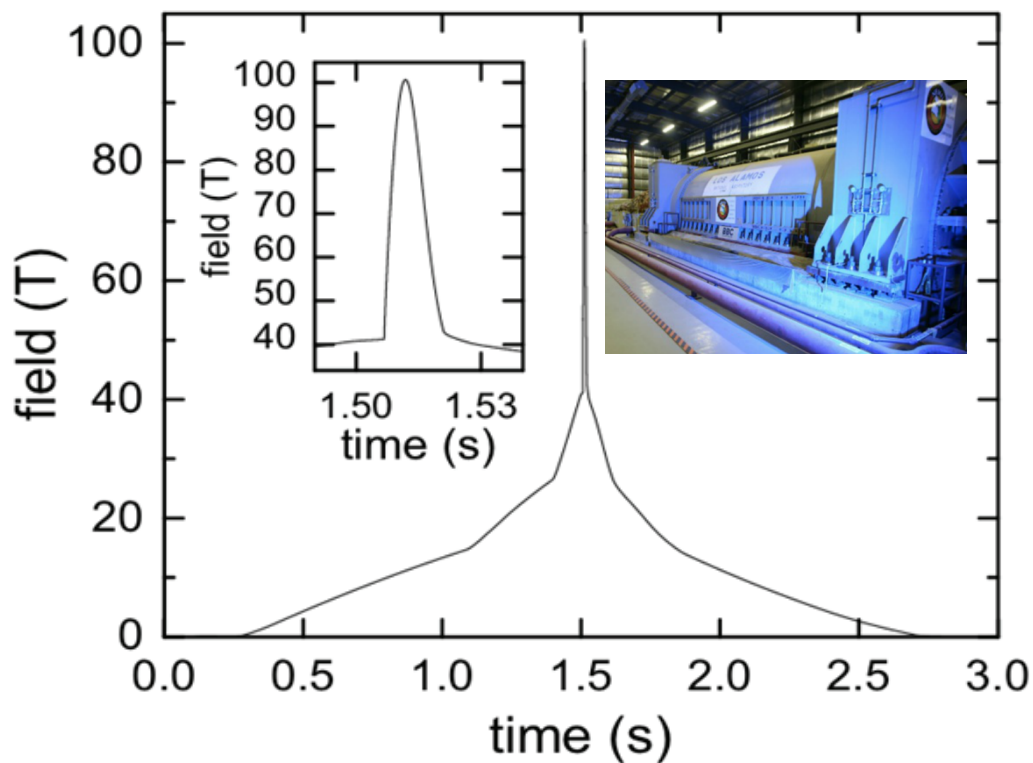


FIGURE 4.2: The magnetic field profile for the 100 T pulsed field magnet with a total pulse duration of 3 seconds. The outer coil set of the magnet is generator-driven to a magnetic field of 39 T. When this field is reached, the capacitor bank discharges 1.6 MJ of energy to the insert coil, producing a magnetic field of 100 T. Left inset: Field profile focused on the 40-100 T range. Right inset: A picture of the generator used to power the 100 T pulsed field magnet. Figure modified from [62].

a difficult problem. At the Pulsed Field Facility, several steps are taken to try to improve the ratio of signal to noise during the measurements and accurately stabilize temperature during the magnetic pulse.

### 4.1.1 Temperature Control

The copper coil which makes up the magnet is cooled to 77 K in liquid nitrogen. The cryostat used for the experiment is inserted directly into the bore of the magnet. It is typically filled with liquid helium for most experiments which must be done at low temperatures and is surrounded by a vacuum jacket. Temperatures as low as 1.5 K can be reached by pumping on this main bath of liquid helium. The probe, which holds the sample, thermometer and all measurement wires resides in a separate space inside a stainless steel fridge with a vacuum jacket, which is then inserted in the cryostat for better thermal control of the sample environment. For low temperatures, the probe is inserted directly into liquid  $^3\text{He}$  or  $^4\text{He}$  and temperatures can be precisely controlled by regulating the vapor pressure of the exchange gas above the liquid. For most measurements, even at higher temperatures,  $^3\text{He}$  or  $^4\text{He}$  exchange gas will be used as a means of thermal equilibration inside the sample space. For most of the torque measurements, we found that having the sample and the lever in liquid  $^3\text{He}$ , which is more viscous at low temperature, allows for less vibration during the pulse and cleaner data.

### 4.1.2 Data Acquisition

The Pulsed Field Facility uses synchronous digital lock-in software that was designed in-house and offers several advantages over conventional lock-in amplifiers. First, the digital lock-in can operate at very high signal frequencies and sampling rates, which is necessary for pulsed field measurements where the magnetic pulse is over in less than a tenth of a second. Secondly, the synchronous digitizer captures as much information as possible during the pulse and all typical lock-in functions are applied reversibly to the data afterwards in software. With a magnet cool

down time of approximately 45 minutes, it is crucial to limit any irreversible loss of information in data acquisition.

For pulsed field measurements, a sine wave is synthesized along with a clock signal that is an integer multiple of the signal frequency. The sample response to the generated signal is sent to the differential front end of a Stanford Research Systems SR560 low noise preamplifier, which amplifies the signal with gain of 100 (Figure 4.3). Just as the capacitor bank discharges through the magnet, a signal is sent to trigger National Instruments data acquisition cards that record the torque signal voltage as a function of time, as well as the pickup voltage from two different coils used for measuring the time response of the magnetic field and the angle. The data acquisition cards are triggered with time stamps specified by the clock at a very high sampling rate of approximately 20 MHz in order to reconstruct the torque signal as a function of magnetic field. After the experiment, the lock-in software digitally multiplies the input signal and the reference signal and then integrates over a user-specified time constant, which acts as a low pass band filter and the contribution from any signal that is not at the same frequency as the reference signal is attenuated. Similarly, the reference is adjusted with a 90° phase shift and the multiplication and integration are repeated to obtain both in-phase and quadrature signals. With a conventional lock-in, the time constant is chosen beforehand such that noise reduction occurs at the expense of response time causing an unavoidable time delay in the output. With the synchronous digital lock-in, data can be reanalyzed multiple times with adjustments made to the time constant, phase shift, and filtering after the measurement while avoiding any delays in the signal response.

It is important to compare data taken during both the rise and fall of magnetic field as it often provides information about temperature control during the pulse. However, voltages induced by a large  $\frac{dB}{dt}$  (Section 4.1.3) at the beginning of the

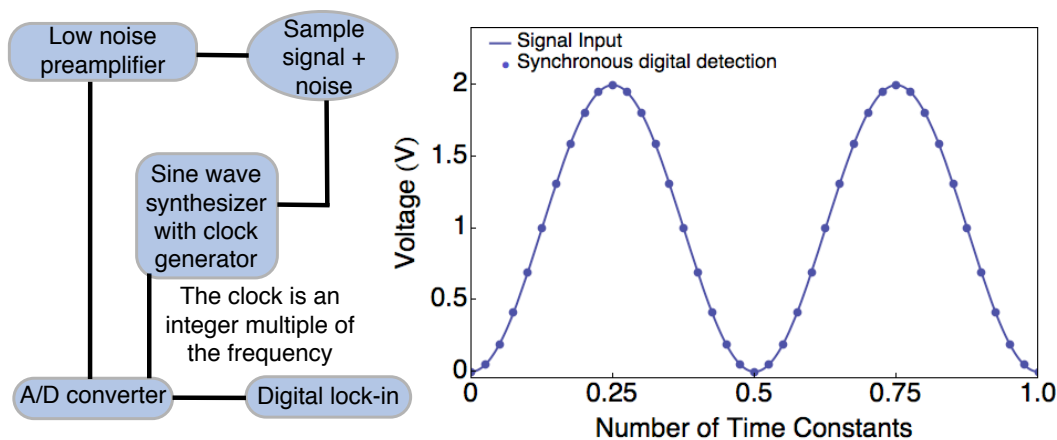


FIGURE 4.3: Left: Schematic of the pulsed magnetic field data acquisition with synchronous lock-in processes. Right: Sine wave representing the signal input and the synchronous digital detection with a sampling rate is an integer multiple of the signal frequency. Figure modified from [54].

pulse result in electrical noise during the up sweep so only the down sweep data is used. Also, the fall of magnetic field occurs more slowly than the rise, allowing more data points and better averaging to be acquired on the down sweep. The electrical noise during the up sweep of the magnetic field can be significantly reduced with careful design of the measurement probe (Section 4.1.4).

### 4.1.3 Field and Angle Control

The rotator probe (Section 4.1.4) houses two copper pickup coils with a known number of turns; one located at the very bottom of the probe used to measure the magnetic field during the pulse and determine the position of field center, and the other located on the sample platform used to determine the angle of the sample with respect to magnetic field. The Maxwell-Faraday Law  $\Delta \times \vec{E} = -\frac{\partial \vec{B}}{\partial t}$  describes

an electric field induced by a time-dependent magnetic field. Stoke's theorem can be used to transition to the intergral form

$$\oint_{\partial S} \vec{E} \cdot d\vec{l} = - \frac{d}{dt} \int_S \vec{B} \cdot d\vec{A}, \quad (4.1)$$

where the integral on the right hand side gives the magnetic flux  $\Phi$  through a surface S [55]. The magnetic flux of a loop of wire with area  $A$  in a magnetic field  $\vec{B}$  is  $\Phi = BA\cos\theta$  with  $\theta$  defined as the angle between  $\vec{B}$  and the vector normal to the area enclosed by the loop of wire. By considering a coil with  $N$  turns of wire, integration over the left hand side of Equation 4.1 will give the pickup voltage

$$V = - NA\cos\theta \frac{dB}{dt} \quad (4.2)$$

from the projection coil that can be used to determine the magnitude of the magnetic field [55]. The pickup voltage for a 65 T pulse is plotted as a function of time in Figure 4.4. Integration of the measured voltaged over some time  $t$  is directly proportional to the magnetic field (Figure 4.1).

A smaller magnetic field projection coil resides on the reverse side of the sample platform to measure the angle of the sample stage, and hence the sample, with respect to the applied magnetic field (Figures 4.6 and 4.7). Just as with the fixed pickup coil, the area and the number of turns of the smaller projection coil are known and the voltage is integrated to yield the magnetic field measured by the sample stage coil. When the rotating projection coil has the same orientation as the fixed pickup coil, the vector normal to the area enclosed by each loop is parallel to the applied field ( $\theta = 0^\circ$  in Equation 4.2) and a maximum voltage is measured. As the platform is rotated from this orientation, the voltage measured in Equation 4.2 will be a function of  $\theta$ . A fixed area and number of turns for each coil allows one to use the ratio of the magnetic field measured by the rotating and the fixed

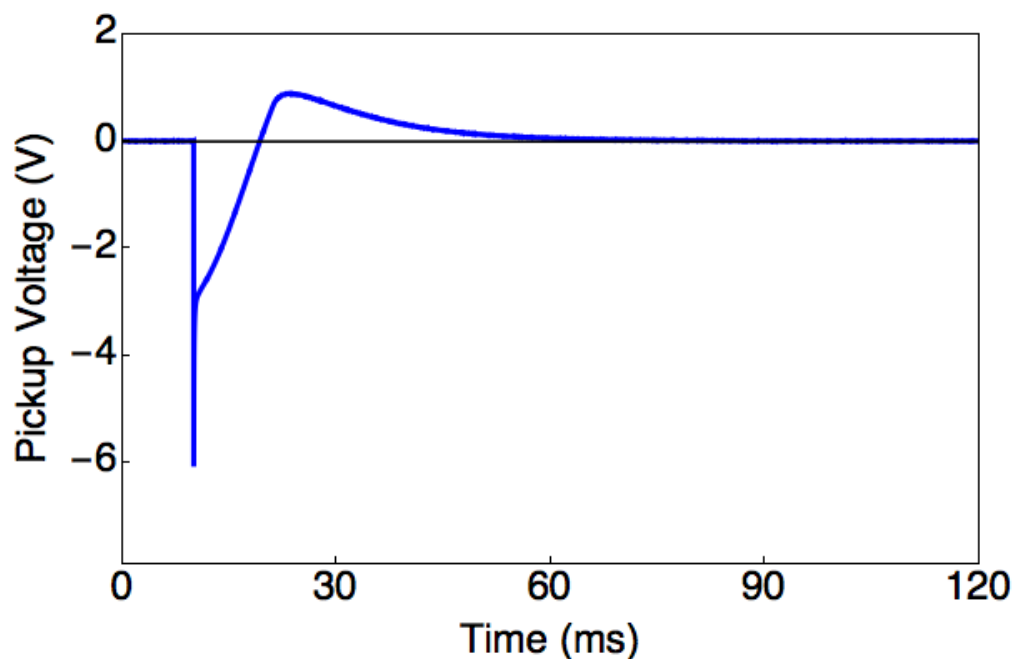


FIGURE 4.4: The pickup voltage from the main field pickup coil used to measure the magnetic field as a function of time.

projection coil to accurately determine the angle

$$\theta = \cos^{-1} \left( \frac{B_{rotator}}{B_{fixed}} \right) \quad (4.3)$$

of the platform with respect to the applied magnetic field (Equation 4.3).

Before each experiment, the pickup coil or the platform projection coil can also be used to determine the position of magnetic field center (Figure 4.5) by driving an AC current through the magnet coil and searching for the maximum voltage as the probe is raised and lowered. Any nonuniformity of the magnetic field can cause a force on a magnetic sample that can affect the overall torque signal, making it particularly important to position the sample in field center to minimize the magnetic field gradient.

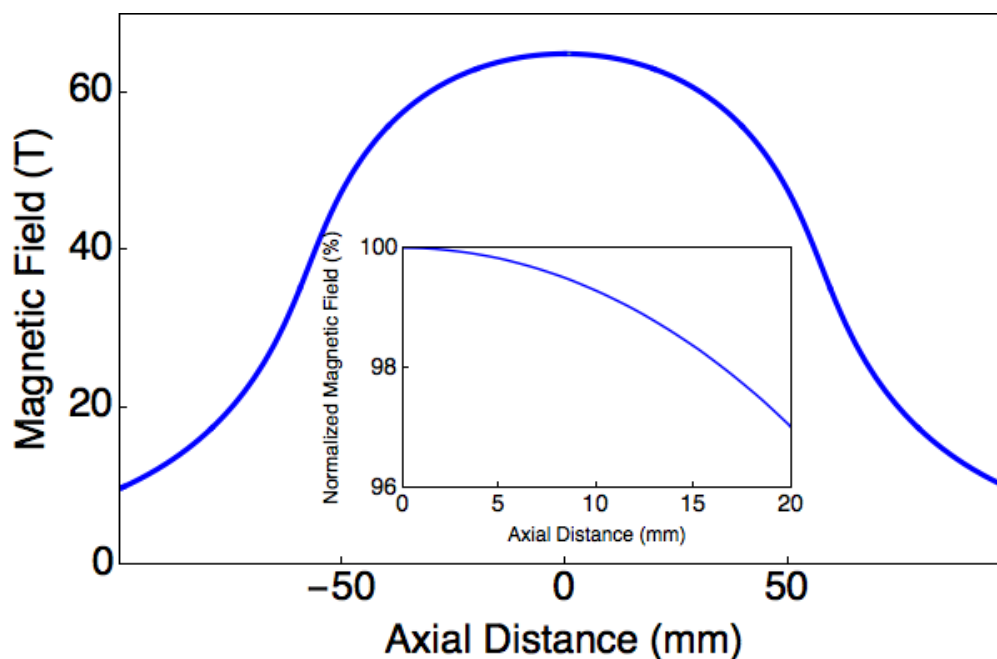
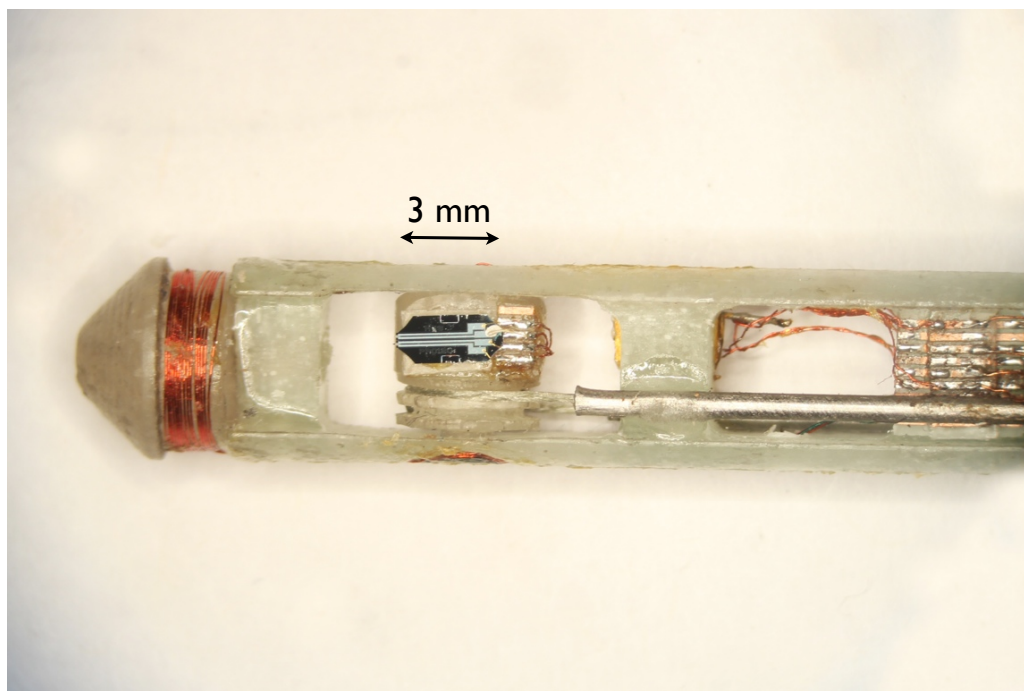


FIGURE 4.5: The 65 T magnetic field profile as a function of axial distance ( $\hat{z}$  direction) symmetrically calculated around field center (0 mm). The inset shows a 3 percent reduction in magnetic field at a distance 20 mm from the center of the magnet.

#### 4.1.4 100 T Rotator Probe

For angle dependent information, the sample is rotated on the probe with respect to the external field between magnetic field sweeps and the measurement will be repeated. The probe is essentially a long support rod with the sample on one end, which is inserted into the magnet. All wires that are needed for collecting data are run up the length of the probe from the sample end (Figure 4.6) to the equipment above the magnet. The single-axis rotator probe described in this section was built by me specifically for use in the 100 T magnet, but was also used for the 65 T pulsed field torque measurements.

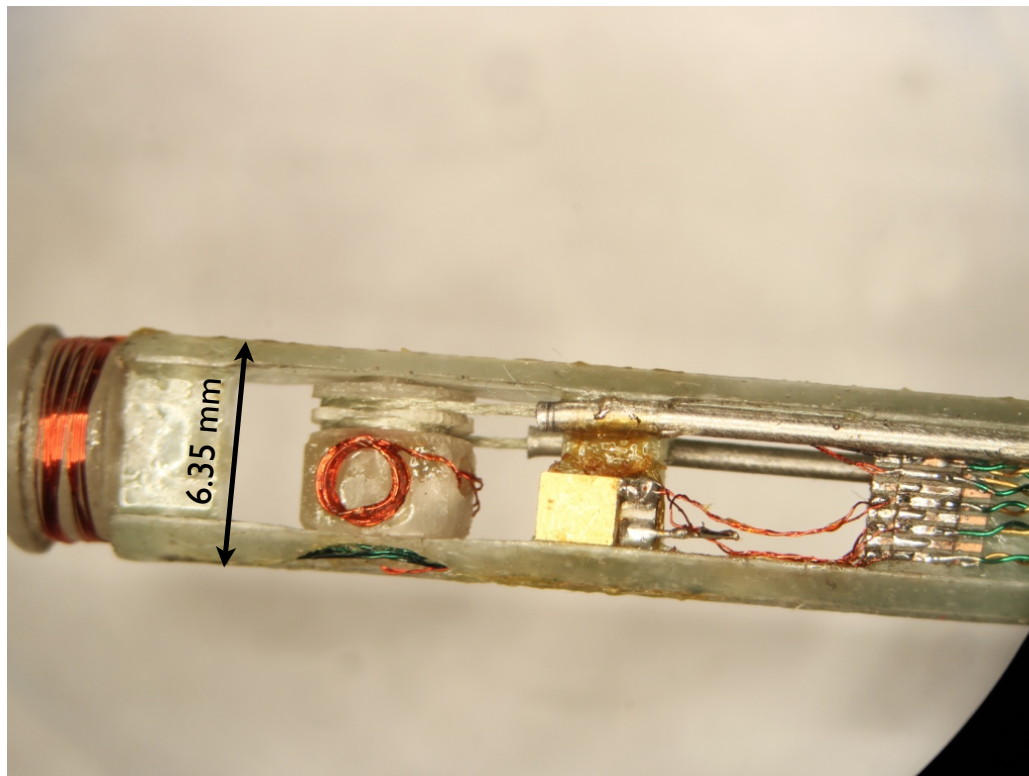


---

FIGURE 4.6: The bottom of the 100 T single axis rotator probe with the lever side visible on the platform. The breakout pad on the sample stage (center) is used to make electrical connection to samples mounted on the platform. The breakout pad out the right disconnects wires running along the length of the probe from wires running along the outside where they are more likely to need replacement. The TUF-Line string is free to move in the stainless steel tube along the bottom right. The fixed angle pickup coil is on the left.

The basic components of the probe include a rotating sample platform, a thermometer, a heater, a magnetic field pickup coil, and a rotating magnetic field projection coil, all of which are in close proximity to the sample. The probe is made of a strong type of fiber-reinforced plastic called G-10. It is approximately 100 inches in length and narrows down to a diameter of 1/4 inch at the bottom to fit inside the bore of the 100 T magnet.

A groove cut into one side of the G-10 platform (Figure 4.7) fixes a TUF-Line



---

FIGURE 4.7: The reverse side of the 100 T rotator probe. Phosphor bronze twisted pairs run along the length of the probe to a breakout pad, which makes electrical connection to the thermometer, the heater, and both projection coils via copper twisted pairs. The rotating projection (center left) lies opposite the lever and the sample on the platform. The Cernox thermometer is to the right of the rotating platform.

string in place that is responsible for rotating the platform. One end of the string is connected to a linear feed at the top of the probe, allowing for rotation in situ, and the other end is attached to a spring at the midpoint, which provides tension on the string. The string is run through a stainless steel tube for protection as it slides along the length of the probe. A Cernox thermometer is mounted directly above and as close as possible to the sample platform to provide the most accurate temperature reading of the sample (Figure 4.7). The heater is made of a

high resistance ( $\approx 50 \Omega$ ), green Manganin wire that winds around both the sample platform and the thermometer to provide even heat distribution (Figure 4.8). A Neocera LTC-21 temperature controller is routinely used to read the temperature and control the heater power.



---

FIGURE 4.8: The side view of the 100 T rotator probe shows the heater (green wire) surrounding the sample and thermometer space. The hollow cylindrical pin in the center lets copper wires pass through the rotation axis of the platform to make connections to the rotating projection coil and the sample.

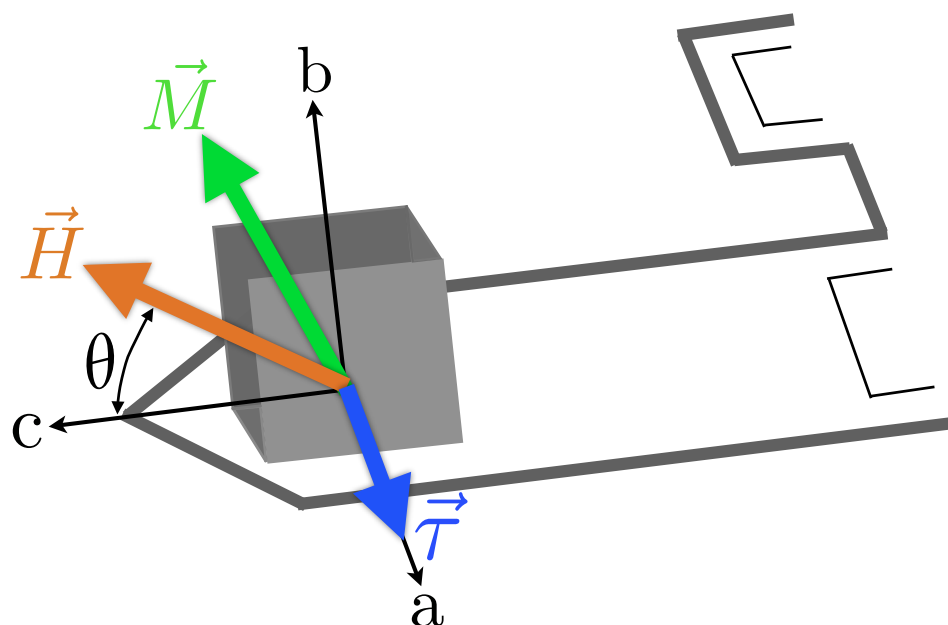
Insulated twisted pairs of copper wire are used to carry the measurement signal along the length of the probe from the reference lever and the sample lever. Each twisted pair is wound tightly to eliminate any open loop area perpendicular to field through which changing magnetic flux can induce large voltages and pick up electrical noise (Section 4.1.3). Each pair is covered with Apiezon N Grease, which freezes at low temperature, and runs through a grounded stainless steel tube for electrical shielding from the other pairs of wires. The stainless steel tubes are glued into place along the length of the probe with GE varnish to reduce vibration

during the pulse. Breakout pads are used at two places on the probe near the sample end (Figure 4.6) to allow for connections to new samples to be made easily without unwiring the entire probe. One breakout pad is on the sample platform and the other is before the opening on the right in Figure 4.6. The opening can be used to mount samples along the sides of the G-10 walls to do fixed angle measurements. All twisted pairs from the larger breakout pad exit through a small hole in the side of the probe and are glued in place along the outside of the G-10 with GE varnish. Similarly, on the reverse side of the probe (Figure 4.7), five twisted pairs of phosphor bronze wires, which are slightly more substantial and have a low thermal conductivity compared to the copper wires, run along the length of the probe to connect to the thermometer, heater, and both field pickup coils. To avoid damage to the wires during rotation, a hole is drilled through the center of the rotation axis of the platform that allows the rotating projection coil and sample wires to pass through (Figure 4.8).

### 4.2 Torque Magnetometry

Torque magnetometry is a highly sensitive technique that is uniquely equipped to probe magnetic anisotropy. A magnetically anisotropic material experiences a torque  $\vec{\tau}$  when its magnetization  $\vec{M}$  is not aligned with the applied magnetic field  $\vec{H}$ ,  $\vec{\tau} = \vec{M} \times \vec{H}$  (Figure 4.9). When the applied magnetic field is parallel to a principal magnetization axis, the resulting torque will be zero. The intrinsic magnetic properties of very small single crystals, on the order of  $\sim 10 \mu\text{m}^3$ , can be measured in pulsed magnetic fields by mounting the sample directly on a piezoresistive microcantilever. As the crystal tries to align its magnetic axes with the applied field, a torque is generated by the sample that is transmitted to the lever. The mechanical stress of the flexing lever is detected by the piezoresistive path and measured as a change in resistance. With careful alignment of a single crystal

on the lever, an angle dependence of the magnetic torque can yield the principal magnetic axes, as well as the differences between the principle components of the magnetic susceptibility – referred to as the principal components of magnetic anisotropy.




---

FIGURE 4.9: Schematic of a magnetically anisotropic sample oriented on a cantilever in an external magnetic field. Rotation of the lever with the sample in this orientation will provide the magnetic anisotropy in the  $b$ - $c$  plane .  $\theta$  denotes the degree of rotating the crystallographic  $\hat{c}$  axis from the direction of the applied magnetic field  $\vec{H}$ .

The cantilever magnetometry technique offers several advantages over more conventional magnetometry methods. First, cantilever magnetometers can detect a magnetic moment,  $m = 10^{-14}$  Am<sup>2</sup> at 1 T making them roughly two orders of magnitude more sensitive than the best commercial SQUID magnetometers [56].

The deflection of the lever can be measured capacitively, optically, or piezoresistively and the preferred method may vary depending upon the particular experiment. Piezoresistive cantilevers are particularly attractive for pulsed magnetic field measurements and the fabrication process is well-established. The cantilever is designed with a high eigenfrequency for fast response in transient magnetic fields, which also aids in reducing electrical noise from low frequency mechanical vibrations [57]. Unlike most magnetometry methods which require the growth of large single crystals to detect small magnetic moments, the small dimension and mass of the cantilever makes it possible to adequately resolve the magnetic anisotropy of very small single crystals at all temperatures. Finally, as magnetic torque measurements access magnetic anisotropy directly, small changes in the magnetic anisotropy can be resolved even when the individual magnetic susceptibilities are large. Thus, torque magnetometry is an invaluable thermodynamic probe that has compatibility with high magnetic fields, making it a particularly well-suited technique to measure the magnetic anisotropy of the first single crystals of  $\text{Li}_2\text{IrO}_3$ , where the exchange anisotropy is expected to couple to spatial anisotropy.

Torque measurements on  $\text{Li}_2\text{IrO}_3$  were performed in a 20 T superconducting magnet designed by Oxford Instruments, and in the capacitor bank-driven 65 T and the generator and capacitor bank-driven 100 T pulsed field magnets at the NHMFL in Los Alamos. The experimental details for each of these measurements are largely the same and outlined below. Some modifications, such as data acquisition and probe wiring are necessary for noise reduction in the pulsed field magnets and these are discussed in Section 4.1. The experimental setup, which can typically resolve a torque signal on the order of  $10^{-14}$  Nm in the DC magnets and  $10^{-13}$  Nm in the pulsed magnets, is explained in more detail by Ohmichi and Osada [57].

A commercial silicon piezoresistive microcantilever fabricated by Seiko Instruments

Inc. (Figure 4.10) is used in our measurements. It was originally designed for the noncontact mode in AFM measurements [57]. The principal bending mode of the cantilever has an eigenfrequency of  $\sim 300$  kHz ( $\sim 3$   $\mu$ s), providing a sufficiently fast response for a pulsed magnetic field which has an 8 ms rise time (Section 4.1). With a sample loaded on the lever, the frequency response can be as low as  $\sim 10$  kHz for samples as large as 1  $\mu$ g [58]. In such cases, it is important to reduce the size of the sample to increase the response time during the magnetic pulse. This cantilever is 120  $\mu$ m long with a piezoresistive path that can sensitively detect mechanical stress of the lever. Residing on the same platform is another piezoresistive path to a shorter reference lever, which lies in the same experimental environment (far left side of Figure 4.10). Both levers are part of a Wheatstone bridge circuit, which uses the signal from the reference lever to null out the thermal and magnetic background of the sample lever, allowing small changes in the torque due to the samples magnetic response to be measured. The single crystal is directly mounted on the tip of the lever with silicon grease and is too small to be seen in Figure 4.10.

For a typical torque measurement in pulsed magnetic fields, an AC voltage source will send  $2 V_{\text{RMS}}$  at a frequency of 59.7 kHz through a 325  $\Omega$  resistor and a 40:1 transformer to maintain a constant current of  $\sim 150$   $\mu$ A. The current is sent to each lever, making up two legs of the Wheatstone bridge circuit (Figure 4.11). The measured output voltage  $\delta V$  (at points A and B in the circuit diagram) from the bridge is sent to the differential front end of a Stanford Research Systems SR844 RF lock-in amplifier. The voltage signal from the lock-in amplifier, a direct measurement of the change in resistance due to the mechanical torque of the lever, accurately displays the magnitude and sign of the sample's magnetic torque during the field sweep. Before each measurement and at zero magnetic field, the bridge is balanced with a potentiometer to null the background from the torque signal. The

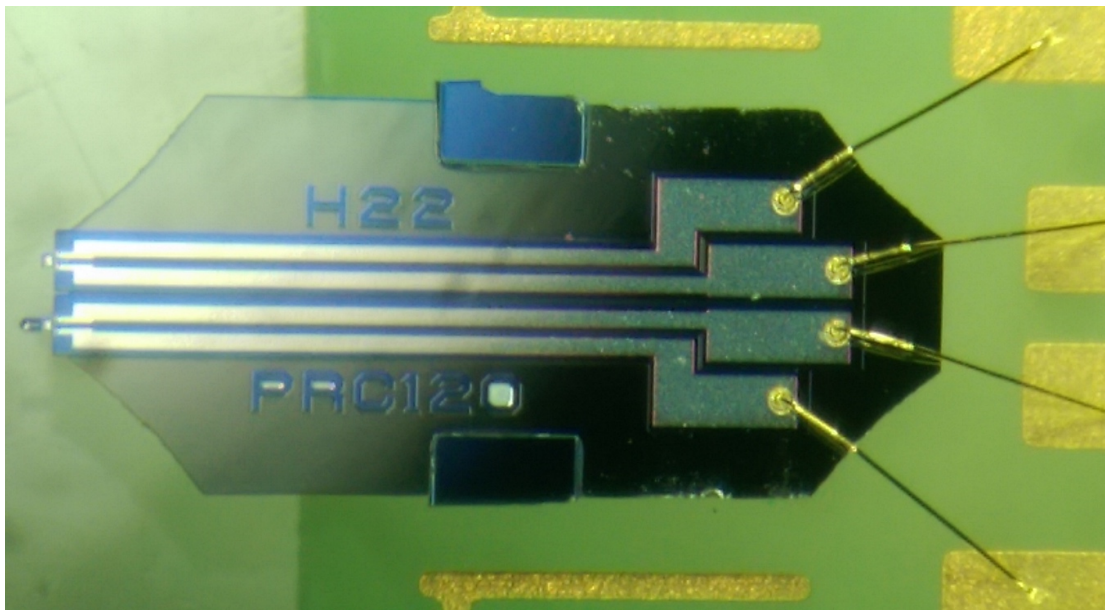


FIGURE 4.10: Commercially available silicon piezoresistive microcantilever fabricated by Seiko Instruments Inc. The sample lever on the far left has dimensions  $l=120 \mu\text{m}, t=4 \mu\text{m}, w=50 \mu\text{m}$ .

sensitivity is determined by the noise of this voltage, which is on the order of tens of  $\mu\text{V}$  in zero magnetic field. During the magnetic field pulse, the sensitivity of the torque signal decreases due to mechanical vibration and inductive/capacitive cross talk in the measurement wires (Section 4.1), which can give a voltage noise of  $\sim 500 \mu\text{V}$ .

To obtain quantitative values for the magnitude of the torque signal, several parameters of the lever are needed, including the longitudinal piezoresistive coefficient of silicon in the  $\langle 110 \rangle$  direction  $\pi_L$ , the leg width  $w$ , and the thickness  $t$  [57]. With an estimated piezoresistive coefficient of  $4.5 \times 10^{-10} \text{ m}^2/\text{N}$  and both a leg width and thickness, of  $\sim 4 \mu\text{m}$ , the measured change in voltage can be converted to torque with units of Newton-meters with the equation

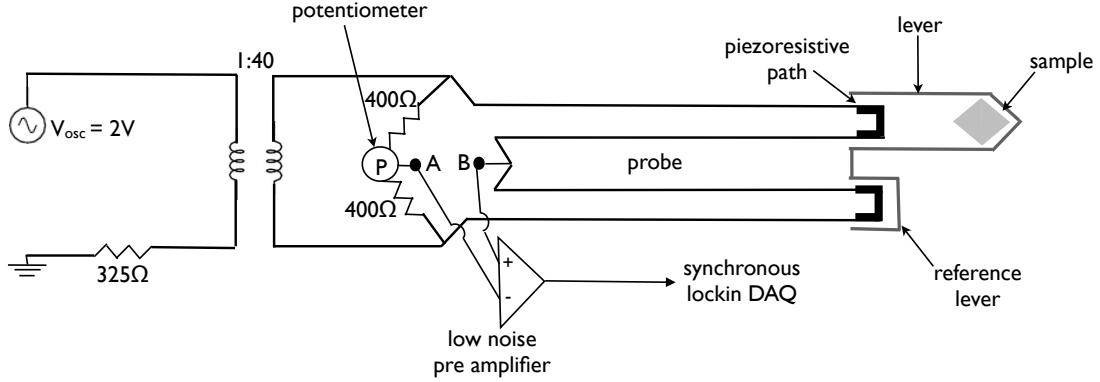


FIGURE 4.11: The Wheatstone bridge circuit diagram for a typical torque magnetometry measurement in the pulsed magnet.

$$\tau = \frac{4wt^2\delta V}{3\pi_L V} = \frac{wt^2\delta R}{3\pi_L R}, \quad (4.4)$$

where  $V$  is the excitation voltage and is roughly 100 mV for a lever resistance path of approximately  $500\Omega$  at low temperature [57]. There is a systematic error in the absolute magnitude of the signal due to variation in the calibration of the piezoresistive response of each lever. For this reason, all torque magnetometry measurements on  $\text{Li}_2\text{IrO}_3$  were performed on the same lever to get an accurate temperature dependence of the magnetic anisotropy. Also, to get an absolute magnitude of the magnetic susceptibility, the measurements were repeated using a SQUID magnetometer (Section 4.3), and close agreement with the magnitude of the torque data is found using the above equation.

### 4.3 SQUID Magnetometry

SQUID magnetometers are made up of two superconductors that form a ring, but are separated by layers of insulating material – Josephson junctions [59]. A change in the magnetic flux through the Josephson junctions due to the sample’s magnetic response will change the phase of Cooper pairs across the junction. The phase difference between the two superconductors affects the electrical properties at the junction and this can be detected as a change in voltage. By maintaining a constant current, the flux will vary between two values depending upon the applied flux quantum, causing the voltage to oscillate [59]. A shift in this oscillation frequency can be measured with extreme accuracy, making the SQUID a sensitive measurement of magnetic field. The SQUID measurements on  $\text{Li}_2\text{IrO}_3$  (Chapter 6) were done by collaborators in the group of James Analytis at UC Berkeley.

### 4.4 Proximity Detector Oscillator (PDO) Measurements

PDO is an *rf* technique that can be used to measure magnetic susceptibility in the case of insulators or changes in the skin-depth in the case of conducting materials. The PDO circuit is based on a proximity detector chip used in modern metal detectors, which operates similarly to a TDO (tunnel diode oscillator) circuit. However, unlike a TDO, the PDO can operate across a wide range of temperatures and inductances, has a broad dynamic resonant frequency range, and is insensitive to bias voltages [60]. PDO is also a contactless technique that can be used to measure conductance, which is especially useful for samples whose surfaces are difficult to contact. Additionally, it is well suited for pulsed magnetic field measurements due to the high speed of data acquisition – signal frequencies on the order of MHz allow changes in the sample response to be measured in microsecond time scales [61].

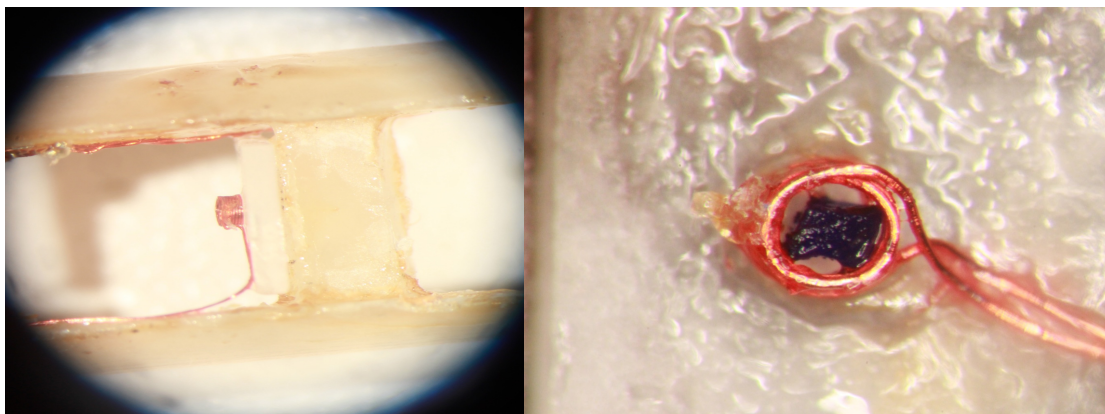


FIGURE 4.12: Left: A photograph of the coil oriented on a probe for magnetic field aligned with the long axis of the coil. Right: A coil tightly wound around  $[\text{Cu}(\text{pyz})(\text{gly})](\text{ClO}_4)$  to increase the filling factor and the inductive coupling.

The sample is inserted into a coil that is part of the PDO circuit (Figure 4.12). The filling factor (sample volume/coil volume) should be between 0.5 and 1 to effectively couple the sample to the coil [60]. Changes in the skin depth (electrical conductivity) or the magnetic susceptibility will change the inductance  $L$  of the circuit, causing a shift in the measured frequency  $\omega$  (more details contained in reference [61]). For insulators, the frequency shift is

$$\Delta\omega = -a\Delta\chi - b\Delta R_o, \quad (4.5)$$

where  $a$  and  $b$  are positive constant functions of the magnetoconductance, capacitance, and inductance of the circuit.  $\Delta R_o$  represents the magnetoconductance of the coax cable and the sensor coil in the presence of a magnetic field [61]. Changes in the magnetic susceptibility  $\Delta\chi$  can be isolated from the magnetoconductance by taking a background measurement without a sample inside of the coil and subtracting this from the sample measurement.

## 4.5 Electron Paramagnetic Resonance (EPR)

The electron paramagnetic resonance (EPR) spectra were measured using a cavity perturbation technique and an MVNA spectrometer manufactured by AB-mm. The sample is placed inside a cylindrical multi-moded cavity with resonant frequencies ranging from  $\sim 10$  GHz to 40 GHz. A fixed resonant frequency of the cavity is maintained while sweeping magnetic field. The magnetic field increases the gap between excitable spin states due to Zeeman splitting ( $\Delta E = g\mu_B B$  in the case of a  $s^z = -1/2$  to  $s^z = +1/2$  transition) and when this energy is equal to that of the photon  $h\nu$ , an allowable transition ( $\Delta S_{\text{total}} = 0$ ,  $\Delta s^z = \pm 1$ ) is observed as an absorption in the EPR line. Magnetic fields up to 17 T were provided by a superconducting magnet. A mono-moded rectangular cavity resonating at  $\sim 70$  GHz is used for angle dependent EPR measurements, where rotation between magnetic field sweeps does not require thermal cycling.

## Torque Data Analysis

The torque magnetometry section in the previous chapter provided a general overview of the technique and a predominantly qualitative discussion. In this chapter, the magnetic torque measurements of  $\text{Li}_2\text{IrO}_3$  are presented, along with a thorough, but general discussion of torque data analysis, particularly in the low field limit. Other factors contributing to the torque signal are discussed, including: the force acting on a magnetic sample due to a magnetic field gradient, the magnetoresistive background due to the piezoresistive path of the lever, and the nonlinear response of the lever.

The magnetic torque of  $\text{Li}_2\text{IrO}_3$  was measured in the 20 T superconducting magnet. At small applied magnetic fields, the linear response of  $\tau/H$  is determined as a function of angle and temperature in the crystallographic  $a$ - $b$ ,  $a$ - $c$ , and  $b$ - $c$  planes, yielding the principal components of magnetic anisotropy<sup>\*</sup>. The magnetic field  $H^*$

---

<sup>\*</sup>Modic, K. A. et al. Realization of a three-dimensional spin–anisotropic harmonic honeycomb iridate. Nat. Commun. 5:4203 doi: 10.1038/ncomms5203 (2014). J.G.A. synthesized the crystals. J.G.A. and R.D.M. conceived the experiment. K.A.M., R.D.M., A.S. and J.G.A. performed the torque magnetometry experiments. N.P.B., J.G.A. and T.E.S. performed the SQUID magnetometry experiments. A.V., I.K. and A.S. contributed to the theory. A.B., S.C., R.D.J. and R.C. solved the crystal structure from single-crystal X-ray diffraction measurements and wrote the crystallography section of the paper. P.W.-C., G.T.M., F.G. and J.Y.C. performed additional X-ray diffraction measurements. Z.I. measured changes in the low-temperature crystallographic parameters below TN. All authors contributed to the writing of the manuscript.

at which a transition, apparently to magnetic saturation, occurs is mapped out as the field is rotated with respect to each crystal plane. The significance of the data shown in this chapter, in regards to understanding the physics of  $\text{Li}_2\text{IrO}_3$ , will be reserved for Chapter 6.

## 5.1 Angle Dependent Torque Data

The deflection of the cantilever in a magnetic field is a direct measure of the magnetic torque of the sample, which can be related to its magnetic anisotropy with the following analysis of the angle dependent torque. Torque magnetometry was measured on the first single crystals of  $\text{Li}_2\text{IrO}_3$ , which were  $\sim 40 \times 30 \times 30 \mu\text{m}^3$ . The primary bending mode of the lever results from a torque that is perpendicular to both the long axis and the normal of the planar surface of the lever. Thus, the orientation of the crystal on the lever and the plane of rotation in field should be chosen in such a way to measure the desired components of magnetic anisotropy,  $\alpha_{ij} \equiv \chi_i - \chi_j$ . For example, in Figure 4.9, a sample with known crystallographic information is oriented on the lever to measure  $\alpha_{bc}$ . The cantilever can be mounted on a rotator probe (Chapter 4) to rotate of the sample with respect to the magnetic field without thermal cycling. The rotational axis is always the torque axis ( $\hat{a}$  in Figure 4.9) and rotation between each measurement is done in  $\sim 5^\circ$  increments. Thermal cycling is only necessary when remounting the sample to change the plane of rotation to measure different principal components of magnetic anisotropy. When remounting, care is taken to maintain the same center of mass position of the crystal on the lever to minimize any systematic changes in the size of the torque signal and the sensitivity.

A single crystal of  $\text{Li}_2\text{IrO}_3$  was oriented on the lever with respect to the applied magnetic field as shown in Figure 5.1. The orientation of the crystallographic axes



FIGURE 5.1: Left: Single crystal of  $\text{Li}_2\text{IrO}_3$  oriented on lever for rotation through a crystal plane which does not contain a principal direction. Right: Orientation of crystallographic axes with respect to the macroscopic crystal and the relative orientation of the applied magnetic field.

with respect to the diamond-shaped morphology of the macroscopic crystal is also shown on the right hand side of Figure 5.1. The raw torque signal measured as a function of magnetic field to 18 T is shown in Figure 5.2.

This measurement was done at 1.5 K, within the magnetically ordered state of  $\text{Li}_2\text{IrO}_3$  (Chapter 6), and with an angle of  $\theta = 45^\circ$  between the crystallographic  $\hat{c}$  axis and the applied magnetic field  $\vec{H}$  (the lever was rotated into the plane of the paper in Figure 5.1). The parabolic shape of the curve below 4 T demonstrates the paramagnetic response where the induced magnetization is linear in field strength. At a magnetic field of approximately 4.3 T for this particular orientation and temperature, the parabolic behavior subsides and the torque signal kinks to a more linear response at higher fields, implying a saturation of the magnetic response. When there is no external field applied, the measured torque should be zero. However, at a finite frequency, the bridge circuit can never be balanced exactly and this causes a finite voltage reading. The offset at zero field has been removed by fitting the data below magnetic fields of 3 T to a quadratic function (Inset

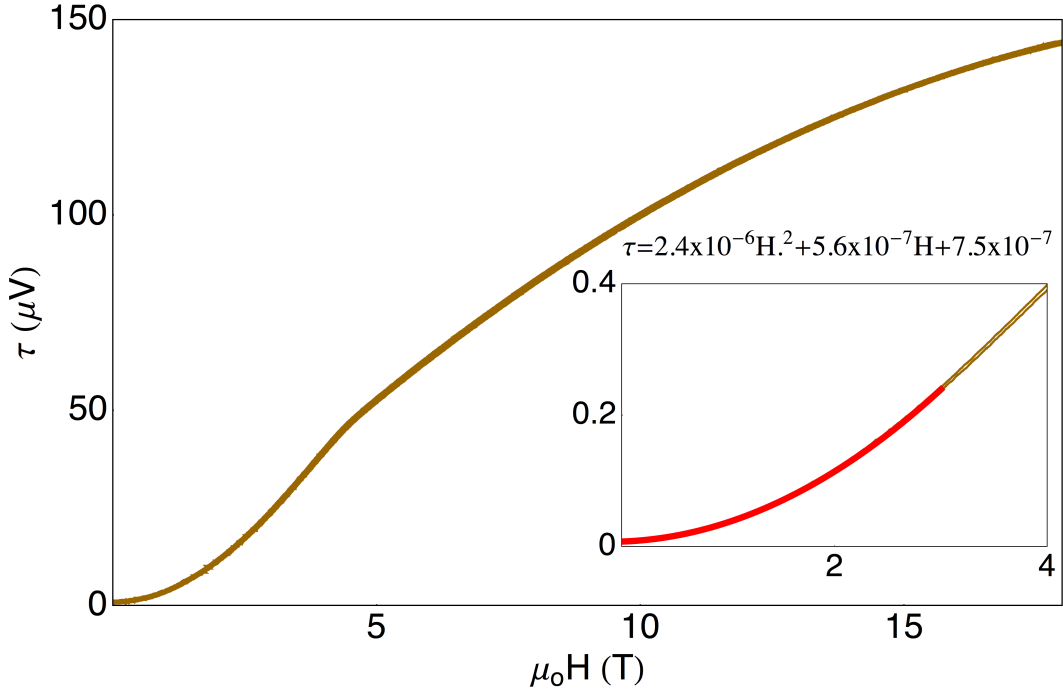


FIGURE 5.2: The raw torque signal of  $\text{Li}_2\text{IrO}_3$  as a function of applied magnetic field measured at  $T=1.5$  K. The magnetic field is applied  $45^\circ$  from the crystallographic  $\hat{c}$  axis toward an angle between the crystallographic  $\hat{a}$  and  $\hat{b}$  axes. The inset shows the measured torque below magnetic fields of 4 T with a parabolic fit to fields below 3 T. The inset highlights a small, but finite offset in the measured torque in the absence of an external field due to an imbalance of the bridge circuit.

of Figure 5.2) and subtracting the y-intercept determined by the fit parameters. This value has been subtracted from all values of the output voltage.

The measurement is repeated for a number of different angles between the crystallographic  $\hat{c}$  axis and the applied magnetic field and the data is shown in Figure 5.3. The offset has been removed and the observed deflection of the lever measured as a voltage has been converted to proper units of torque (Nm) using Equation 4.4. Each of the colored curves correspond to different degrees of rotation through the arbitrary crystal plane shown in Figure 5.1. The red data corresponds to the magnetic field applied parallel to the crystallographic  $\hat{c}$  axis and green data is

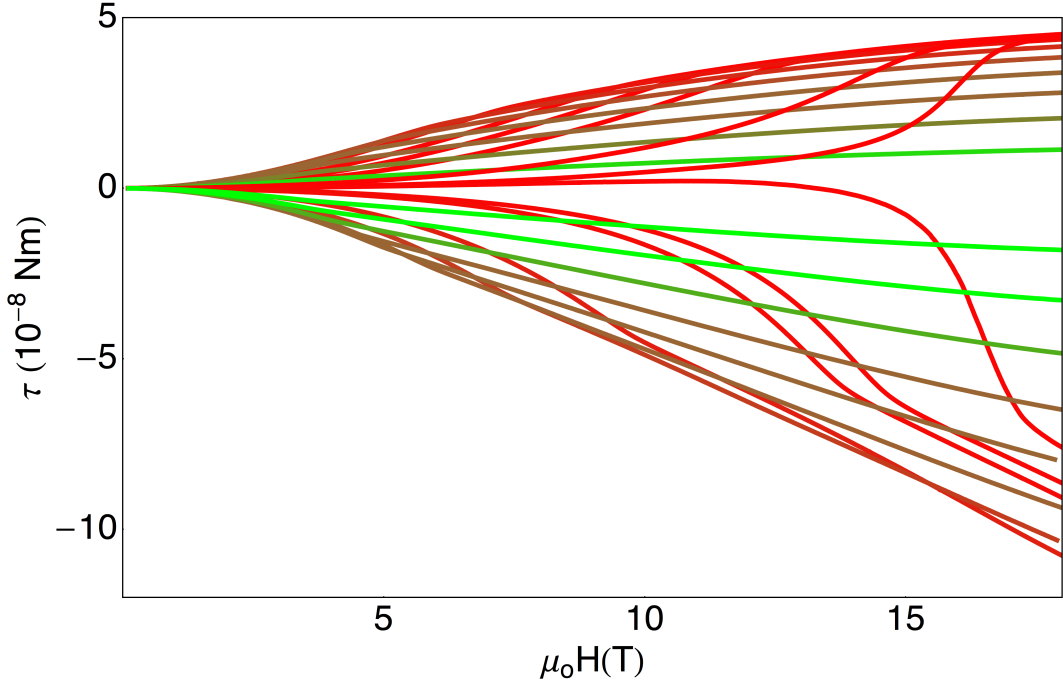


FIGURE 5.3: Raw torque signal of  $\text{Li}_2\text{IrO}_3$  as a function of magnetic field at  $T=1.5$  K. Colored curves correspond to rotation of the crystal with respect to the applied field from the crystallographic  $\hat{c}$  axis through an arbitrary plane of the crystal.

taken when the field is applied in the  $a$ - $b$  plane. Blended colors represent angles in between these two directions. The full data set in Figure 5.3 represents a complete  $180^\circ$  rotation through a single crystal plane. The positive (negative) sign of the torque signal, which changes with magnetic field applied to either side of the  $\hat{c}$  axis, is associated with the lever flexing up (down). The relationship between the sign and the direction of flexing depends on the bridge circuitry and can be verified by carefully flexing the lever under a microscope and recording the sign of the voltage measured.

The measured torque (without a force contribution, which will be discussed shortly) is simply  $\vec{\tau} = \vec{M} \times \vec{H}$  and so a convenient way to represent the magnetization is to

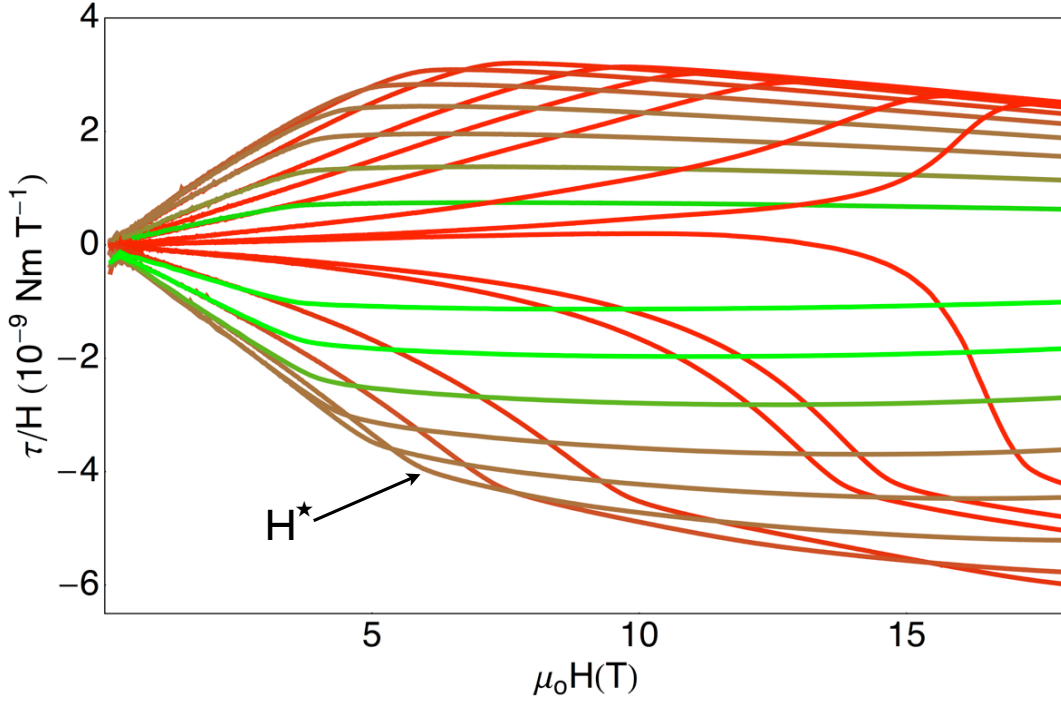


FIGURE 5.4: Torque signal  $\tau$  divided by the applied magnetic field  $H$  at a temperature of 1.5 K, indicating a linear low field dependence which is strongly angle dependent. Colored curves correspond to angles in Figure 5.11.

divide the data in Figure 5.3 by the applied magnetic field (Figure 5.4). At temperatures well within the magnetically ordered phase, just as one would observe in a magnetization measurement, a few features from the  $\tau/H$  data are immediately noticeable. At all angles,  $\tau/H$  increases linearly as function of field until a change in slope occurs at a field denoted as  $H^*$ , and then the magnetic response more or less saturates at higher fields. In the low field limit ( $\vec{M} = \chi\vec{H}$ ), the kink field  $H^*$  is inversely proportional to the magnetic susceptibility. For application of field in or near the  $a$ - $b$  plane, field strengths of only  $\sim 3$ - $5$  T are required to saturate the magnetic response along the field direction. This is true for magnetic field applied at almost all angles, except those very near the  $\hat{c}$  direction. When magnetic field is applied near  $\hat{c}$  (red curves in Figure 5.4), the linear response in  $\tau/H$  is observed

at low fields, but much larger field strengths are required for saturation and this can be accompanied by a large deflection of the lever and a nonlinear response.

The nonlinear behavior that occurs when the field is applied along the “hard” magnetic axis is the result of a feedback mechanism in which the angle-dependent torque changes the angle of the lever. Especially in a system which exhibits large magnetic anisotropy, such as  $\text{Li}_2\text{IrO}_3$ , a small change in the angle of the lever due to the magnetic torque can lead to a large change in the magnetic torque exerted by the sample. This effect is most dramatic when the magnetic field is applied along a direction in which it is energetically unfavorable for an increase in the magnetic susceptibility to occur – essentially competing with a desire to increase susceptibility at nearby angles, altering the angle and the measured torque in a nonlinear fashion.

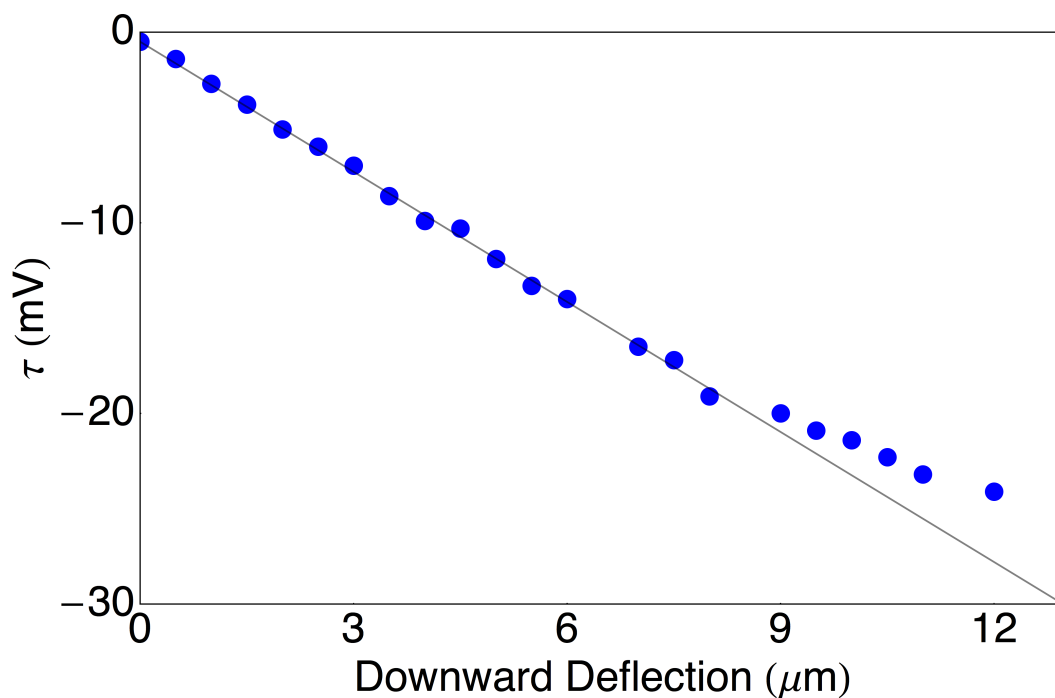


FIGURE 5.5: The Wheatstone bridge circuit diagram for a typical torque magnetometry measurement in the pulsed magnet.

Another nonlinear effect can occur due to the piezoresistive elements of the lever. A simple experimental test was set up to ensure that the measured voltage is a linear response of the torque exerted on the lever when the sample is not attached to it. The change in voltage was measured, while replicating the details of the experimental set-up used in the  $\text{Li}_2\text{IrO}_3$  measurements (Chapter 4), as the lever was flexed incrementally using a micromanipulator under a microscope. The voltage measured as a function of downward deflection of the lever is shown in Figure 5.5. The lever broke after a downward displacement of  $13\ \mu\text{m}$ . The output voltage of the bridge circuit shows a linear response up to a modest deflection of  $9\ \mu\text{m}$ , corresponding to a lever angle of  $\sim 4.3^\circ$ . The size of the torque signal at which the response becomes nonlinear is much larger than the torque exerted by  $\text{Li}_2\text{IrO}_3$  suggesting that we are well within the linear response regime of the lever.

Referring back to the  $\tau/H$  data in Figure 5.4, it is also obvious that the entire data set lies on a background with an overall negative slope. For example, the torque measured with the lever positioned at  $+45^\circ$  and  $-45^\circ$  in Figure 5.3 (brown curves with angle-color relationship labeled in Figure 5.11) should be symmetric about zero. Instead, the lever position ( $-45^\circ$ ) which demonstrates negative torque is of larger magnitude at high fields than its counterpart ( $+45^\circ$ ). This asymmetry can either be explained by a small, yet finite force component from a magnetic field gradient or from magnetoresistance in the lever. The torque signal due to the sample's magnetic properties will change sign according to a  $\sin 2\theta$  dependence (discussion to follow in this section). As the position of the lever with respect to field orientation is rotated  $360^\circ$ , the sign of the torque signal will change upon entering each quadrant, with the same sign observed for quadrants diagonally opposite each other (Figure 5.6). The positive sign corresponds to the lever flexing upwards and negative corresponds to a downward deflection. This is unlike force or magnetoresistive contributions, which either always add to or subtract from the

torque signal irrespective of the angle of the lever. The relative magnitude of the assymetry was studied due to each effect.

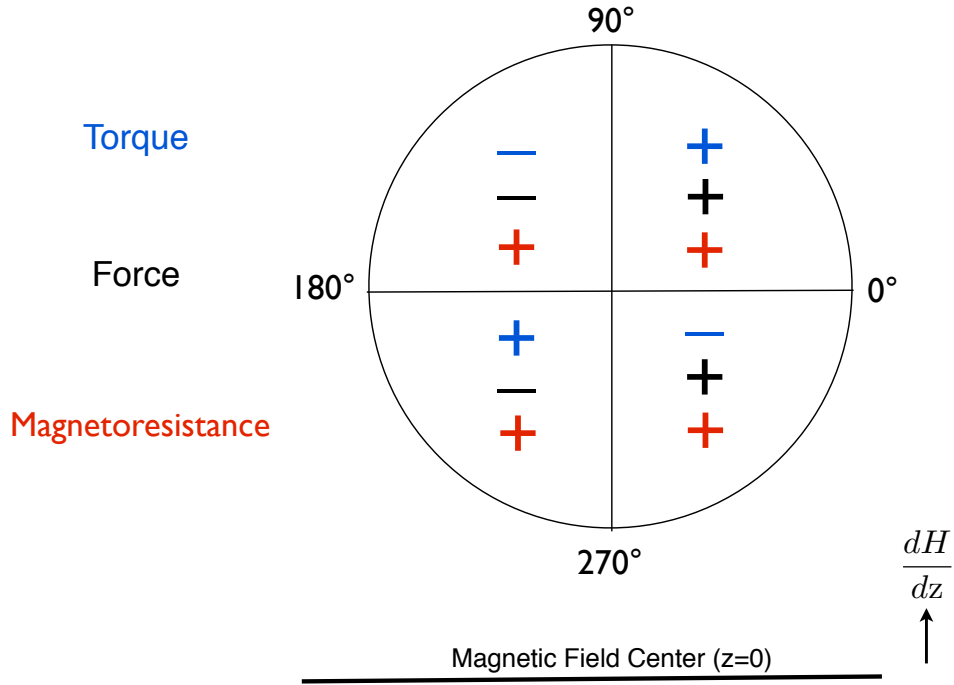


FIGURE 5.6: Schematic of the appropriate sign of the torque, force, and magnetoresistive contributions to the measured signal as the lever is rotated between each quadrant. The example shown is for magnetic field applied in the  $+\hat{z}$  direction with the lever positioned slightly above field center.

The potential energy of a magnetic moment in an applied magnetic field is  $E = -\vec{m} \cdot \vec{H}$ . The force, given by the negative derivative of energy with respect to distance, on a magnetic moment suggests that a non-uniform applied magnetic field in the  $\hat{z}$  direction will also contribute to the measurement signal according to

$$F = m \frac{dH}{dz}. \quad (5.1)$$

The relative magnitude of the force contribution to the signal can be observed by repeating measurements with the cantilever raised or lowered out of field center to determine whether or not the magnetic field gradient is causing a significant source of error. The magnetic torque was measured to 65 T with the probe raised 20 mm above and below field center (Figure 5.7). Upon raising or lowering the probe from field center, a 1.5 percent change in the response was observed at maximum field where the force component is expected to be greatest. It should be noted that this test of the force contribution was done for torque measurements in a plane with larger magnetic anisotropy than those shown in Figure 5.2, which explains the more than an order of magnitude increase in the torque signal. By using the probe centering technique discussed in Section 4.1.3, there is no reason to anticipate that the lever and the sample are more than 5 mm from field center. Hence, it is safe to assume that the force on the lever due to a magnetic field gradient is negligible and is not responsible for the assymetry observed in the angle dependent measurements.

To further explore the cause of the assymetry, which became more apparent at high magnetic fields (Figure 7.4), tests were done in the 65 T pulsed magnet without a sample to determine the effects of magnetoresistance. During pulsed field measurements, only two legs of the Wheatstone bridge circuit are placed in the applied magnetic field; the lever and the reference lever. A two-point measurement of the angle dependent magnetoresistance of both the empty lever and the reference lever was done at 4 K with 125  $\mu\text{A}$ , the typically amount of current used during pulsed field torque measurements. The lever was rotated with respect to the applied field in  $\sim 20^\circ$  increments. An applied magnetic field will cause the resistance to increase with increasing field strengths. Just as expected, this behavior is observed for both levers with a larger (16 percent) change in magnetoresistance for fields applied perpendicular to the lever path ( $0^\circ$ ) as compared to fields applied

parallel to the lever (12 percent).

The question remains as to how this magnetoresistance affects the output voltage measured from the bridge circuit and if its relative magnitude accounts for the asymmetry observed in our measurements. To calculate the output voltage as a function of all resistors making up the bridge circuit, the driving voltage  $V_{\text{in}} = IR_{\text{total}}$  must be determined. With the use of a 40:1 turns ratio  $N$  transformer and load resistor  $R_{\text{Load}} \sim 500 \Omega$ , an effective impedance  $Z = N^2 R_L$  of  $\sim 800 \text{ k}\Omega$  allows a constant current to be assumed. For the particular arrangement of resistors in

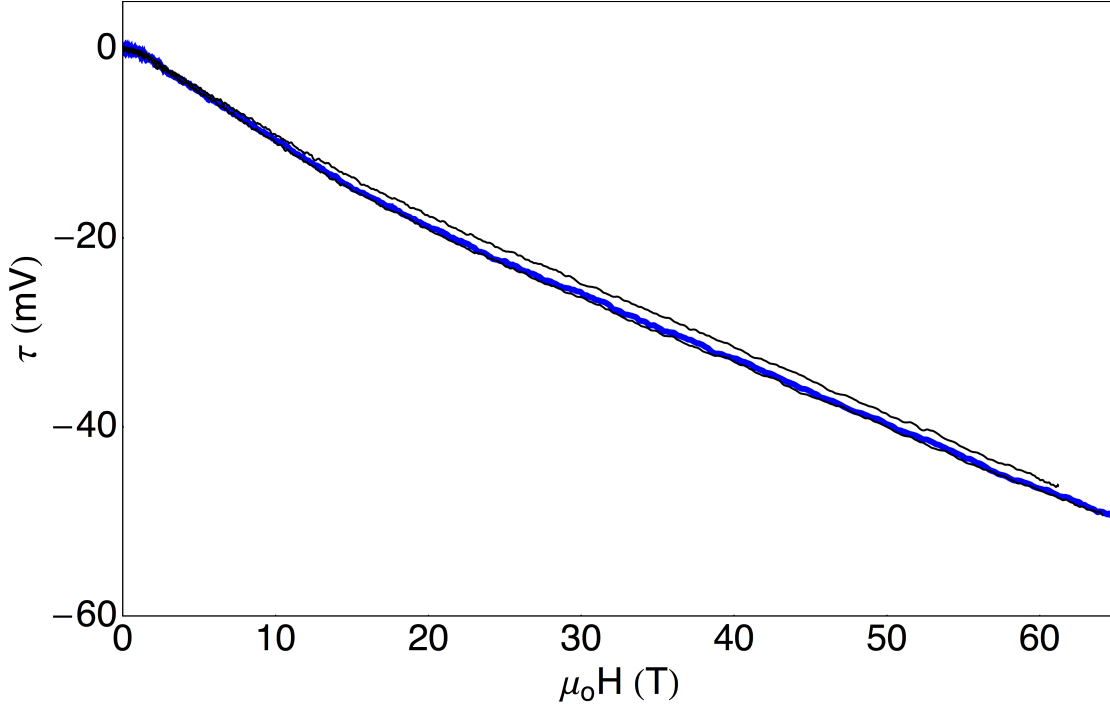


FIGURE 5.7: Torque with magnetic field applied parallel to the crystallographic  $\hat{b}$  direction (thick blue line) at 4 K. Measurements repeated with the probe raised and lowered from field center by 20 mm (thin black lines) showing a 1.5 percent change in torque at 60 T.

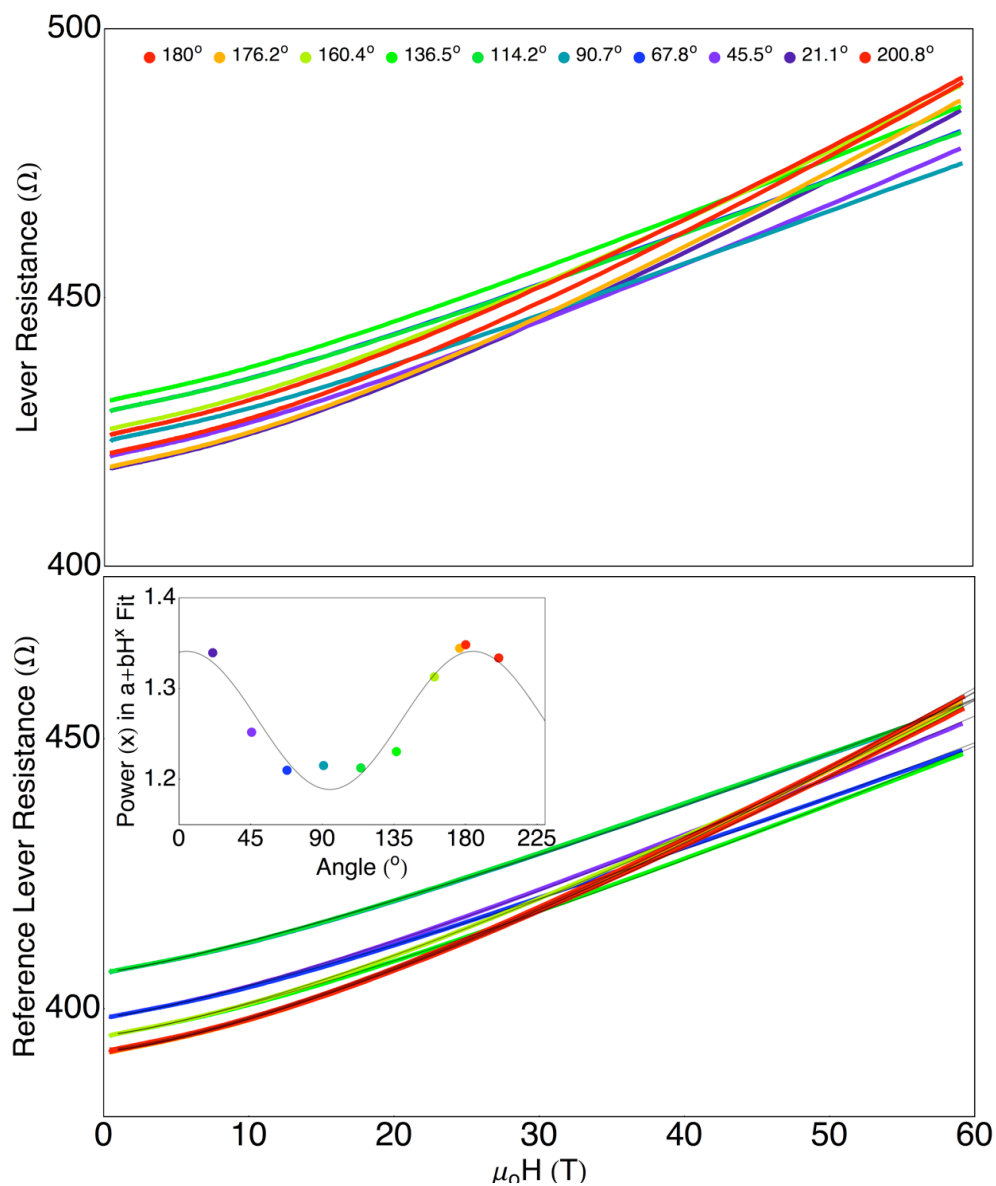


FIGURE 5.8: Angle dependent magnetoresistance of the unloaded lever and the reference lever by a two-point voltage measurement (no bridge circuit) at 4 K. For 60 T magnetic fields applied perpendicular to the lever ( $0^\circ$  or  $180^\circ$ ), a  $\sim 16$  percent change in magnetoresistance is observed, while the lever experiences a  $\sim 12$  percent change in resistance for fields applied parallel ( $90^\circ$ ). Inset: The power  $x$  in the  $a + bH^x$  fit to the magnetoresistance data plotted as a function of angle, which follows a  $\cos^2\theta$  dependence.

Figure 5.9, the total resistance  $R_{\text{total}}$  is given by

$$R_{\text{total}} = \frac{1}{\frac{1}{R_L + R_R} + \frac{1}{R_3 + R_4}} = \frac{(R_3 + R_4)(R_L + R_R)}{R_L + R_R + R_3 + R_4}. \quad (5.2)$$

The potential divider will supply an output voltage  $V_{\text{out}}$  according to the equation

$$V_{\text{out}} = \left( \frac{R_4}{R_3 + R_4} - \frac{R_R}{R_L + R_R} \right) V_{\text{in}}, \quad (5.3)$$

which is given in its final form in Figure 5.9.

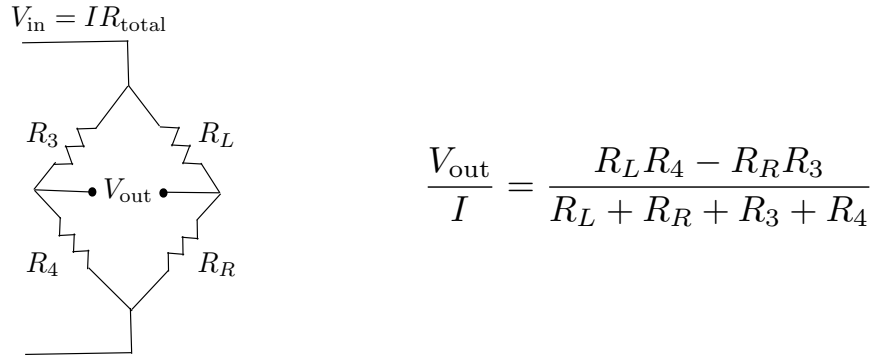


FIGURE 5.9: Schematic of the Wheatstone bridge circuit and the effect of each resistor on the measured output voltage.  $R_L$  is the resistance of the sample lever and  $R_R$  is the resistance of the reference lever

The behavior of the output voltage as a function of magnetic field can be simulated by incorporating magnetoresistance with a  $H^{\frac{1}{3}}$  field dependence on both the sample and reference levers, and torque with an  $H^2$  field dependence on the sample lever. The resistance can be calculated using the right side of Figure 5.9, where  $R_L$  is the resistance of the path to the lever with the sample and  $R_R$  is the resistance of the reference lever path. Both the magnetoresistance and the torque have an angle dependence, which is known from previous measurements. The

torque signal follows a  $\sin 2\theta$  dependence and the magnetoresistance of both levers behave as  $\cos^2\theta$ . After including the angle dependence and choosing reasonable prefactors for each term, the calculated output voltage as a function of magnetic field is shown in Figure 5.10. The torque is simulated as a change in resistance measured from the balanced bridge circuit with the following considerations. Each of the four resistors making up the Wheatstone bridge circuit has a resistance of  $\sim 500 \Omega$  at zero magnetic field and at low temperatures. While measuring  $\text{Li}_2\text{IrO}_3$  in magnetic fields up to 65 T, it is found that the zero field resistance value can change by as much as 10 percent due to the torque on the lever during the pulse. The parameters describing the field and angle dependences were taken from fits to the magnetoresistance data for both the sample and the reference levers. However, the magnitude of the magnetoresistance has been tested without a sample on the lever and thus, there is no torque. Magnetically isotropic materials cannot be used to test this because they do not experience a torque. While it is not definite that the magnetoresistance is fully responsible for the overall negative slope and the asymmetry in the angle dependent measurements, the simulation accurately captures the observed data in the sense that at high magnetic fields, the magnitude of the measured torque for positive angles is approximately half of that measured at negative angles. This observation describes all of the high field torque measurements and so a magnetoresistive background will be subtracted when it is necessary.

A wealth of information about the sample's magnetic anisotropy can be understood from the simple, parabolic response of the torque signal at small fields. It is in this regime that the magnetic response behaves linearly with applied magnetic field and so the magnetic anisotropy can be captured by a susceptibility tensor  $M_i = \chi_{ij}H_j$ . The susceptibility tensor is diagonal in the basis of the principal magnetic axes, which defines three principal components of magnetic susceptibility  $\chi_{a,b,c}$ . For  $\text{Li}_2\text{IrO}_3$ , which is an orthorhombic crystal, these magnetic axes naturally coincide

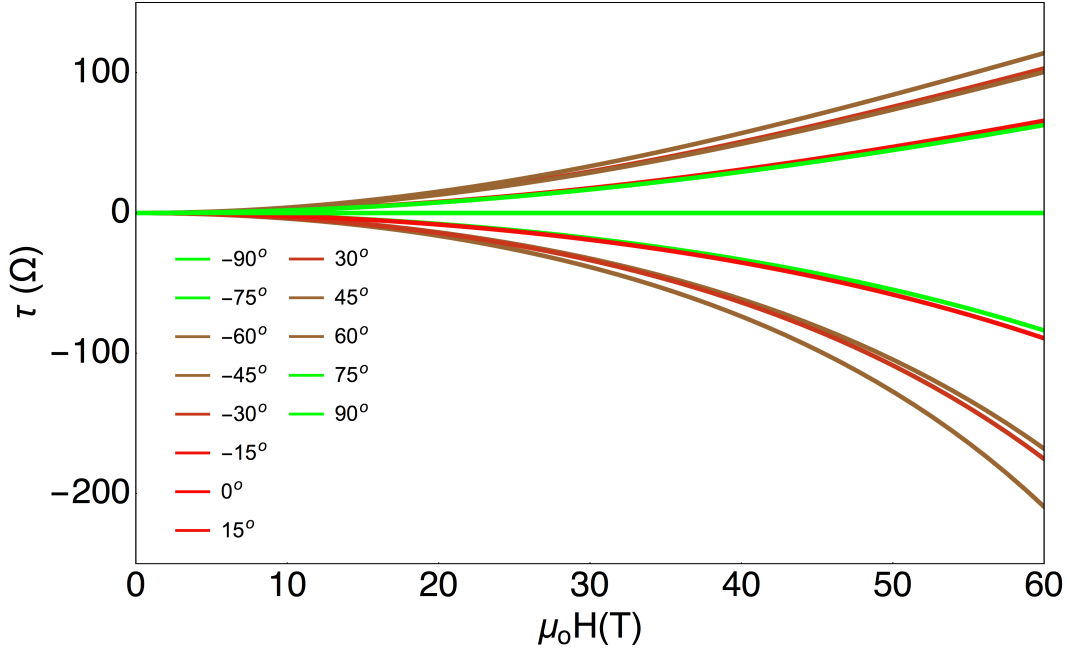


FIGURE 5.10: Simulation of a magnetoresistive background added to a parabolic torque signal.  $0^\circ$  describes the lever perpendicular to the applied magnetic field. The asymmetry of the torque signal as a function of angle is approximately of the same magnitude observed while measuring  $\text{Li}_2\text{IrO}_3$ .

with the crystallographic directions and this can be independently confirmed with torque magnetometry. For example, for rotations in the  $b$ - $c$  plane (Figure 4.9) at small applied fields, the anisotropic magnetization  $(M_b, M_c) = (\chi_b H_b, \chi_c H_c)$  creates a torque

$$\tau_a = M_b H_c - M_c H_b = (\chi_b - \chi_c) H_b H_c. \quad (5.4)$$

Defining  $\theta$  as the angle between a crystallographic axis ( $\hat{c}$  in this case) and the applied magnetic field, the torque can be rewritten as

$$\tau_a = (\chi_b - \chi_c) H^2 \sin\theta \cos\theta = \frac{(\chi_b - \chi_c) H^2 \sin 2\theta}{2}, \quad (5.5)$$

where  $(H_b, H_c) = (H \sin\theta, H \cos\theta)$ . X-ray data on  $\text{Li}_2\text{IrO}_3$  separately identified the

crystallographic axes and so by defining  $\theta$  as the angle between the  $\hat{c}$  direction and the applied magnetic field, it is easy to see that the torque will be zero when the field is applied parallel to the principal magnetic directions ( $\tau \propto \sin 2\theta = 0$  when  $\theta = 0^\circ$  or  $90^\circ$ ). The principal magnetic directions can also be identified from a complete angle dependence of torque measurements even for a sample without known crystallographic information. As only the components of susceptibility perpendicular to the torque axis are measured,  $\theta$  can always be defined from any direction in that plane causing the torque at small fields to pass through zero as the crystal is rotated. To uniquely identify the principal magnetic axes, it may be necessary to do an angle dependence of the torque measurements through several crystal planes to find the true high symmetry direction of the  $\sin 2\theta$  dependence. Importantly, expression 5.5 suggests that the slope of the linear response in  $\tau/H$  versus  $H$  at low fields (Figure 5.4) will have a  $\sin 2\theta$  dependence with the amplitude being proportional to the magnetic anisotropy,  $\alpha_{ij} = (\chi_i - \chi_j)$  (Figure 5.11). Thus, an angle dependence of the magnetic torque is a powerful method to identify the principal magnetic directions and sensitively measure the principal components of magnetic anisotropy.

The slope of the linear response of  $\tau/H$  versus  $H$  (Figure 5.4) is plotted as a function of angle in Figure 5.11. In the paramagnetic regime, when the magnetic field is aligned parallel to a principal magnetic direction, the magnetic moments will grow along that direction, resulting in zero torque. This is observed when magnetic field is applied parallel to the crystallographic  $\hat{c}$  direction ( $\theta = 0^\circ$  in Figure 5.11). The gray line is a  $\sin 2\theta$  fit through the data points to obtain the amplitude and quantify the magnetic anisotropy  $\alpha_{ij}$ .

After determining the principal magnetic axes, the same single crystal was reoriented on the lever to completely map out the principal components of magnetic anisotropy. An angle dependence in the  $a$ - $c$  and  $a$ - $b$  planes were measured in the

20 T superconducting magnet and the  $b$ - $c$  plane was measured in the 65 T pulsed magnet. Using the diamond-shaped morphology (left side of Figure 5.13), the desired components of magnetic susceptibility were oriented in the plane of the long axis of the lever and the planar normal. With magnetic field oriented in the the  $a$ - $c$  plane and at a temperature  $T = 1.5$  K, the magnetic field was swept to 18 T at a rate of 0.5 T/min and data was taken during both the up and down sweep of field with no noticeable hysteresis present.  $\tau/H$  versus  $H$  is shown in Figure 5.12 with the blue (red) color corresponding to the magnetic field applied parallel to the crystallographic  $\hat{a}$  ( $\hat{c}$ ) direction. Blended colors are used for magnetic field applied between the  $\hat{a}$  and  $\hat{c}$  directions as illustrated in the bottom left panel of Figure 5.13. The rotation of the lever between magnetic field sweeps is in  $\sim 5^\circ$

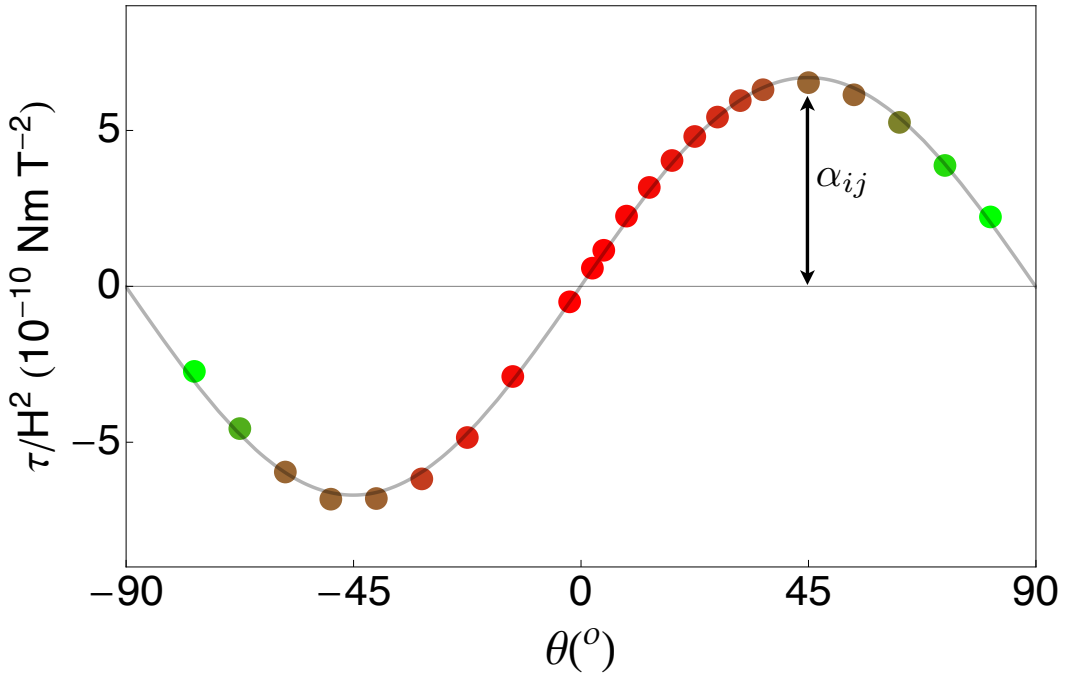


FIGURE 5.11: The slope of the low-field linear response of  $\tau/H$  (Figure 5.4) measured as a function of angle.  $\theta = 0^\circ$  is with field applied parallel to the crystallographic  $\hat{c}$  axis. The crystal is rotated with respect to the external field toward a direction in the  $a$ - $b$  crystal plane.

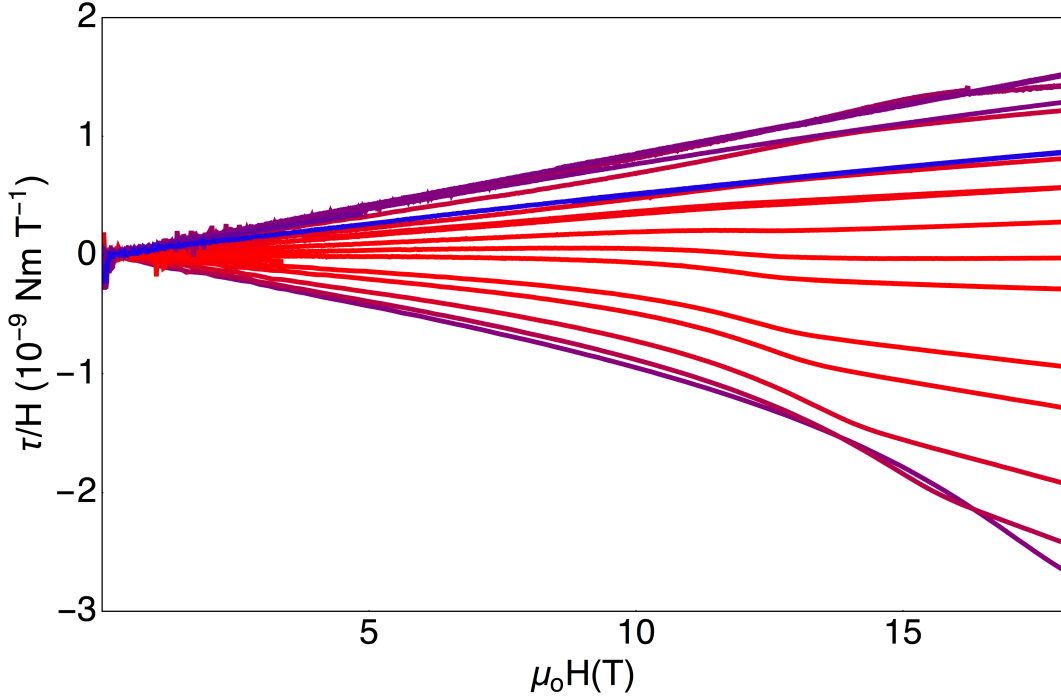


FIGURE 5.12:  $\tau/H$  as a function of magnetic field for rotation of the crystal in the  $a$ - $c$  plane. The colored curves correspond to magnetic field applied parallel to crystallographic directions indicated in Figure 5.13

increments.

The linear response of magnetization is observed with applied magnetic fields below approximately 10 T for all field orientations. A small kink at a particular field  $H^*$  is discernable at most angles. As the lever is rotated so that the field is applied near the  $\hat{a}$  axis ( $\theta > 45^\circ$ ),  $H^*$  moves to high field until it is no longer observable below 18 T.  $H^*$  and the low-field slope are plotted as a function of angle in the right side of Figure 5.13.  $\chi_a - \chi_c$  is given by the amplitude of the  $\sin 2\theta$  fit and is approximately 5 times smaller than the magnetic anisotropy measured between the  $\hat{c}$  direction and the 110 direction roughly (Figure 5.11). The much smaller magnetic anisotropy observed in the  $a$ - $c$  plane suggests that the magnetic susceptibility is largest when there is some component of field along  $\hat{b}$ . This is in

agreement with a kink field  $H^*$  that is pushed to higher fields when there is no component of field along  $\hat{b}$  (top right of Figure 5.13).

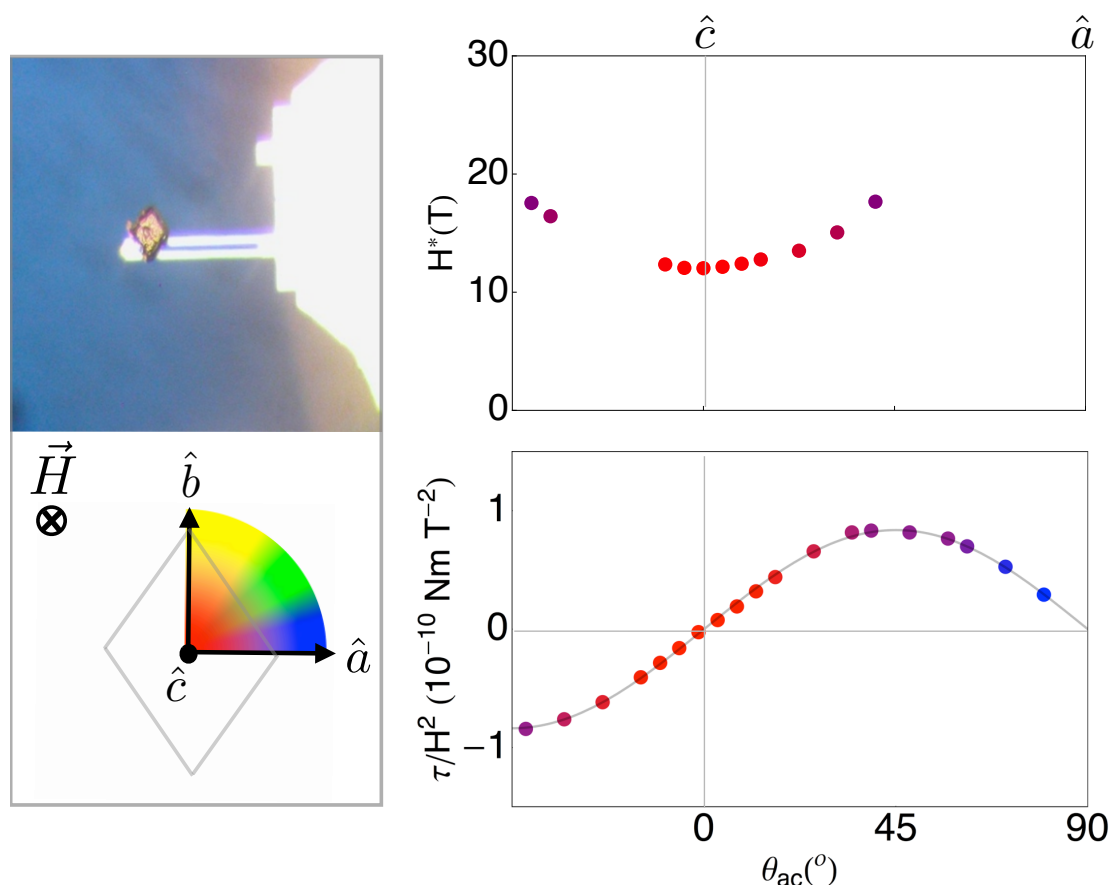


FIGURE 5.13: Left: Crystal orientation on lever for  $a$ - $c$  plane of rotation. Top right: Kink field,  $H^*$  plotted as a function of angle. Bottom right: Angle dependence of low field linear response.

By carefully aligning the sample so that the normal of the diamond face ( $\hat{c}$  axis) is parallel to the torque axis (left side of Figure 5.15), the magnetic anisotropy in the  $a$ - $b$  plane was measured. Similarly, the data is taken at  $T = 1.5$  K.  $\tau/H$  as a function of magnetic field is shown in Figure 5.14 with the blue (yellow) curves corresponding to magnetic field applied along the crystallographic  $\hat{a}$  ( $\hat{b}$ ) directions.

The behavior of the low field slope and the kink field as a function of angle are revealed in Figure 5.15 for field applied in the  $a$ - $b$  plane.

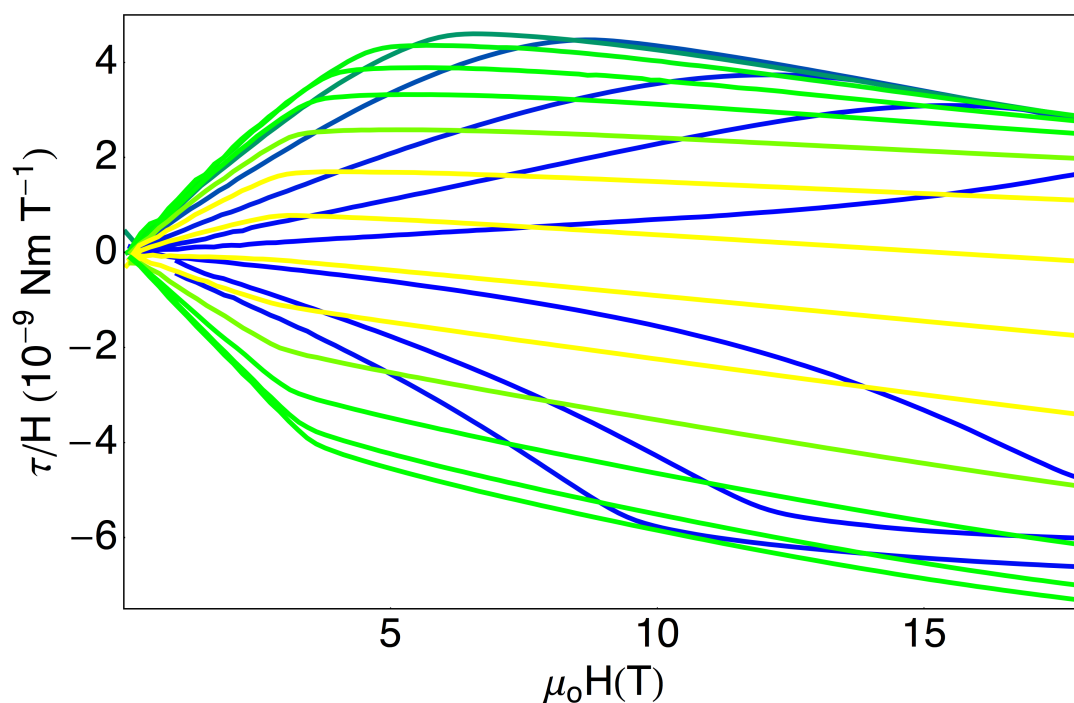


FIGURE 5.14:  $\tau/H$  as a function of magnetic field for rotation of the crystal in the  $a$ - $b$  plane. The colored curves correspond to magnetic field applied parallel to crystallographic directions indicated in Figure 5.15

Some important observations can be made by comparing the measured torque in the  $a$ - $c$  and the  $a$ - $b$  planes. First, by considering only the data in the low field limit (less than 3 T), the size of the torque signal changes by an order of magnitude between the two data sets. This is most easily distinguishable in the  $\tau/H^2$  plot in the bottom right hand panels of Figures 5.13 and 5.15 (notice that the units on the vertical axes are different). This data confirms a much larger magnetic anisotropy in the  $a$ - $b$  plane. Second, there is a much stronger angle dependence of the kink field  $H^*$  when the magnetic field is applied in the  $a$ - $b$  plane. The anisotropy in the

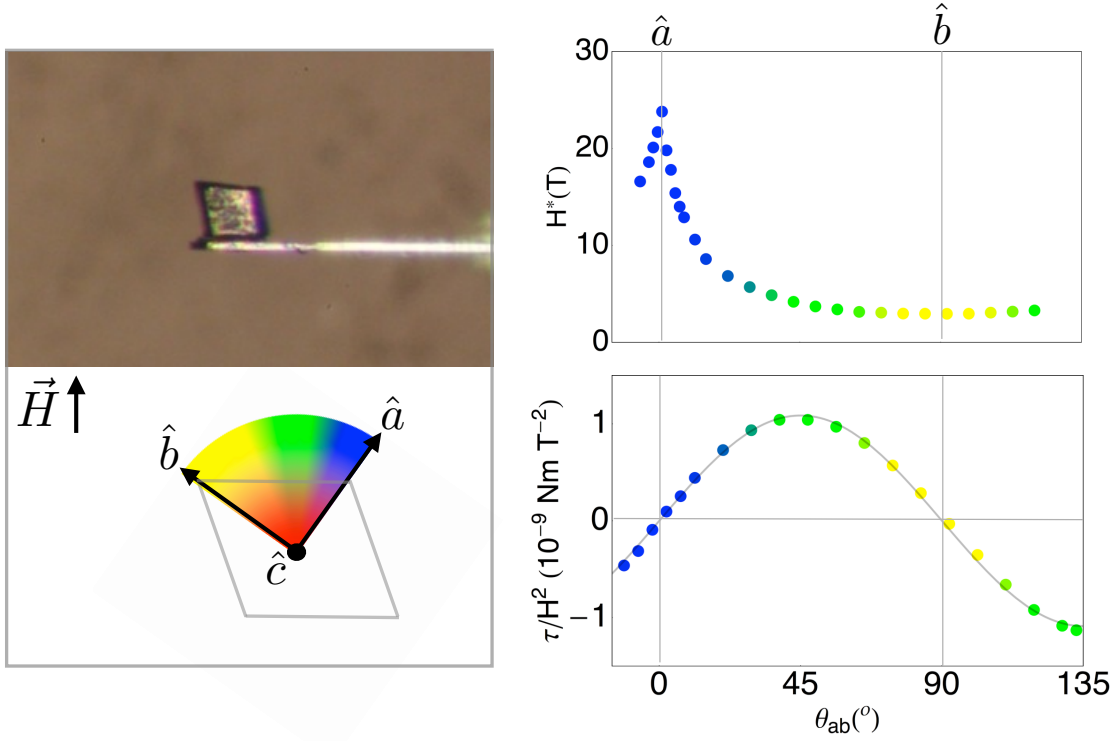


FIGURE 5.15: Left: Crystal orientation on lever for  $a$ - $b$  plane of rotation. Top right: Kink field,  $H^*$  plotted as a function of angle. Bottom right: Angle dependence of low field linear response.

magnetic susceptibility correlates with the anisotropy in the kink field, indicating that there is a common moment at the kink field for all field orientations. However, because only the differences in the magnetic susceptibility are probed, the torque data alone cannot reveal the size of the field-induced moment.

To focus on the temperature dependence of the linear response in the 20 T superconducting magnet, the angle dependent torque in the  $b$ - $c$  plane was only measured to magnetic fields of 5 T. This allowed us to determine the magnetic anisotropy  $\alpha_{bc}$  on the same single crystal as that used to measure the other principal components of magnetic anisotropy. Measuring different samples changes the relative

size of the torque signal, making it difficult to accurately compare the magnetic anisotropy in different crystal planes. The data taken in the  $b$ - $c$  plane is shown in Section 7.2. The 20 T magnet was also used to repeat the angle dependence to 5 T to observe the low field slope of  $\tau/H$  versus  $H$  for all three crystal orientations at several temperatures ranging from 1.5 to 240 K. The significance of how the magnetic anisotropy evolves with temperature is summarized and discussed in Chapter 6. This chapter has presented all of the low field (magnetic fields up to 18 T) torque measurements performed on  $\text{Li}_2\text{IrO}_3$ . The measurements were later extended to higher fields in the pulsed field magnets to map out the angle dependence of the kink field  $H^*$  for fields applied in the  $b$ - $c$  plane and try to saturate the response. The high field torque data (Chapter 7) will be considered in regards to unanswered questions and future work.

## 6

### Magnetic Anisotropy of $\text{Li}_2\text{IrO}_3$

The angle dependent magnetic torque of  $\text{Li}_2\text{IrO}_3$  was measured in applied magnetic fields up to 5 T at a number of temperatures ranging from 1.5 to 240 K to determine the low field slope. As discussed in Chapter 5, the slope as a function of angle follows a  $\sin 2\theta$  dependence with an amplitude that is directly proportional to the magnetic anisotropy. In this chapter, the differences between the principal components of magnetic susceptibility – the magnetic anisotropy – as a function of temperature is shown for each of the principal planes of rotation\*. The significance of the unusual temperature dependence of the magnetic anisotropy of  $\text{Li}_2\text{IrO}_3$  is discussed – starting with the high temperature behavior and then transitioning to the magnetically ordered state at low temperatures. In the context of the Kitaev model, a spin liquid state will manifest itself in the limit of purely anisotropic exchange interactions. The temperature dependence of the magnetic anisotropy from the torque measurements provides compelling evidence for enhanced anisotropy in

---

\*Modic, K. A. et al. Realization of a three-dimensional spin–anisotropic harmonic honeycomb iridate. *Nat. Commun.* 5:4203 doi: 10.1038/ncomms5203 (2014). J.G.A. synthesized the crystals. J.G.A. and R.D.M. conceived the experiment. K.A.M., R.D.M., A.S. and J.G.A. performed the torque magnetometry experiments. N.P.B., J.G.A. and T.E.S. performed the SQUID magnetometry experiments. A.V., I.K. and A.S. contributed to the theory. A.B., S.C., R.D.J. and R.C. solved the crystal structure from single-crystal X-ray diffraction measurements and wrote the crystallography section of the paper. P.W.-C., G.T.M., F.G. and J.Y.C. performed additional X-ray diffraction measurements. Z.I. measured changes in the low-temperature crystallographic parameters below TN. All authors contributed to the writing of the manuscript.

the exchange interactions, but competing interactions prevail, causing the system to order at low temperature. In an effort to engineer a spin liquid, the magnetic anisotropy of  $\text{Li}_2\text{IrO}_3$  must be understood in order to design a material with more extreme anisotropy in the exchange.

In this chapter, the significance of this unusual temperature dependence of the magnetic anisotropy will be discussed in detail. Beginning with the high temperature behavior, the observed magnetic anisotropy can be understood by a uniaxial g-factor anisotropy that is constrained by the crystal structure. Crystallographic x-ray data confirms that there are no changes in the crystallographic symmetry from room temperature to below the ordering temperature  $T_N$  [35]. These observations place constraint on the ordering of the principal components of the g-factor at all temperatures. Upon cooling, the deviation from Curie-Weiss like

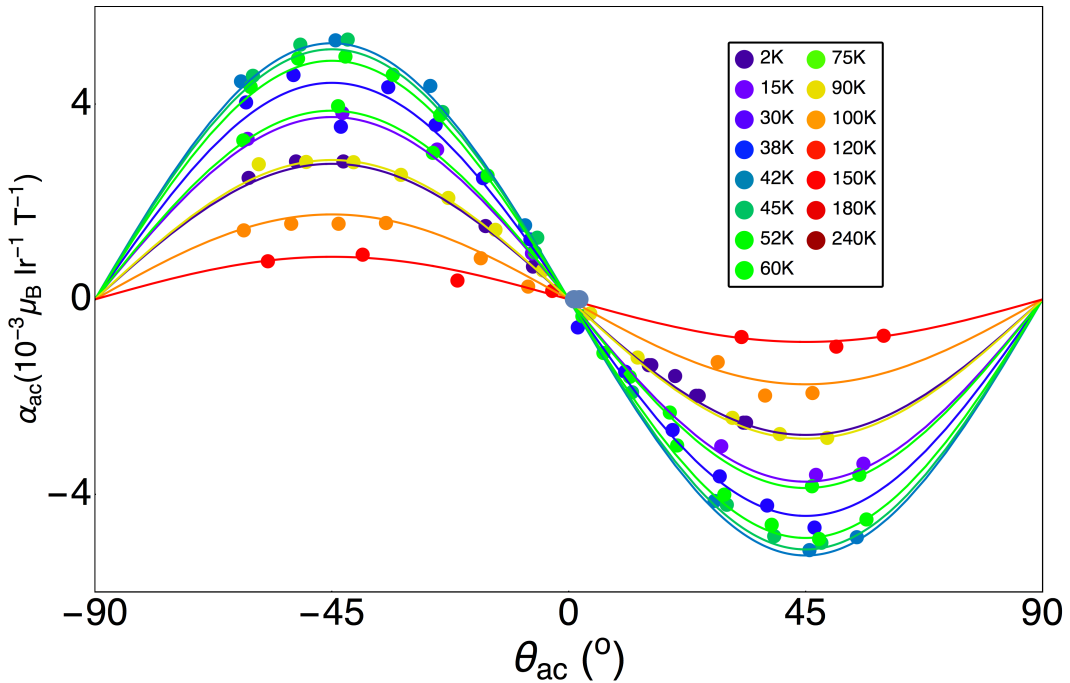


FIGURE 6.1: Slope of the low field linear regime plotted as a function of angle for rotation in the  $a$ - $c$  plane at a number of temperatures ranging from 240 K to 2 K.

behavior is highlighted by the crossover of  $\chi_b$  and  $\chi_c$  at  $T = 75$  K, indicating the energy scale at which the exchange interactions are becoming relevant. The temperature dependence of the magnetic anisotropy suggests that the observed 10-fold increase in  $\chi_b$  at low temperatures must be driven by spin-anisotropy in the exchange interactions.

## 6.1 Temperature Dependent Magnetic Anisotropy

Using the analysis previously discussed in Section 5.1, the magnetic anisotropy  $\alpha_{ij} = \chi_i - \chi_j$  is found for the principal components of magnetic anisotropy  $\alpha_{a,c}$ ,  $\alpha_{a,b}$ , and  $\alpha_{b,c}$  at several temperatures. The slope of  $\tau/H$  at small applied fields, where the magnetization is linear in field strength, is plotted as a function of angle for a number of different temperatures in Figures 6.1, 6.2, and 6.3 for field orientations in the  $a$ - $c$ ,  $a$ - $b$ , and the  $b$ - $c$  planes, respectively.

The angle dependence of the slope is fitted to a sine function to extract the amplitude (equal to  $\frac{\chi_i - \chi_j}{2}$ , see Equation 5.5) and find the magnetic anisotropy  $\chi_i - \chi_j$  at each temperature. The result is plotted in Figure 6.4. The units of the magnetic anisotropy have been converted to  $\mu_B$ /iridium to compare with the absolute magnitude of the magnetic susceptibility measured with SQUID magnetometry (Figure 6.5). The volume of the unit cell, along with the crystal volume estimated by the crystal dimensions were used to approximate the mols of iridium as  $5.95 \times 10^{-9}$ . The Nm units of the torque signal, found using the piezo coefficient of the lever in Equation 4.4, can easily be converted to units of Bohr magnetons. The first thing to notice in comparing the three data sets (Figures 6.1, 6.2, and 6.3) is that rotations that include magnetic field oriented along the  $\hat{b}$  axis have an amplitude that is roughly an order of magnitude greater than the  $a$ - $c$  anisotropy at

low temperatures (compare purple curves in Figures 6.2, and 6.3 to purple curve in Figure 6.1).

Surprisingly, the amplitude of the  $\sin 2\theta$  dependence changes sign as a function of temperature in Figure 6.3. This crossover from a positive to negative amplitude is emphasized in the inset, which is focused on the temperature range 60 K to 100 K. Upon increasing the temperature above 75 K, the torque signal at small applied fields changes sign, suggesting that  $\chi_c$  becomes greater than  $\chi_b$  at high temperature. The resolution of this reordering of the principal components of magnetic susceptibility nicely illustrates the sensitivity and usefulness of the torque magnetometry technique. Because torque directly probes the magnetic anisotropy, a value that is often the main goal of an experiment, it is able to resolve the differences between the principal components of susceptibility even

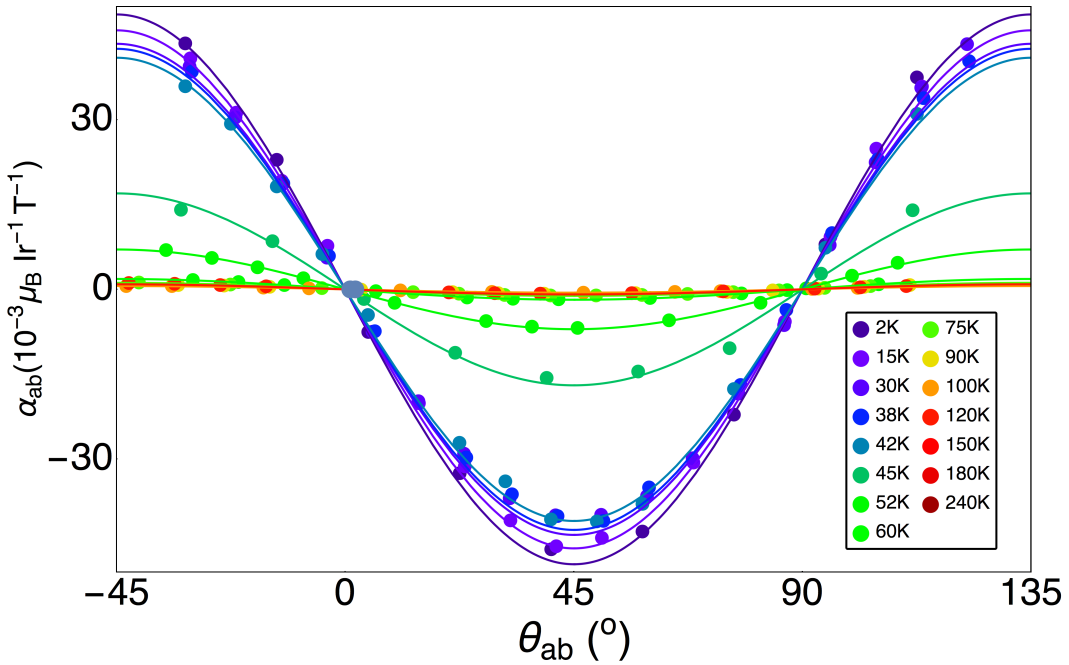


FIGURE 6.2: Slope of the low field linear regime plotted as a function of angle for rotation in the  $a$ - $b$  plane at a number of temperatures ranging from 240 K to 2 K.

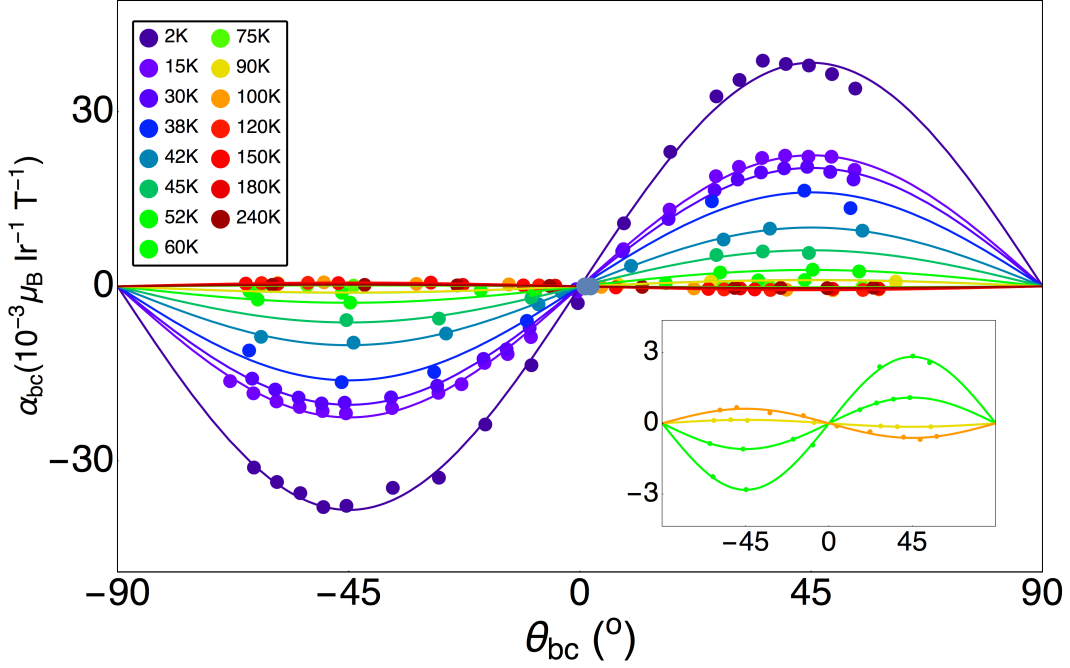


FIGURE 6.3: Slope of the low field linear regime plotted as a function of angle for rotation in the  $b$ - $c$  plane at a number of temperatures ranging from 240 K to 2 K. Inset: Narrowed focus on temperature range where magnetic anisotropy  $\chi_b - \chi_c$  changes sign.

when the individual susceptibilities themselves are large. It would be difficult to accurately determine the anisotropy using conventional magnetometry methods because any misalignment of the crystal will allow undesirable components of the susceptibility to contribute to the signal. Especially for a material with a high degree of magnetic anisotropy, even a very slight misalignment can lead to a large change in the magnetic response. Incidentally, the orientation of the crystal on the lever was left untouched during these measurements with temperature as the only changing variable, which unambiguously confirms the reordering as a function of temperature.

By subtracting the appropriate pairwise differences of the magnetic susceptibility measured with SQUID magnetometry, the light gray data points in Figure 6.4 are

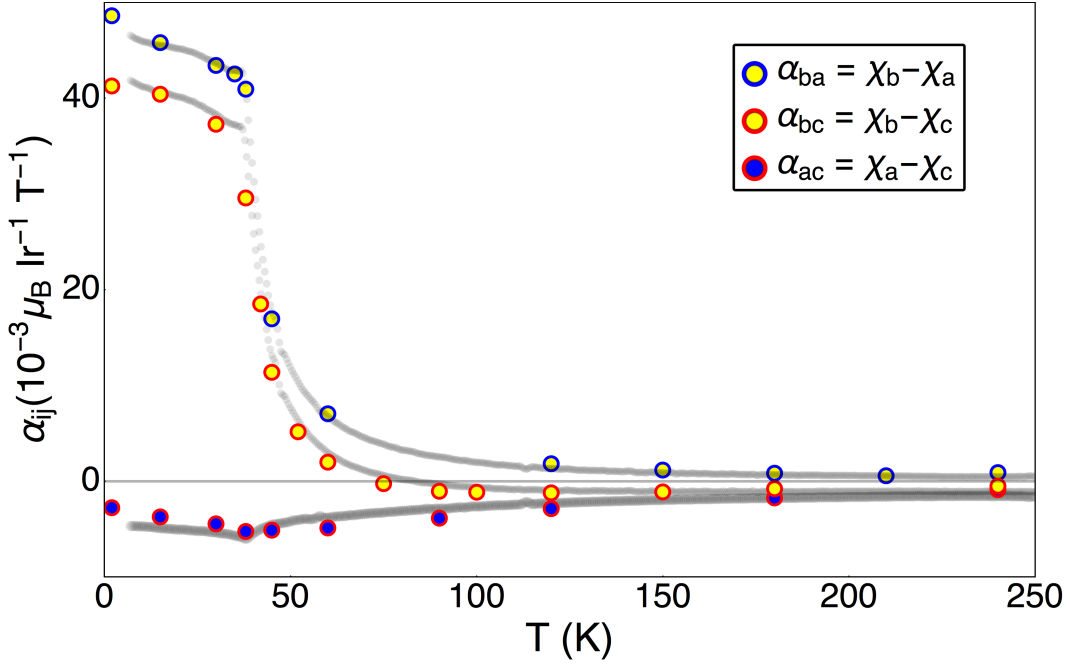


FIGURE 6.4: Temperature dependence of the magnetic anisotropy, as obtained from the amplitude of the  $\sin 2\theta$  dependence in Figures 6.1, 6.2, and 6.3.

obtained. This data is in close agreement with the magnetic anisotropy obtained from torque magnetometry. Because the absolute magnitude of the torque signal relies on the piezoresistive response, which can vary from lever to lever, we used the SQUID data to obtain meaningful absolute values for the susceptibility. We chose to use both techniques in unison as there are some ambiguities that arise in the susceptibility measurements. At high temperatures, the gray lines from the SQUID measurements do not lie on the torque data points. Furthermore, the correct ordering of the principal components at high temperature cannot be captured using the SQUID magnetometer due to a decrease in the sensitivity (this is visibly true in the plot of  $1/\chi$  in Figure 6.10). Also, the smallness of the crystals make it very difficult to accurately align each principal component of susceptibility with the applied magnetic field in the SQUID. To increase the size of the signal and try to minimize the alignment error, these measurements were

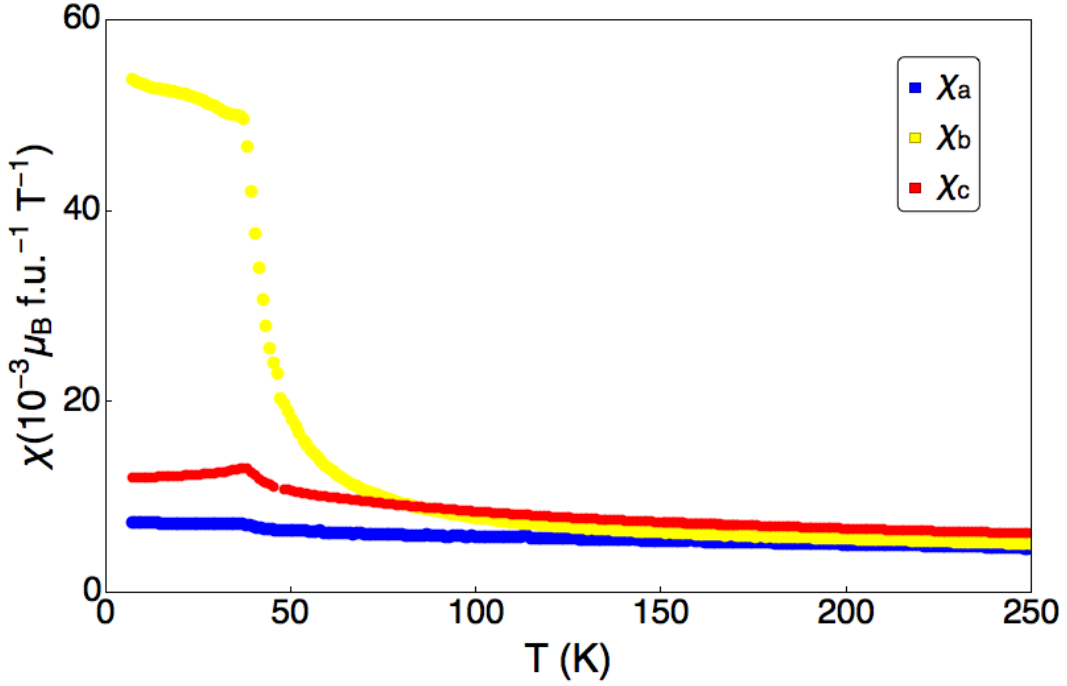
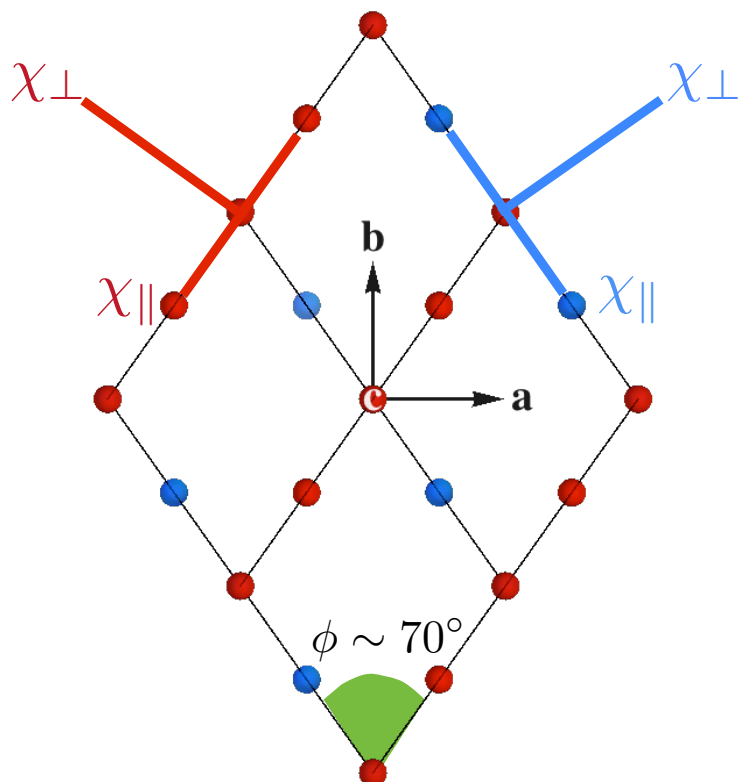


FIGURE 6.5: Temperature dependence of the magnetic susceptibility as measured with SQUID magnetometry using an aligned mosaic of single crystals. Figure modified from [35].

performed for a mosaic of 7 crystals. To account for these inaccuracies, the data points acquired with torque magnetometry in Figure 6.4 were scaled so that the low temperature data for both techniques is in agreement. The vertical axis is then displaying meaningful values for the magnitude of the susceptibility differences. The torque measurements, which can accurately yield the relative magnitude of the principal components of magnetic susceptibility with respect to one another, can then be used to determine the correct value for the differences between the principal components at all temperatures. The rescaled torque data was then used to correct the high temperature magnetic susceptibility to display the proper ordering of the principal components of susceptibility and capture the crossover of  $\chi_b$  and  $\chi_c$  at 75 K in Figure 6.5.

## 6.2 High Temperature Magnetic Anisotropy

Most of the details presented in this section regarding the analysis of the high temperature magnetic anisotropy can also be found in the supplementary information of reference [35]. For an effective spin 1/2 system at temperatures greater than the exchange interaction energy scales, one expects that only  $g$ -factor anisotropy affects the behavior of the magnetic anisotropy. First, one should look to the crystal structure to try to relate the magnetic behavior to the geometrical properties. As recalled from Section 3.2, each iridium atom in the harmonic honeycomb series occupies a local, three-fold planar environment with its nearest neighbor iridium. This is true regardless of the honeycomb plane in which the atom under consideration resides (red versus blue spheres in Figure 3.3). Such an environment implies that each iridium can be described by a uniaxial  $g$ -factor anisotropy that can be captured by a magnetic susceptibility parallel  $\chi_{\parallel}$  to and perpendicular  $\chi_{\perp}$  to the plane defined by its three nearest neighbor iridium atoms. The measured high temperature magnetic anisotropy  $\alpha_{ij} = \chi_i - \chi_j$ , arises from the sum of this local anisotropy of the two interlaced honeycomb planes. At high temperatures, we find that the  $\hat{c}$  component of magnetic susceptibility, which is parallel to both of the honeycomb planes, is larger than  $\chi_{a,b}$ , which both include some component of  $\chi_{\perp}$  (Figure 6.6). Thus, the data reveals that  $\chi_{\parallel} > \chi_{\perp}$ . Strangely, this is opposite to the ordering of the parallel and perpendicular components of the susceptibility  $\chi_{\parallel} < \chi_{\perp}$  observed in the layered  $\text{Na}_2\text{IrO}_3$  compound [49, 63]. It is possible that the larger octahedral distortions within the layers of  $\text{Na}_2\text{IrO}_3$  act in such a way to increase the orbital component of the  $g$ -factor when the magnetic field is applied perpendicular to the layers.




---

FIGURE 6.6:  $c$  axis view of  $\text{Li}_2\text{IrO}_3$  crystal structure showing two honeycomb planes separated by a  $70^\circ$  angle (green arc). The components of magnetic susceptibility  $\chi_{\parallel}$  and  $\chi_{\perp}$  are used to describe the uniaxial  $g$ -factor anisotropy of each plane.

Defining  $\phi$  as the  $70^\circ$  angle separating the two honeycomb planes (Figure 6.6), the components of magnetization along  $\hat{a}$  and  $\hat{b}$  for one of the honeycomb planes is

$$\begin{aligned}
 M_a &= M_{\perp} \cos \frac{\phi}{2} + M_{\parallel} \sin \frac{\phi}{2} \\
 M_b &= M_{\perp} \sin \frac{\phi}{2} - M_{\parallel} \cos \frac{\phi}{2}.
 \end{aligned}
 \tag{6.1}$$

The magnetization parallel  $M_{\parallel}$  and perpendicular  $M_{\perp}$  to that plane can be written as

$$\begin{aligned} M_{\perp} &= \chi_{\perp} H_{\perp} = \chi_{\perp} (H_a \cos \frac{\phi}{2} + H_b \sin \frac{\phi}{2}) \\ M_{\parallel} &= \chi_{\parallel} H_{\parallel} = \chi_{\parallel} (H_a \sin \frac{\phi}{2} - H_b \cos \frac{\phi}{2}). \end{aligned} \quad (6.2)$$

Putting this together, the resulting components of magnetization for one of the honeycomb planes is

$$\begin{aligned} M_a &= \chi_{\parallel} \sin \frac{\phi}{2} [-H_b \cos \frac{\phi}{2} + H_a \sin \frac{\phi}{2}] + \chi_{\perp} \cos \frac{\phi}{2} [H_a \cos \frac{\phi}{2} + H_b \sin \frac{\phi}{2}] \\ M_b &= -\chi_{\parallel} \cos \frac{\phi}{2} [-H_b \cos \frac{\phi}{2} + H_a \sin \frac{\phi}{2}] + \chi_{\perp} \sin \frac{\phi}{2} [H_a \cos \frac{\phi}{2} + H_b \sin \frac{\phi}{2}]. \end{aligned} \quad (6.3)$$

While the other honeycomb plane will similarly take the form

$$\begin{aligned} M_a &= \chi_{\parallel} \sin \frac{\phi}{2} [H_b \cos \frac{\phi}{2} + H_a \sin \frac{\phi}{2}] - \chi_{\perp} \cos \frac{\phi}{2} [-H_a \cos \frac{\phi}{2} + H_b \sin \frac{\phi}{2}] \\ M_b &= \chi_{\parallel} \cos \frac{\phi}{2} [H_b \cos \frac{\phi}{2} + H_a \sin \frac{\phi}{2}] + \chi_{\perp} \sin \frac{\phi}{2} [-H_a \cos \frac{\phi}{2} + H_b \sin \frac{\phi}{2}]. \end{aligned} \quad (6.4)$$

The magnetization components in Equation 6.4 can easily be obtained by changing the sign of the argument in the sine and cosine functions in Equation 6.3. The sum of the local anisotropies of each honeycomb plane give three components of magnetization determined by only two microscopic parameters

$$\begin{aligned} M_a &= 2H_a [\chi_{\perp} \cos^2 \frac{\phi}{2} + \chi_{\parallel} \sin^2 \frac{\phi}{2}] \\ M_b &= 2H_b [\chi_{\perp} \sin^2 \frac{\phi}{2} + \chi_{\parallel} \cos^2 \frac{\phi}{2}] \\ M_c &= H_c \chi_{\parallel}, \end{aligned} \quad (6.5)$$

where the  $\hat{c}$  component of magnetization is purely parallel to both honeycomb

planes. Using  $\chi_{\pm} = \chi_{\parallel} \pm \chi_{\perp}$  and half angle trig identities, the anisotropic susceptibility due to local g-factor anisotropy can be simplified to

$$\begin{aligned}\chi_a &= \chi_+ - \chi_- \cos\phi \\ \chi_b &= \chi_+ + \chi_- \cos\phi \\ \chi_c &= \chi_+ + \chi_-.\end{aligned}\tag{6.6}$$

Again, recall from Section 3.2 that the geometry of the undistorted, edge sharing octahedra constrains the angle separating the two honeycomb planes to  $\phi \sim 70^\circ$ . At high temperature where  $g$ -factor anisotropy dominates, the uniaxial iridium environment combined with the relative orientation of the honeycomb planes, leads to some very simple insights about the magnetic anisotropy. First, from Equation 6.6, the ordering of the three principal components of the magnetic susceptibility must be  $\chi_c > \chi_b > \chi_a$ . Furthermore,  $\cos\phi \sim \frac{1}{3}$  requires that the principal components must be equally spaced  $2\chi_b = \chi_a + \chi_c$  at high temperatures. This equidistant property of the magnetic susceptibilities

$$\begin{aligned}\chi_a &= \chi_+ - \left(\frac{1}{3}\right)\chi_- \\ \chi_b &= \chi_+ + \left(\frac{1}{3}\right)\chi_- \\ \chi_c &= \chi_+ + \chi_-\end{aligned}\tag{6.7}$$

can easily be visualized by considering the radius  $\chi_-$  of a circle, where the angle  $\phi \sim 70^\circ$  represents the relative changes in the principal components of susceptibility from the mean susceptibility  $\chi_+$  (Figure 6.7).

Because torque magnetometry probes the *differences* between the principal components of susceptibility, the simplest way to observe the equal spacing of  $\chi_{a,b,c}$  at high temperatures is to plot the ratios of the differences  $\alpha_{ij}/\alpha_{jk}$ . The equidistant

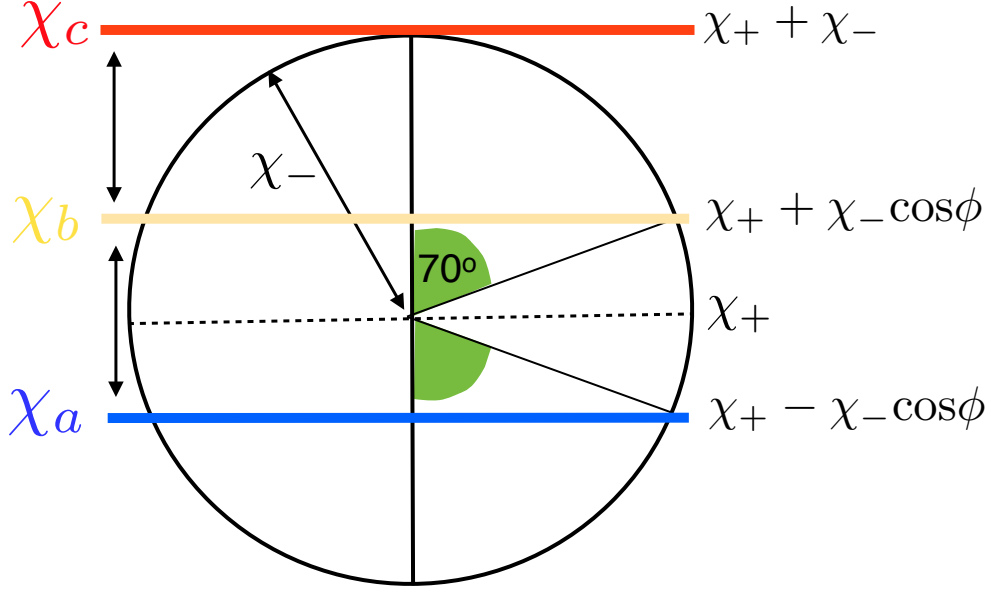


FIGURE 6.7: Schematic of the equidistant susceptibility obtained from a uniaxial  $g$ -factor anisotropy described by components of susceptibility perpendicular and parallel to each plane separated by  $70^\circ$ . The green arc represents the  $70^\circ$  angle between the two honeycomb planes, which is also reflected in the crystal morphology (Figure 6.6).

property is then clearly realized when the ratios of the magnetic anisotropies converge to simple fractional values,  $\alpha_{ba}/\alpha_{ac} = -\frac{1}{2}$ ,  $\alpha_{bc}/\alpha_{ac} = \frac{1}{2}$ ,  $\alpha_{bc}/\alpha_{ab} = 1$  (Figure 6.8). At temperatures below approximately 150 K, the ratios begin to diverge from these values – a good indication that  $g$ -factor anisotropy alone can no longer describe the magnetic anisotropy in this system.

It is conveniently true that all members of the harmonic honeycomb family, except for the layered honeycomb structure, are made up of two planes that are separated by a  $70^\circ$  angle due to the arrangement of their nearly undistorted and edge sharing octahedral complexes. Also, all members have an identical local iridium environment, which suggests that the equidistantly spaced principal components

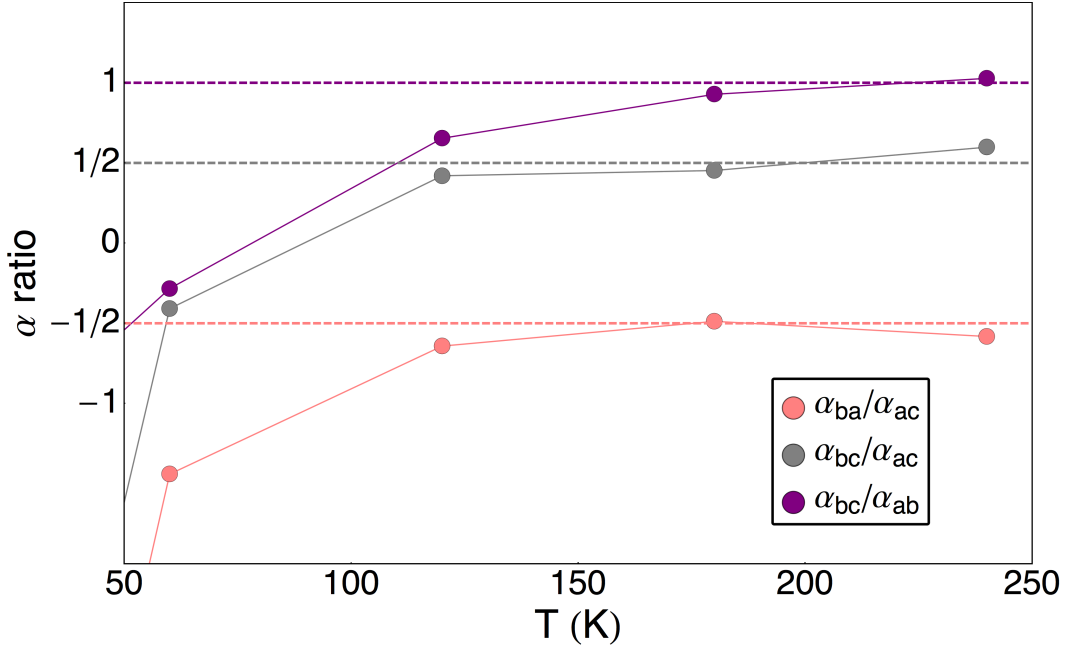


FIGURE 6.8: Ratios of the magnetic anisotropies at high temperatures. The ratios converge to simple fractional values as dictated by the  $g$ -factor anisotropy of the local planar iridium environment. The dashed lines are a guide to the eye.

of susceptibility at high temperature would be a universal feature of this structural family.

Single crystal x-ray diffraction (SXD) data indicates that the structure remains three-dimensionally ordered and fully coherent above and below the magnetic transition temperature (see supplementary information of reference [35]). Also, the observed principal magnetic axes, which were separately verified with torque magnetometry (Chapter 4), are independent of temperature between 300 K and 1.5 K. The observed ordering of the principal components of susceptibility at high temperature, when taken together with the evidence for a temperature-independent crystal structure, places constraints on the ordering of the principal components of the  $g$ -factor at all temperatures.

### 6.3 Deviation from Curie-Weiss Behavior

Torque magnetometry reveals a rather unusual reordering of the principal components of susceptibility as a function of temperature ( $\chi_b - \chi_c$  crosses zero in Figure 6.4). This sign change in the anisotropy was confirmed by repeating an angle dependence of the torque measurements (magnetic field applied at several different angles in the crystallographic  $b$ - $c$  plane) at several temperatures without changing the orientation of the crystal on the lever (Figure 6.9). The amplitude of the  $\sin 2\theta$  angle dependence of the low field slope changes sign between  $T = 75$  K and  $T = 90$  K, corresponding to a change in the direction that the lever flexes in the applied magnetic field – up versus down. This sign change is consistent with  $\chi_b$  becoming greater than  $\chi_c$  at low temperatures.

The susceptibility of a three-dimensional Heisenberg spin will not have a preeminently preferred direction, even if the exchange interactions are stronger along certain directions at low temperatures. Spatial anisotropy of Heisenberg exchange leads to a suppression of long-range magnetic order, by effectively reducing the dimensionality, but  $\chi$  typically does not show a large degree of anisotropy. The crossover of  $\chi_b$  and  $\chi_c$  highlights a strong deviation from Curie-Weiss behavior at much higher temperatures than the ordering temperature  $T_N$ , and this is accompanied by a hugely anisotropic  $\chi$  at low temperatures. Such behavior is in stark contrast to spin-isotropic Heisenberg exchange systems where the low temperature susceptibility reflects the  $g$ -factor anisotropy observed at high temperatures, even in the presence of spatially-anisotropic exchange [35]. For example, in organic Cu-based quasi-two-dimensional Heisenberg magnets, the intra-plane coupling can be as much as three orders of magnitude more than the inter-plane coupling [64]. However, the experimentally determined intra- and inter-plane  $g$ -factors are found to scale with the inverse of their corresponding anisotropic magnetic saturation

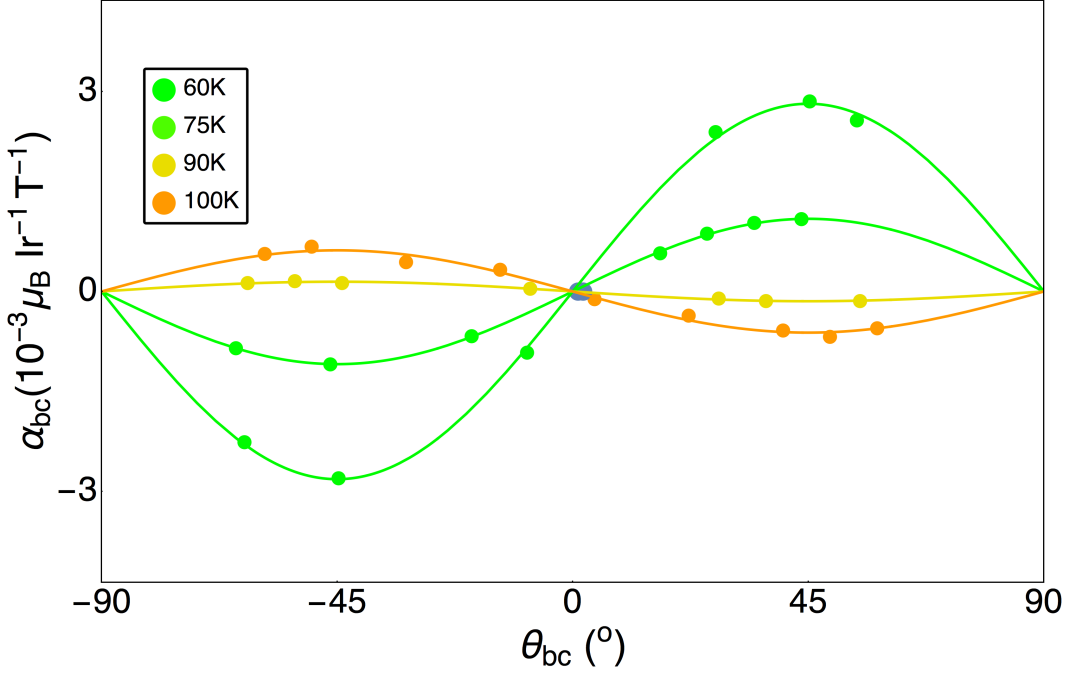


FIGURE 6.9: The data points represent the low field slope of torque measured at several different temperatures and magnetic field orientations in the  $\mathbf{b}$ - $\mathbf{c}$  plane. Similar to the complete temperature dependence shown in Figure 6.3, the lines show a  $\sin 2\theta$  fit to the data confirming that  $\alpha_{bc} = \chi_b - \chi_c$  changes sign between 75 and 90 K.

fields (proportional to the magnetic susceptibilities). In  $\text{Li}_2\text{IrO}_3$ , the crossover arises because  $\chi_b$  softens, becoming an order of magnitude greater than  $\chi_a$  and  $\sim 5$  times greater than  $\chi_c$  (Figure 6.5) at low temperature [35]. As a result, the susceptibility cannot be parameterized by a Curie-Weiss temperature: the linear extrapolation of all three components of inverse susceptibility to the temperature axis depends strongly upon the temperature range considered (Figure 6.10) [35]. For example, between  $T = 50$  K and  $T = 150$  K, all three components of inverse susceptibility extrapolate to a negative temperature, consistent with the absence of a net moment in the ordered state [35]. However, at higher temperatures ( $\sim 200$ – $300$  K) the inverse susceptibilities  $1/\chi_b, 1/\chi_c$  extrapolate to positive temperature intercepts indicating a ferromagnetic component to the interactions.

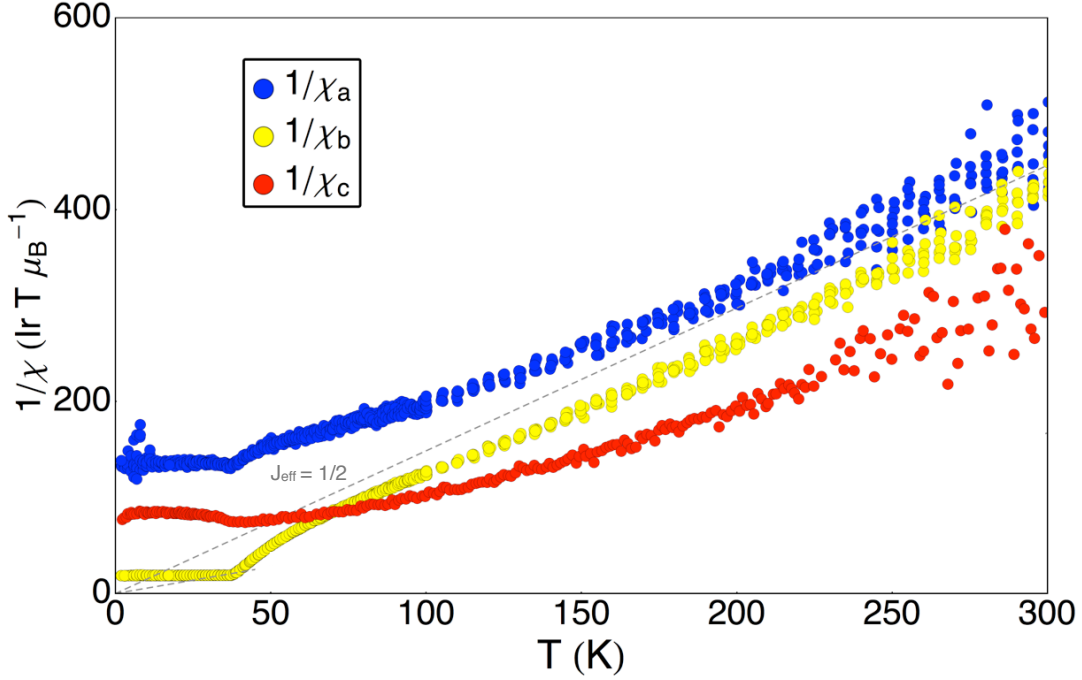


FIGURE 6.10: The inverse of the principal components of susceptibility as a function of temperature. The sensitivity of the SQUID decreases at high temperature making it difficult to determine the Curie-Weiss temperature and the effective moment from a linear fit of  $1/\chi$ . The slope of the dashed line represents the slope expected for  $J_{\text{eff}} = \frac{1}{2}$  magnetism. Figure modified from [35].

Because the linear fit of  $1/\chi$  is so temperature and field angle dependent, the effective magnetic moment per iridium cannot be accurately determined from the susceptibility data. Instead, the dashed line in Figure 6.10 represents the Curie-Weiss behavior for  $J_{\text{eff}} = \frac{1}{2}$  magnetism, where the slope is inversely proportional to and determined by the Curie constant

$$C = \frac{N}{3k_B} \mu_{\text{eff}}^2. \quad (6.8)$$

The effective moment is given by  $\mu_{\text{eff}} = g_J \mu_B \sqrt{J(J+1)}$ , where  $J$  is the total

angular momentum,  $\mu_B$  is the bohr magneton, and  $k_B$  is the boltzmann constant.  $N$  is the total number of magnetic moments per unit volume.  $N$  is set equal to 1 for direct comparison to the observed susceptibility data, which has been renormalized to display susceptibility per iridium. Because the high symmetry of the octahedral complexes at least partially quenches the orbital angular momentum, the total angular momentum  $J$  is estimated to be equal to half the number of unpaired electrons and the  $g$ -factor  $g_J$  is approximately equal to 2 to show the spin-only contribution of spin  $\frac{1}{2}$  per iridium (dashed line).

To date, no experimental evidence has conclusively identified the spin state on iridium in Li<sub>2</sub>IrO<sub>3</sub>. This could be determined by magnetization measurements. However, the unavailability of large single crystals, combined with the need for magnetic fields on the order of 100 T to saturate the magnetic response, makes this a challenging measurement. Attempts were made to observe transitions between the spin states of Li<sub>2</sub>IrO<sub>3</sub> using electron paramagnetic resonance (EPR), but with no sign of a resonance to measured magnetic fields of 16 T and with temperatures up to 250 K. Since the possibility of Li deficiency, leading to a  $5d^4$  electron configuration on iridium, cannot be ruled out, it is shown in Appendix A that the likely ground state for such a scenario is a magnetically active  $\Gamma_4$  triplet.

## 6.4 Low Temperature Magnetic Properties

As the temperature is lowered, the magnetic torque and the susceptibility (Figures 6.4 and 6.5) identify a magnetic anomaly at 38 K. This transition to a magnetically ordered state is most likely reflective of the bipartite nature of the structure (Chapter 3), which alleviates the magnetic frustration [35]. The extreme softening of  $\chi_b$  is truncated by the magnetic instability at 38 K. Within the ordered state, the  $\hat{b}$  component of magnetization increases linearly with applied field ( $\tau/H$  in

Figure 6.11). At a sufficiently high magnetic field,  $H^* \approx 3$  T (Figure 6.11), the magnetization kinks abruptly. For this orientation, the lever was at a  $-45^\circ$  angle when the magnetic field was applied along the  $\hat{b}$  direction, generating a torque  $\tau(-45^\circ) = +\tau + \text{MR}$ . The size of the magnetoresistive background can be determined by subtracting the torque  $\tau(45^\circ) = -\tau + \text{MR}$  from the complementary angle. The dashed line shows the negative slope mostly due to a magnetoresistive background (MR). The magnetoresistive contribution to the signal has been removed from the data in the inset of Figure 6.11. This kink in the magnetization ( $\tau/H$ ) at 3 T corresponds to an induced moment of  $\sim 0.03 \mu_B$  per iridium, as obtained from SQUID magnetometry measurements.

If this kink corresponds to a fully saturated moment along the field direction, the expected magnetic moment is a quantization of the angular momentum along the applied magnetic field direction  $\mu_{\text{eff}} = m g_J \mu_B$ . Here,  $m$  is the magnetic quantum number and can take values from  $-J$  to  $+J$ . For  $J_{\text{eff}} = \frac{1}{2}$  and a  $g$ -factor of 2, this results in an effective magnetic moment approximately equal to  $1 \mu_B$ . Because only a fraction of the expected saturated moment for spin  $\frac{1}{2}$  on iridium is observed, the kink field is associated with a saturation of only the  $\hat{b}$  component of magnetization (see magnetic order in Figure 6.12). The smaller susceptibilities observed for small magnetic fields applied along the  $\hat{a}$  and  $\hat{c}$  directions implies that more field is required to saturate these components of the magnetization, which is perhaps a result of stronger magnetic correlations along the  $\hat{a}$  and  $\hat{c}$  directions.

Our conclusions regarding the magnetic order were later confirmed by magnetic resonant x-ray diffraction [33]. The unexpectedly complex, yet highly symmetric magnetic order below  $T_N$  was found to involve non-coplanar and counter-rotating magnetic moments (Figure 6.12) [33]. The light and dark shaded discs represent elliptical areas in which the moments are confined, with the smallest component of the ellipsoids along  $\hat{b}$ , which helps to justify the projection onto the  $a$ - $c$  plane.

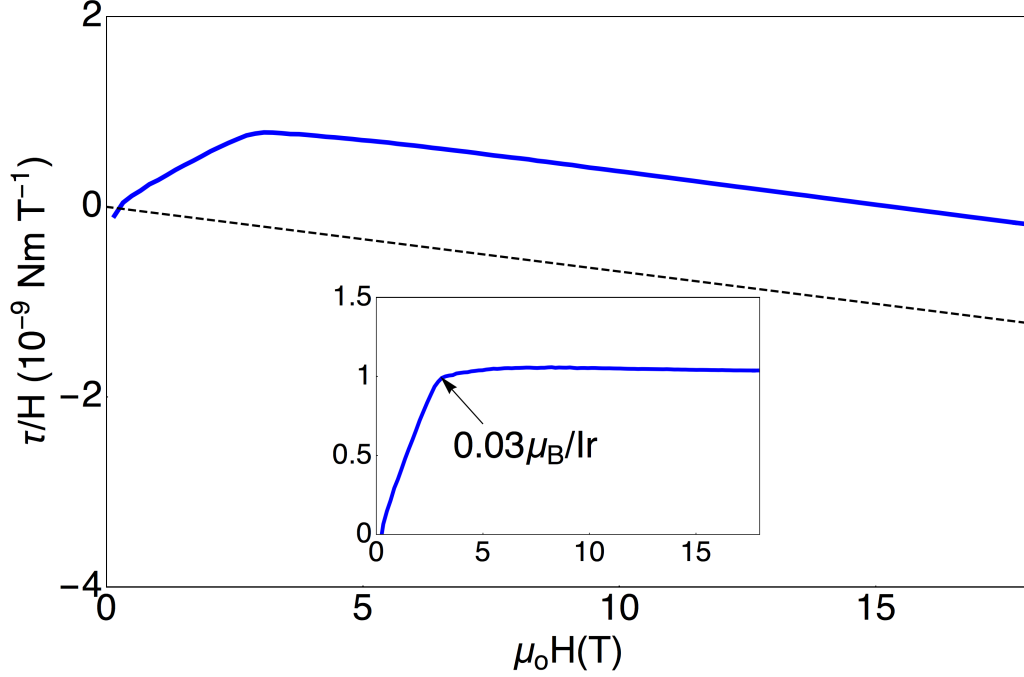


FIGURE 6.11:  $\tau/H$  as a function of magnetic field applied parallel to the  $\hat{b}$  axis at  $T = 1.5$  K. The dashed line shows the overall negative slope caused by magneto-resistance of the lever path. The inset shows the magneto-resistive background subtracted from the data with a moment at the kink field corresponding to  $0.03 \mu_B$  per iridium as obtained from SQUID magnetometry measurements.

Figure 6.12 describes counter-rotating moments between consecutive sites along  $\hat{c}$ , which form counter-rotating zigzag chains along  $\hat{a}$ . By rotating to the “Kitaev” axes ( $\hat{x}$ ,  $\hat{y}$ , and  $\hat{z}$ ), it is clear that along each x-type bond, the spins are aligned when they point along  $\hat{x}$  and anti-aligned when they point along  $\hat{y}$ , and this is similarly true for the y-type bonds, suggesting that Kitaev interactions can stabilize this counter-rotating order with a propagation vector  $\mathbf{q}$  along  $\hat{a}$  [33].

The angular dependence of both the slope of the linear regime and the kink field  $H^*$  was performed for all principal components of anisotropy at  $T = 1.5$  K (Chapter 4). Figure 6.13 shows the low field slope (top right) and the kink field (bottom right)

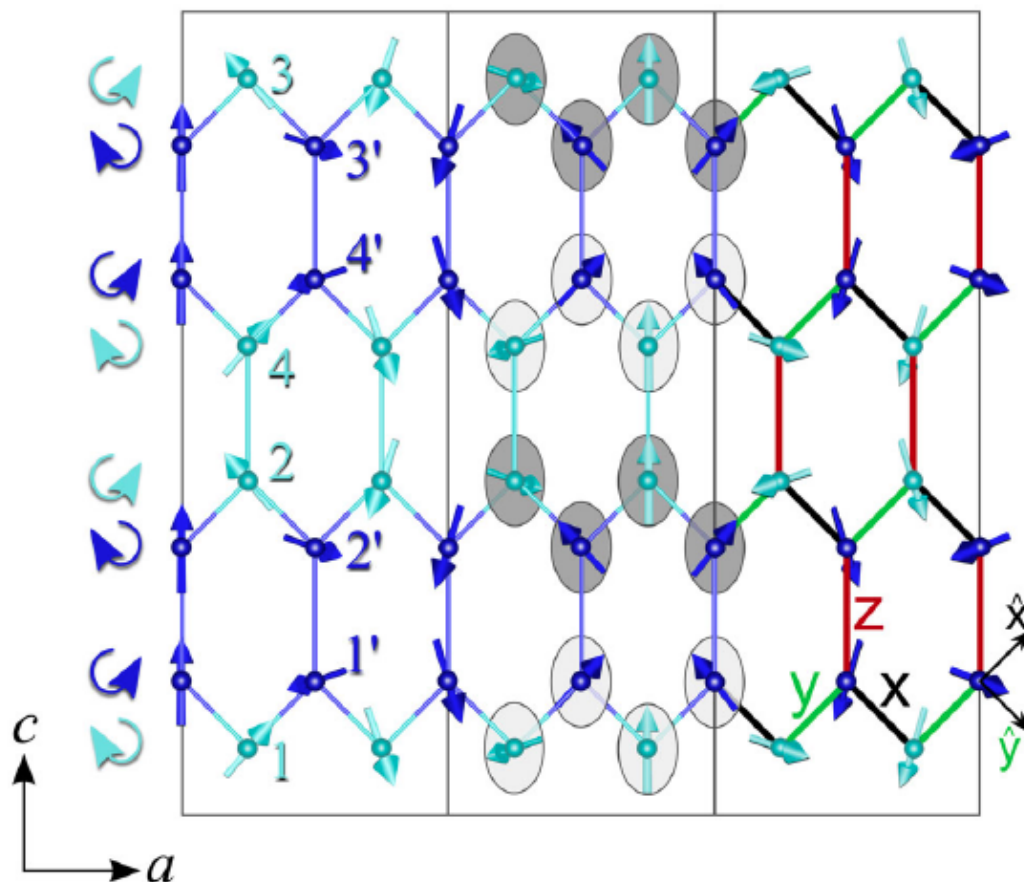


FIGURE 6.12: Projection of the magnetic structure on the  $a$ - $c$  plane showing 3 unit cells along the horizontal propagation direction  $a$ . Light and dark blue arrows show the moments on the Ir and Ir' sublattices, with sites 1-4 and 1'-4', respectively. Curly arrows on the left side illustrate counter-rotating magnetic order between the consecutive sites along  $c$ . In unit cell 2, light ( $-\phi$ ) and dark ( $\phi$ ) shaded elliptical envelopes emphasize the confinement of the moments to alternate planes obtained from the  $a$ - $c$  plane by a rotation by  $\mp\phi$  around  $c$ . In unit cell 3, the color of bonds indicates the anisotropy axis of the Kitaev exchange for the three different bonds. Figure and caption reproduced from [33].

for the  $b$ - $c$  plane, which experiences the largest anisotropy next to similar data taken in the  $a$ - $c$  plane (middle) for comparison. Both the low field slope, which is proportional to the anisotropic susceptibility  $\alpha_{ij}$  and the kink field exhibit an order of magnitude change in anisotropy depending upon the field orientation. Such strong anisotropy observed in a spin  $\frac{1}{2}$  system highlights the strong orbital character arising from the spin-orbit coupling, in contrast to spin  $\frac{1}{2}$  Heisenberg antiferromagnetism [35, 64].

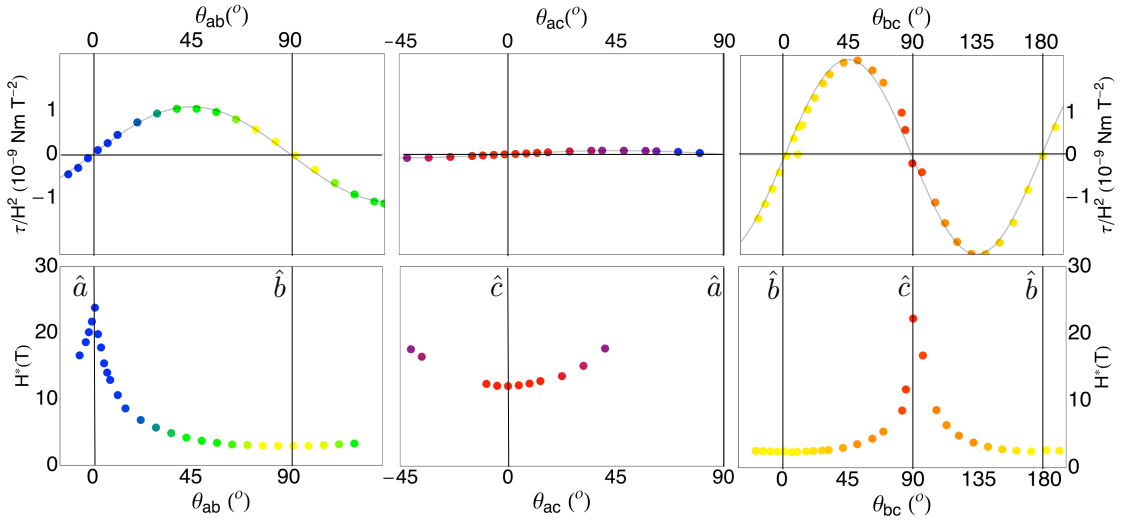


FIGURE 6.13: The anisotropic susceptibilities (top) and the kink field  $H^*$  (bottom) shown as a function of magnetic field orientation  $\theta_{ab}$  (left),  $\theta_{ac}$  (middle), and  $\theta_{bc}$  (right).

The observed ten-fold increase in  $\chi_b$  at low temperatures cannot be driven by the  $g$ -factor anisotropy of the local iridium environment, whose geometric constraints (Section 6.2) are temperature independent [35]. Because of a negligible octahedral distortion that preserves the same local environment between all nearest neighbor iridium, the magnitude of the exchange interactions  $J$  should be of comparable strength on all nearest neighbor bonds, ruling out spatial anisotropy and provoking the question as to what drives the order of magnitude increase in susceptibility

along  $b$ . We note that all the  $c$ -axis bonds have an Ir-O<sub>2</sub>-Ir plane normal to the  $b$ -axis, whether they preserve or rotate between the two honeycomb orientations (Figure 6.14). This is the only plane that is normal to a crystallographic axis. The evidence for the strong orbital character of the exchange coupling is necessary to explain the large magnetic susceptibility along  $b$  observed at low temperatures, as no other structural characteristics distinguish this principal direction from the other two. The strong spin-orbit interaction introduces a large magnetic anisotropy that is dependent upon the spatial orientation of the iridium-iridium bonds by coupling the spin to the symmetry of the local orbital environment. Across the

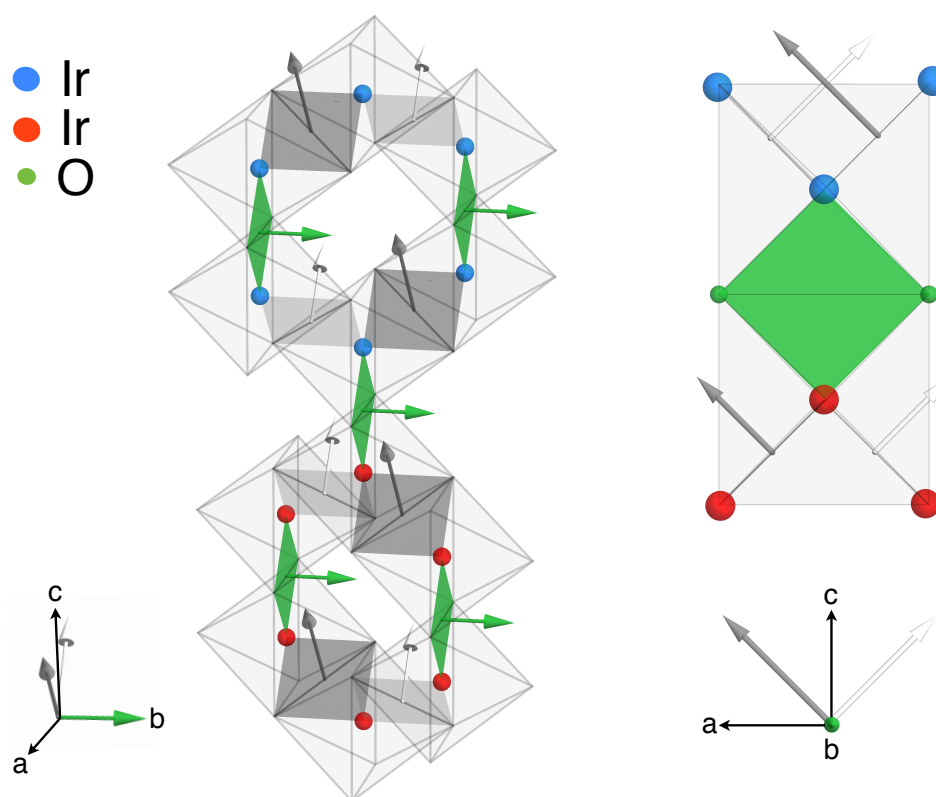


FIGURE 6.14: The Ir-O<sub>2</sub>-Ir planes defining three orthogonal directions of the spin-exchange, one parallel to  $\hat{b}$  and the other two parallel to  $(\hat{a} \pm \hat{c})$ .

Ir-O<sub>2</sub>-Ir planes, the spin-anisotropy of the exchange is expected to be enhanced by

the interfering exchange mechanism suggested by Jackeli and discussed in Chapter 2 [28]. The spin-anisotropic exchange across the  $c$ -axis link (exchange plane normal to  $b$ ) connects the observed order of magnitude increase in  $\chi_b$  to the structural properties required for entelechy of the Kitaev model. By extension, the strong spin-anisotropy should be present on all Ir-Ir links as no changes in the crystallographic symmetry are present on cooling below the magnetic ordering temperature [35]. Within each honeycomb, two Ir-O<sub>2</sub>-Ir planes exist for each type of bond (two planes normal to  $b$  and the other four planes normal to  $\hat{a} \pm \hat{c}$  in Figure 6.14). All of the remaining Ir-Ir links connecting the honeycombs are vertical with their Ir-O<sub>2</sub>-Ir plane normal to the  $b$ -axis, providing further support that the  $\hat{b}$  direction is special and that the Ir-O<sub>2</sub>-Ir plane is the distinguishing feature which determines the exchange anisotropy. The temperature dependence of  $\chi_b$  must therefore arise from spin-anisotropy in the exchange interactions [35].

## High Magnetic Field Properties of $\text{Li}_2\text{IrO}_3$

### 7.1 Temperature Dependent Torque in the 65 T Pulsed Field Magnet

The peculiar temperature dependence of the magnetic anisotropy (Chapter 6) in the  $b$ - $c$  plane turned my focus to this orientation for the high field measurements. This also presented the opportunity to map out the anisotropy of  $H^*$  for fields oriented in this plane. However, the large magnetic anisotropy of  $\text{Li}_2\text{IrO}_3$ , particularly in the  $b$ - $c$  plane at low temperatures, resulted in a very large torque signal that the lever could not withstand at high fields. A complete angle dependence proved especially difficult as the magnetic torque increases as one rotates the principal magnetic axes away from the applied field direction.

To try to get around this problem, the smallest orientable single crystals were first aligned with the magnetic field applied along a principal magnetic axis in an effort to minimize the torque signal in the pulsed magnetic fields. This was done for a  $\sim 50 \times 60 \times 100 \mu\text{m}^3$  single crystal, which was mounted on a fixed probe (no rotation) with the long body diagonal ( $\hat{b}$  axis) aligned as close as possible to the field direction (Figure 7.1).



FIGURE 7.1: Single crystal of  $\text{Li}_2\text{IrO}_3$  oriented on the lever for measurements of magnetic anisotropy in the  $b$ - $c$  plane with magnetic field applied parallel to the crystallographic  $\hat{b}$  direction. The lever is mounted on the side of a fixed angle probe.

The torque as a function of magnetic field was measured to 65 T at temperatures ranging from 0.5 K to 70 K (Figure 7.2). At temperatures below the magnetic ordering temperature of  $T = 38$  K and at small applied fields, the signal is parabolic and the kink is observed near 3 T, as expected for this particular field orientation from the low field data. As the temperature is increased, the low field slope decreases and changes sign at 70 K. This is also in agreement with the temperature dependence measured in the  $b$ - $c$  plane in the 20 T magnet. Rather unusually though, at low temperatures, the torque signal changes sign at high fields and becomes approximately five times larger than at low fields. Such behavior at high fields describes susceptibility along the  $\hat{c}$  axis becoming greater than the susceptibility along  $\hat{b}$ . The ordering of the principal components of the magnetic susceptibility at high fields resembles that obtained from the low field slope at

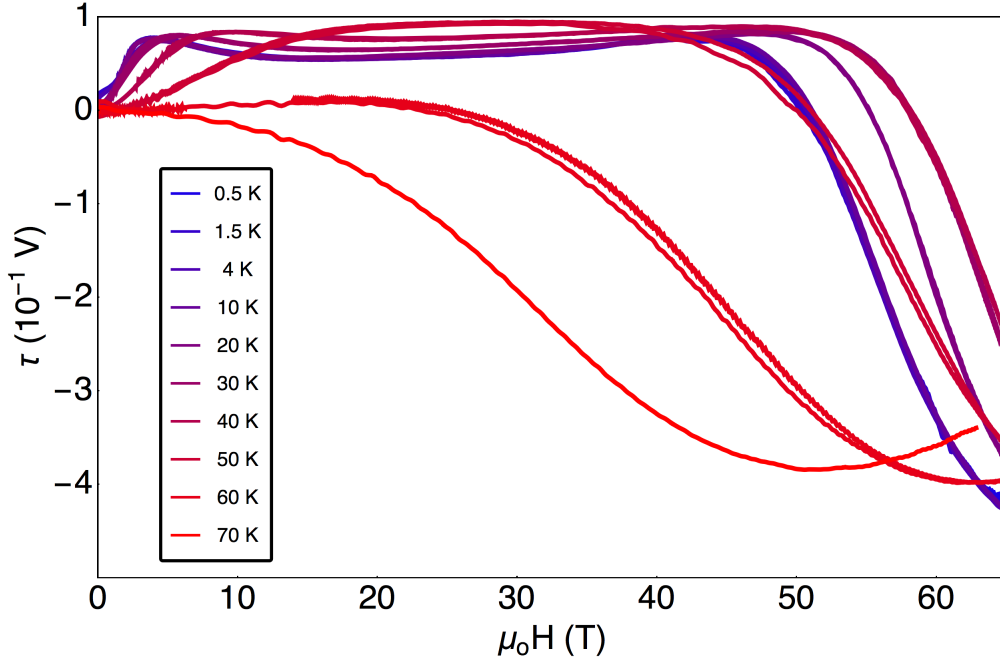


FIGURE 7.2: Temperature dependence of the magnetic torque of  $\text{Li}_2\text{IrO}_3$  with field applied along the crystallographic  $\hat{b}$  direction. The slope of the low field torque changes sign at 70K. At high fields, there is a sign reversal of the magnetic anisotropy that is accompanied by a large increase in the measured torque. The maximum field at which the torque signal changes sign occurs near the magnetic ordering transition temperature  $T = 38$  K.

high temperatures (Chapter 6), suggesting that large magnetic fields have a similar effect as high temperatures. The sign reversal at high fields is temperature dependent with a maximum near the magnetic ordering temperature. The torque continues to grow up to the largest measurable magnetic fields, indicating that the induced moment is not co-linear with the applied field. At magnetic fields that are large compared to the interaction energy scales, the magnetization is expected to align with the applied field and the torque will converge toward zero. Instead, the sharp change in the magnetic anisotropy at high fields in Figure 7.2 suggests a transition to a new magnetically ordered phase.

Unfortunately, the response due to the magnetic torque broke the lever near peak

field during the 70 K measurement. To decrease the size of the torque signal and further explore the high magnetic field properties of Li<sub>2</sub>IrO<sub>3</sub>, the crystal dimensions were reduced using a focused ion beam.

## 7.2 Angle Dependent Torque in the 65 T Pulsed Field Magnet

The focused ion beam (FIB), most commonly used in the semiconductor industry for imaging, deposition, and ablation of materials, can also be used for precision cutting. Here, the FIB was utilized to reduce a  $\sim 35 \times 40 \times 100 \mu\text{m}^3$  single crystal of Li<sub>2</sub>IrO<sub>3</sub> to nearly 1/10<sup>th</sup> of its original volume. The Nova 600 Nanolab at The Center for Integrated Nanotechnologies of Sandia National Laboratory combines high resolution SEM (scanning electron microscopy) and FIB capabilities in one machine. The dual-beam setup allowed use of the ion beam to cut the crystal and the electron beam for imaging. First, a thin cut, using an ion current of 2.1 nA, was made along the long body diagonal of the sample with the intention of splitting the diamond shape in half (Figure 7.3). Another cut, perpendicular to the first, was made  $\sim 18 \mu\text{m}$  from the top surface. The original cut, which was not made deep enough to divide the sample in two, was left as it was because the top layer was thin enough to reduce the torque signal for high field measurements even with both halves of the top surface. The tungsten needle inside the chamber was then used to pick up the newly cut sample and carefully orient it on the lever with the long body diagonal aligned with the long axis of the lever. For the high field measurements, the magnetic anisotropy in the *b-c* crystal plane was of interest, requiring the magnetic field to be applied in the plane of the diamond face normal and the long body diagonal. Ion induced deposition of platinum from a gas precursor was used to bond the crystal to the lever at several places. This helps to hold the crystal in place during the magnetic field pulse.

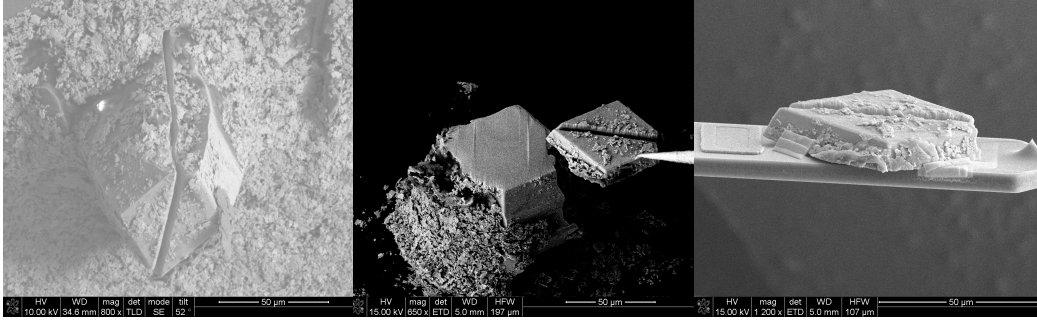


FIGURE 7.3: Left: Single crystal of  $\text{Li}_2\text{IrO}_3$  pressed into conducting tape with first cut made. Middle: Thin top layer of crystal moved with tungsten needle. Right: Reduced size crystal oriented on the lever with platinum deposited at several places where the edge of the crystal meets the lever.

A complete angle dependence of the magnetic torque was successfully measured to high magnetic fields of 60 T using the reduced size sample.  $\tau/H$  versus  $H$  (Figure 7.4) at  $T = 1.5$  K shows the magnetic anisotropy in the  $b$ - $c$  plane for several different angles of the applied magnetic field. The red (yellow) curves correspond to magnetic field applied along the  $\hat{c}$  ( $\hat{b}$ ) direction. Since there has been a significant reduction of the sample size, a greater fraction of the torque signal is due to the magnetoresistance of the lever in the high field measurements so that the data must be symmetrized. The torque data for symmetric angles about zero degrees were added together to find twice the magnetoresistance. The magnetoresistive contribution was then subtracted from each measurement to make each curve necessarily symmetric about the zero in  $\tau/H$ . The single red curve with magnetic field applied along  $c$  that experiences the highest  $H^*$  was symmetrized with its up sweep data (not shown due to electrical noise from a large  $\frac{dB}{dt}$ ). The up sweep data for this magnetically “hard” direction had a negative torque signal that changed sign at peak field due to an unstable equilibrium position of the lever.

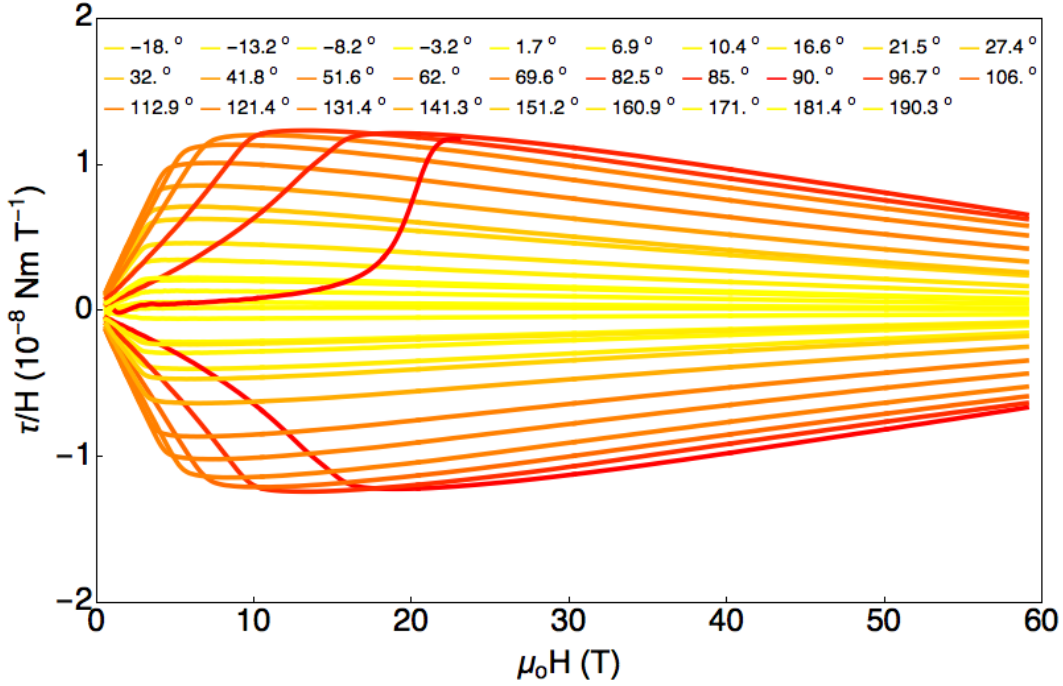


FIGURE 7.4:  $\tau/H$  as a function of magnetic field for rotation of the crystal in the  $b$ - $c$  plane. The colored curves correspond to magnetic field applied parallel to crystallographic directions indicated in Figure 7.5

As expected, at small applied fields, the slope of  $\tau/H$  is approximately equal to zero when the magnetic field is applied parallel to the principal magnetic directions and it follows a  $\sin 2\theta$  dependence. The magnetic anisotropy is highlighted by the kink in magnetization, which changes from  $\sim 3$  T to above 20 T as the crystal is rotated with respect to the field direction. The behavior of the low field slope and the kink field  $H^*$  as a function of angle are summarized in Figure 7.5.

Unexpectedly though, the high field reversal of the magnetic anisotropy experienced during the temperature dependence (Figure 7.2) is no longer observed. Certainly, at low temperatures with magnetic field applied along the  $\hat{b}$  direction (yellow curves), we expect the torque to change sign and continue to increase with large applied magnetic fields. Instead, the torque seems to be converging toward zero at large fields for all field orientations, suggesting a saturation of the

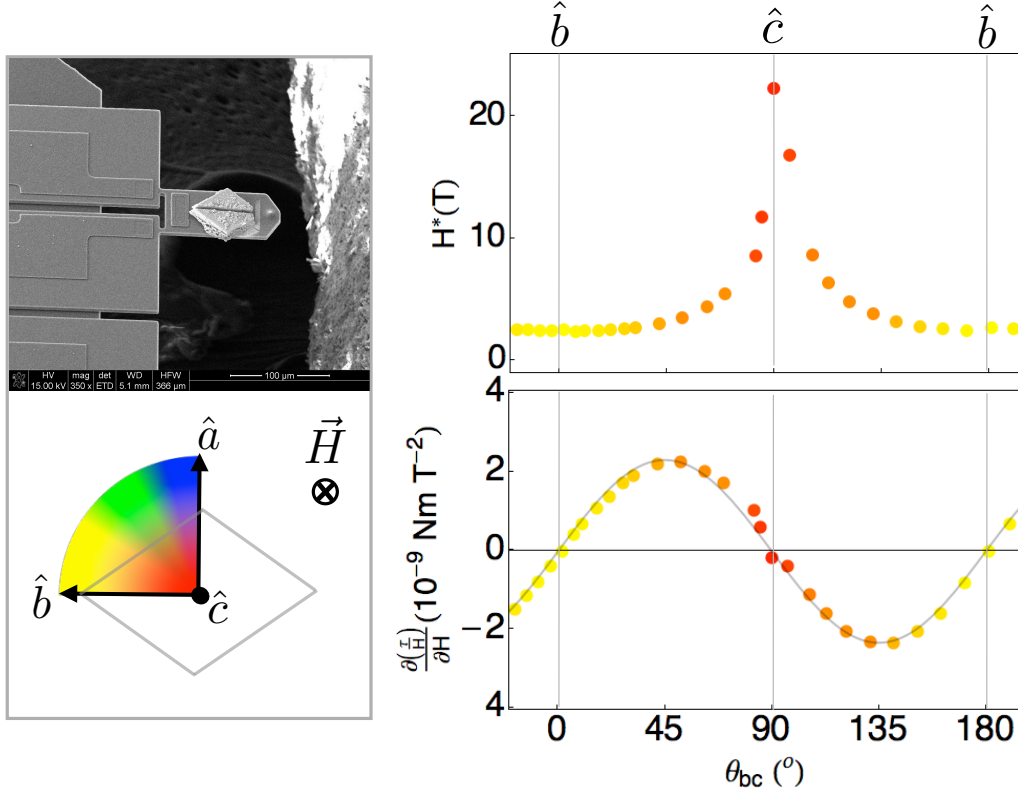


FIGURE 7.5: Left: FIB crystal oriented on lever for  $b$ - $c$  plane of rotation. Top right: Kink field,  $H^*$  plotted as a function of angle. Bottom right: Angle dependence of low field linear response.

magnetization. It is important to confirm the presence of a high field transition and a distinct magnetically ordered phase above the kink field  $H^*$ , as this may help to identify what drives the system to long range order at low temperatures. Saturation of the magnetic anisotropy would put limits on the relative strength of the exchange interactions, in essence revealing how “Kitaev”-like the exchange interactions are. The inconsistency in the data sets might suggest a change in the sample quality as a result of the FIB cutting process, perhaps causing surface damage or oxidation. A more likely explanation is that the sample was misaligned in Figure 7.2, where SEM imaging was not used for alignment and any side of the

crystal when looking down on the diamond face could easily be mistaken for the diamond face itself. Despite the fact that the kink field  $H^*$  occurs at roughly 3 T (Figure 7.2), just as anticipated for field applied parallel to the crystallographic  $\hat{b}$  axis in the temperature dependence, this behavior is also expected for a broad range of angles around  $\hat{b}$  (Figures 5.15 and 7.5). If the sample were mounted on its side and the field was applied toward a corner, believing it to be the long body diagonal, the field direction would still be within  $20^\circ$  of the  $\hat{b}$  axis with a kink field at approximately 3 T.

With a misalignment assumed and hopefully remounted to reproduce the data in Figure 7.2, the crystal has very recently been remeasured. A high field reversal of the magnetic anisotropy has been confirmed when the magnetic anisotropy between the two honeycomb planes is measured, which do not coincide with the principal components of magnetic anisotropy. The three-dimensionality of the structure, combined with three different orientations of the exchange planes, makes it difficult to disentangle the origin of the anisotropy. A more thorough investigation of  $\text{Li}_2\text{IrO}_3$  in high magnetic fields is needed (discussion continues at the end of this chapter).

### 7.3 Angle Dependent Torque in the 100 T Pulsed Field Magnet

The angle dependence of the magnetic torque can be approximated at large applied magnetic fields. As an example, the magnetic anisotropy in the  $b$ - $c$  plane will be considered where  $\phi$  represents the angle between the net magnetization vector  $M$  in the  $b$ - $c$  plane and the  $\hat{b}$  axis. An expression for the free energy  $E$  can be written as a series expansion of the order parameter  $M$ , which must obey the symmetry of the system  $E = E_o + AM^2 - HM$ , where  $A$  is a constant,  $E_o$  is a shift in energy which can be set to zero,  $H$  is the applied magnetic field and  $M$  is the

magnetization. The first term in the free energy represents a local anisotropic contribution and the second term is the interaction of  $M$  with the external field  $H$ . With suitable coefficients chosen for the order parameter and with the field and magnetization in the  $b$ - $c$  plane, the energy at high fields is

$$E = \frac{M_b^2}{2\chi_b} + \frac{M_c^2}{2\chi_c} - M_b H_b - M_c H_c. \quad (7.1)$$

In the case that  $M_b$  and  $M_c$  have a linear response to magnetic field (i.e.  $M_b = \chi_b H_b$ ), the free energy reduces to  $E = -\mathbf{M} \cdot \mathbf{H}$ . However, at large applied magnetic fields, the observed magnetic response is clearly nonlinear, which is why the first two terms must be included in the free energy. Defining  $\theta$  as the angle between the external field and the magnetization, the energy can be rewritten as

$$E = \frac{M \cos^2 \phi}{2\chi_b} + \frac{M \sin^2 \phi}{2\chi_c} - MH \cos \phi \cos \theta - MH \sin \phi \sin \theta. \quad (7.2)$$

For the remainder of this discussion,  $M$  will be set equal to one, constraining the overall length of the magnetization vector. This is reasonable to assume at high fields as it is likely that the magnetization is no longer growing in length, but only rotating toward the magnetic field direction. With the identity  $\cos(\alpha \pm \beta) = \cos \alpha \cos \beta \mp \sin \alpha \sin \beta$ , the last two terms can be rewritten as

$$E = \frac{\cos^2 \phi}{2\chi_b} + \frac{\sin^2 \phi}{2\chi_c} - H \cos(\phi - \theta). \quad (7.3)$$

The torque, which is the partial derivative of the energy with respect to the angle  $\theta$ , is then equal to

$$\tau = \frac{\partial E(\theta, \phi^*(\theta))}{\partial \theta} = \frac{\partial E(\theta, \phi^*)}{\partial \theta} + \frac{\partial E}{\partial \phi} \frac{\partial \phi^*}{\partial \theta}. \quad (7.4)$$

Because  $\frac{\partial E}{\partial \phi} = 0$  by definition, the torque is equal to

$$\tau = \frac{\partial E(\theta, \phi^*)}{\partial \theta} = -H \sin(\phi - \theta). \quad (7.5)$$

To minimize the energy with respect to the angle  $\phi$ , the partial derivative

$$\frac{\partial E}{\partial \phi} = -\frac{\sin 2\phi}{2\chi_b} + \frac{\sin 2\phi}{2\chi_c} + H \sin(\phi - \theta) \quad (7.6)$$

is found with the identity  $2 \cos \alpha \sin \alpha = \sin 2\alpha$  and set equal to zero. By defining and substituting  $\Delta\phi = \phi - \theta$  into the expression, a Taylor series expansion evaluated at  $\theta$  allows us to approximate the torque

$$-H \sin(\Delta\phi) = \frac{c}{2} \sin 2\theta + c \cos 2\theta \Delta\phi, \quad (7.7)$$

where  $c \equiv \frac{1}{\chi_c} - \frac{1}{\chi_b}$ . At large applied fields,  $\Delta\phi$  is assumed to be small and can be approximated as

$$\Delta\phi = -\frac{c}{2} \frac{\sin 2\theta}{H}. \quad (7.8)$$

Thus, the torque  $\tau = -H \Delta\phi$  at large applied fields also follows a  $\sin 2\theta$  dependence

$$\tau = \frac{c}{2} \sin 2\theta. \quad (7.9)$$

This equation also suggests that the limiting torque at large magnetic fields is finite – contrary to the belief that a large enough magnetic field will fully align the magnetization along the field direction and result in zero torque. To check the high field response, let's consider again a magnetization vector  $M$  in the  $b$ - $c$  plane that is at an angle  $\theta$  from an external field  $H$  aligned very near the  $\hat{c}$  direction. Now, upon increasing the magnetic field, the angle  $\theta$  will decrease, where the

$\hat{b}$  component of magnetization is given by  $M_b = H \tan \theta$ . At very small angles, this can be approximated as  $M_b = H \theta$ . The angle  $\theta$ , which scales as  $1/H$ , leads to a small, but finite  $\hat{b}$  component of magnetization at high magnetic fields that generates a torque  $\tau = MH \sin \theta$  of finite value. Now, with some idea of how the torque should behave at very large applied magnetic fields, greater than the energy of the exchange interactions, the high field measurements are reconsidered.

Because the temperature dependence of the low field slope had been independently verified in the 20 T magnet and the high field collapse of the magnetic anisotropy had a temperature dependence that correlated with the magnetic ordering temperature of  $\text{Li}_2\text{IrO}_3$ , it was convincingly apparent that the high field transition (Figure 7.2) was a result of the magnetic anisotropy of  $\text{Li}_2\text{IrO}_3$  and was not an artifact of the experimental method. Also, the featureless high field torque observed in the angle dependence (Figure 7.4) was measured on a different sample that could have been altered by the FIB cutting process. Last but not least, there was no sign of magnetic saturation observed for any orientations of magnetic fields up to 65 T, warranting further investigation into  $\text{Li}_2\text{IrO}_3$  with higher magnetic fields. For all of these reasons, magnetic torque measurements were extended to higher fields using the 100 T pulsed field magnet.

A small single crystal, different from those used for previous high field measurements, was oriented for magnetic anisotropy measurements in the  $a$ - $c$  plane at  $T = 4$  K.  $\tau/H$  is shown for magnetic fields up to 90 T in Figure 7.6 with field very closely aligned to the  $\hat{a}$  and  $\hat{c}$  direction (blue and red curves respectively). The low field kink (although difficult to see with field applied along  $\hat{a}$  in  $\tau/H$ , but clearly visible in its derivative) is used for a very careful alignment of the crystal with the field direction before a full field magnetic pulse. Interestingly, with field along the  $\hat{c}$  direction, the high field transition appears at approximately 65 T, albeit subtly.

It should be noted that this feature is not longer observed for any small rotation of the field away from the  $\hat{c}$  direction.

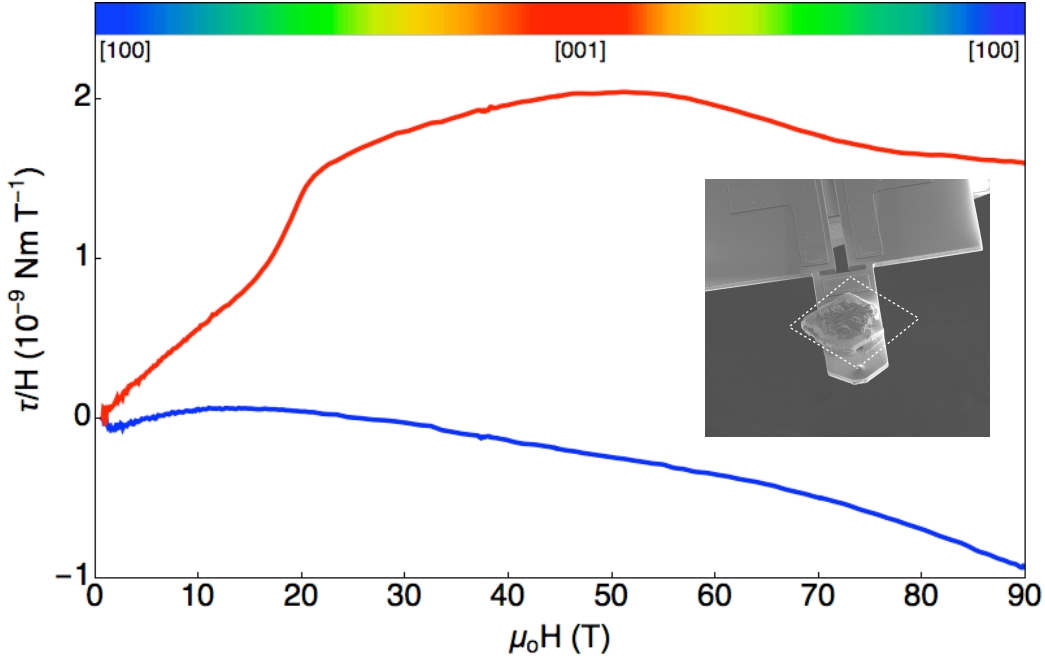


FIGURE 7.6:  $\tau/H$  as a function of magnetic field for magnetic anisotropy measurements in the  $a$ - $c$  plane at  $T = 4$  K. The blue (red) curve shows magnetic field applied along the crystallographic  $\hat{a}$  ( $\hat{c}$ ) direction. The inset shows orientation of the crystal on the lever to probe the magnetic anisotropy in the  $a$ - $c$  crystal plane.

Similarly, the measurements were repeated on a crystal oriented to measure magnetic anisotropy in the  $b$ - $c$  plane. Due to the large magnetic anisotropy in this plane, this crystal was also reduced in size using the FIB to minimize the torque signal. Figure 7.7 shows  $\tau/H$  for magnetic field aligned with the crystallographic  $\hat{c}$  direction (red curve). This is the only field orientation in which the magnetic anisotropy abruptly collapses to zero at high fields. The orange curve shows a rotation of the lever with respect to the applied field of  $\sim 10$  degrees from  $\hat{c}$  towards  $\hat{b}$ , where the high field feature has most likely moved to an inaccessible field

range. A finer angle dependence of the torque with field near the  $\hat{c}$  axis was done to maximum field strength, with no indication of a high field transition.

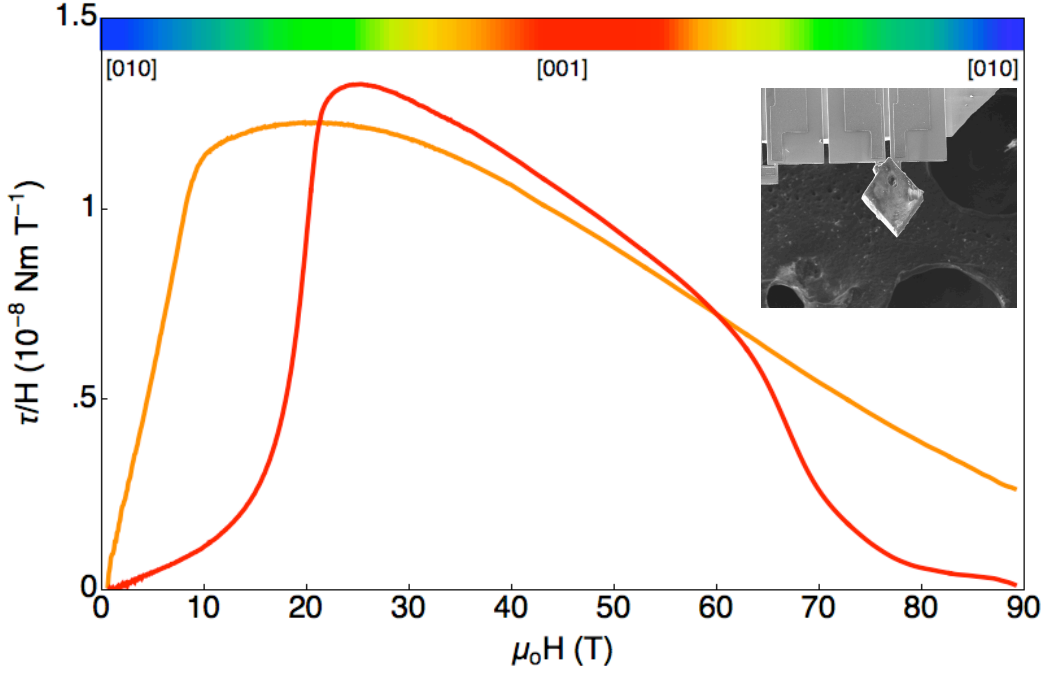


FIGURE 7.7:  $\tau/H$  as a function of magnetic field for magnetic anisotropy measurements in the  $b$ - $c$  plane at  $T = 4$  K. The red curve shows magnetic field applied along the crystallographic  $\hat{c}$  direction. A small rotation of the magnetic field away from this direction shows a high field transition that is strongly angle dependent (orange curve). The inset shows orientation of the crystal on the lever to probe the magnetic anisotropy in the  $b$ - $c$  crystal plane

The high field torque measured to 90 T (Figure 7.7) shows a transition toward magnetic saturation at approximately 70 T when magnetic field is applied close to the  $\hat{c}$  direction. Like the low field magnetic response, the high field transition appears to be highly anisotropic as exemplified by the disappearance of the transition when the lever is rotated by any small angle from the  $\hat{c}$  direction. Despite the magnetic order of the intermediate phase (between roughly 20 and 70 T for this particular field and crystal orientation) remaining unknown, the high field transition provides a lower limit for the energy scales required to overcome the exchange

interactions in this system. This energy scale coincides with the temperature scale ( $\sim 100$  K) below which the magnetic susceptibility deviates from Curie-Weiss behavior (Figure 6.9). It is also consistent with reports that the zigzag magnetic correlations in Na<sub>2</sub>IrO<sub>3</sub> survive at least up to  $T \sim 70$  K [36].

## 7.4 Concluding Discussion and Unanswered Questions

The temperature dependence of the magnetic anisotropy, as obtained from the low field torque measurements, can be well understood at high temperatures by a  $g$ -factor anisotropy reflective of the crystal structure. At temperatures greater than the  $T_N$  ordering temperature, the exchange interactions come into play, as emphasized by a reordering of the principal components of susceptibility upon cooling and a drastic increase in the anisotropy of the magnetic susceptibility at low temperatures. Just as in almost all magnetic systems, even those which are specifically designed to try to enhance frustration in the exchange interactions, something drives Li<sub>2</sub>IrO<sub>3</sub> to long-range magnetic order. Nevertheless, the presence of the unexpectedly complex and new magnetic phase and the uncharacteristically anisotropic magnetic susceptibility suggests that Li<sub>2</sub>IrO<sub>3</sub> is displaying many of the desired properties that one might expect of a system that hosts a spin liquid. The torque data shows promise that exchange anisotropy is responsible for the magnetic frustration. This point is most clear when comparing to the layered honeycomb structure Na<sub>2</sub>IrO<sub>3</sub>; where larger octahedral distortions are thought to destroy the exchange anisotropy and a smaller frustration parameter is observed, despite an ordering temperature that is more greatly suppressed compared to Li<sub>2</sub>IrO<sub>3</sub>. In this light, Li<sub>2</sub>IrO<sub>3</sub> offers hope that the theoretical foundation is well-placed and that a strong enhancement of the exchange anisotropy due to a perfectly undistorted octahedral environment can be obtained through chemical doping or pressure.

Despite our current understanding, Li<sub>2</sub>IrO<sub>3</sub> probably asks more questions than it answers. Some of the most obvious are:

How strong are the exchange interactions?

This system shows non-Curie-Weiss like behavior up to room temperature and a magnetic field of 90 T fails to saturate the moments along the field direction for all but one direction of applied field. These are extreme energy scales that cannot overcome the strength of the exchange interactions, suggesting that  $J$  is very large compared to  $T_N$  and there is a large degree of frustration.

What is the value of the  $g$ -factor?

The spin on iridium is subject to a large spin-orbit coupling that is likely responsible for the anisotropy in the exchange, but we have had no success in measuring the  $g$ -factor with EPR. It is possible that at all measurable temperatures, the exchange interactions are strongly influencing the measurement. Furthermore, it is unclear how a  $g$ -factor anisotropy would affect the anisotropy in the exchange and whether these factors cooperate or compete with each other, specifically in the intermediate temperature regime where both are likely to exist and may heavily influence the fate of the ground state.

What is the magnetic order of the high field phase?

In the phase above  $H^*$ , the finite torque signal reveals that the induced moment is not colinear with the applied field, consistent with a finite slope observed at these fields in magnetization data [35]. This observation, along with the anomalously small field-induced moment, suggests the presence of new magnetically ordered states at high fields. The exact magnetic order is still unknown, but by applying a small magnetic field of 3 T along the  $\hat{b}$  direction, this order could be studied with magnetic x-ray diffraction and could help elucidate what drives the the long-range order observed at low temperatures.

Where do we go from here?

High magnetic fields are extremely important for understanding exotic materials,

such as Li<sub>2</sub>IrO<sub>3</sub>. The magnetic field strength required to destroy magnetic order and fully spin-polarize the system reveals the energy scale of the exchange interactions. In the case of torque magnetometry, high field saturation should directly provide the anisotropy in the exchange interactions, making this an incredibly powerful tool to investigate Kitaev spin liquid candidates. The most recent high field torque measurements on Li<sub>2</sub>IrO<sub>3</sub> (unpublished) show a reversal of the magnetic anisotropy at high fields, but only when magnetic anisotropy between the two honeycomb planes is measured. It should be noted that the planes of the XY-like magnetic order (shaded discs in Figure 6.12) coincide with the honeycomb planes. Analysis of these measurements is currently underway with the hopes of connecting the magnetic structure to the magnetic anisotropy to find the relative magnitude of the anisotropy in the exchange interactions.

## Bose-Einstein Condensation in a Molecular Magnet

Molecular magnets are attractive systems for understanding and manipulating quantum states [65]. Their associated energy scales are often experimentally accessible and can easily be tuned with magnetic field, chemical doping, or pressure. One such example is  $[\text{Cu}(\text{pyz})(\text{gly})](\text{ClO}_4)^*$ , which in addition to its experimental lure, has reduced dimensionality that is responsible for magnetic behavior representative of a Bose-Einstein condensate (BEC) of magnons. The disordered ground state of  $[\text{Cu}(\text{pyz})(\text{gly})](\text{ClO}_4)$  can be driven through a quantum critical point into its magnetic/bosonic state, where the particle density is tuned by the strength of an applied magnetic field. Such model systems are ideal for elucidating quantum critical behavior and associated emergent phases.

### 8.1 Structural Properties of $[\text{Cu}(\text{pyz})(\text{gly})](\text{ClO}_4)$

$[\text{Cu}(\text{pyz})(\text{gly})](\text{ClO}_4)$  is a molecular magnet made up of dimers of antiferro-

---

\*Lancaster, T. et al. Controlling magnetic order and quantum disorder in molecule-based magnets. PRL 112, 207201 (2014). J.L.M., A.M.B., R.D.C., K.E.C., and H.E.T synthesized the crystals. T.L., T.A.W.B., F.X., S.J.B., F.R.F., S.G., J.S.M., P.J.B., F.L.P., and C.B. did the  $\mu\text{SR}$  measurements. L.H. and J.W. did the heat capacity measurements. P.A.G., J.S., and C.V.T. did the pulsed field magnetization measurements. R.D.M. and K.A.M. did the EPR measurements. J.A.S. determined the X-ray structure.

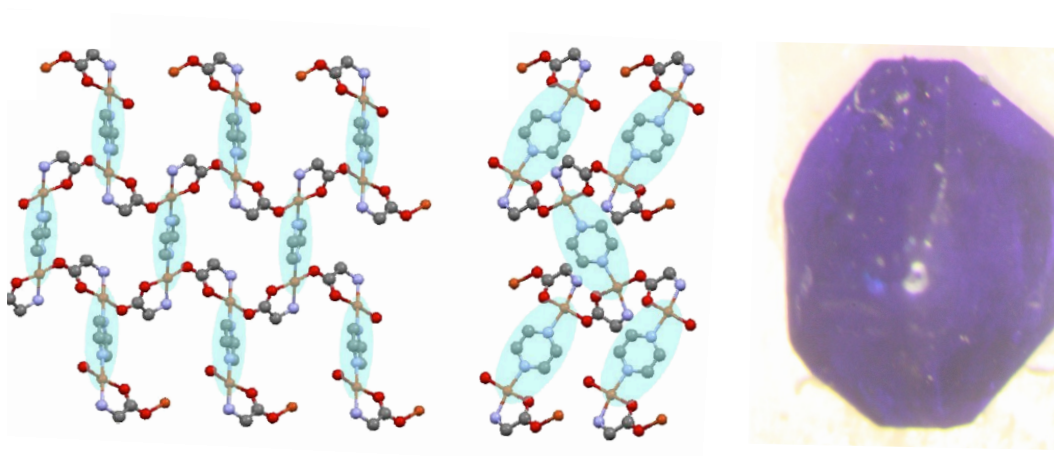


FIGURE 8.1: (Left)  $[\text{Cu}(\text{pyz})(\text{gly})](\text{ClO}_4)$  viewed along the crystallographic  $\hat{a}$  axis and (Middle) the  $\hat{c}$  axis showing pairs of  $\text{Cu}^{2+}$  ions (light orange circles) strongly coupling through pyz ligands to form alternating dimers. Dimers are shaded, and the  $\text{ClO}_4$  ions have been removed for clarity [65]. (Right) Picture of a single crystal of  $[\text{Cu}(\text{pyz})(\text{gly})](\text{ClO}_4)$ , which forms as purple blocks with the monoclinic crystal structure manifesting itself as oblique faces in the crystal morphology. Figure and caption modified from [65].

magnetically interacting  $\text{Cu}^{2+}$  ( $3d^9$ ) spins. The pyrazine (pyz) ligands, effective mediators of magnetic exchange, couple the  $\text{Cu}^{2+}$  ions forming each dimer. The dimers are connected by glycine (gly) bridges to create corrugated sheets, with  $\text{ClO}_4^-$  ions laying between these sheets [65] (Figure 8.1). The exchange through the gly groups and  $\text{ClO}_4^-$  ions is expected to be comparatively weak, resulting in strongly coupled dimer units that are weakly coupled to their neighbors [65].

## 8.2 Spin and Bosonic Representations of Spin Dimer Systems

The spin Hamiltonian describing a network of weakly coupled dimers can be written as

$$\mathcal{H} = J \sum_i \mathbf{S}_{1,i} \cdot \mathbf{S}_{2,i} + \sum_{mni j} J'_{mni j} \mathbf{S}_{m,i} \cdot \mathbf{S}_{n,j} - g\mu_B B \sum_{mi} S_{m,i}^z, \quad (8.1)$$

where  $i, j$  is used to label the dimers and  $m, n = 1, 2$  labels their magnetic sites [66]. In the absence of an applied magnetic field and in the case of an intra-dimer exchange interaction  $J$  that is much stronger than the inter-dimer coupling  $J'$ , two strongly coupled spins per dimer results in a ground state that is a direct product of singlet states ( $S_{\text{total}} = 0$ , Figure 8.2)

$$|\tilde{\downarrow}\rangle = \frac{1}{\sqrt{2}}[|\uparrow\downarrow\rangle - |\downarrow\uparrow\rangle]. \quad (8.2)$$

The ground state is then a quantum disordered paramagnet [65].

An applied magnetic field will Zeeman split the degenerate triplet states ( $S_{\text{total}} = 1$ ), causing the  $s^z = 1$  state to be the lowest-lying excited state

$$|\tilde{\uparrow}\rangle = |\uparrow\uparrow\rangle. \quad (8.3)$$

By projecting the Heisenberg Hamiltonian (Equation 8.1) onto this low-energy singlet-triplet subspace (ignoring the unoccupied  $s^z = 0$  and  $s^z = -1$  states), each dimer can be treated as one effective site with two possible states – effective spin 1/2 down (Equation 8.2) or up (Equation 8.3) [68]. These two possible states can be associated with the absence or presence of a hard core boson: the empty sites correspond to the singlet states  $|\tilde{\downarrow}\rangle = |0\rangle$ , while the occupied site is represented

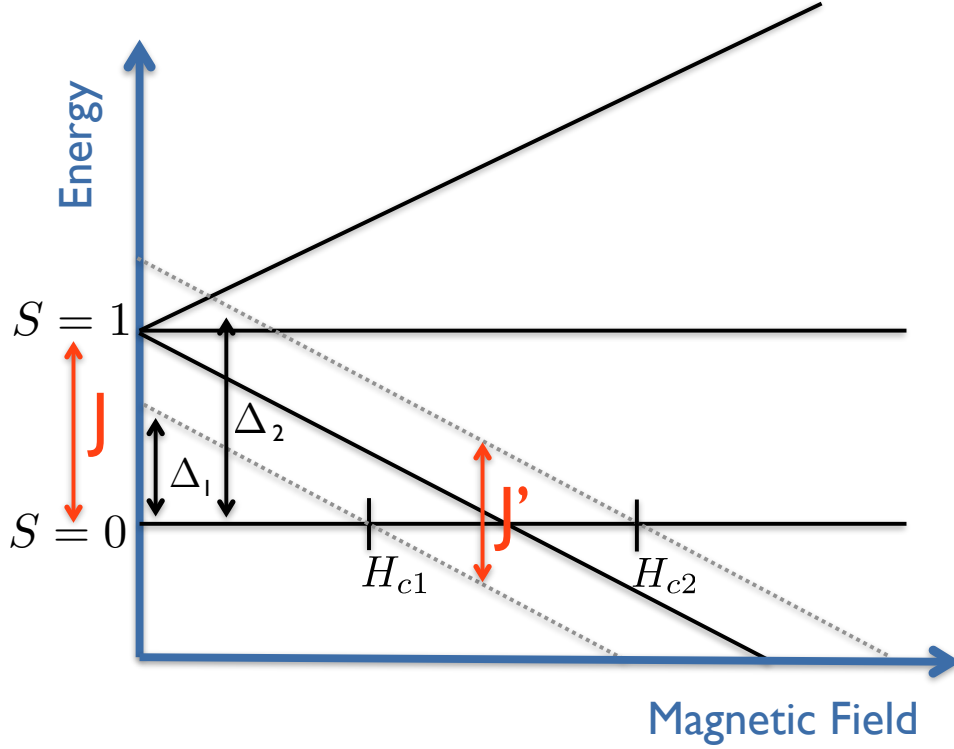


FIGURE 8.2: Energy spectrum of a weakly interacting spin dimer system in an applied magnetic field. The Zeeman splitting of the  $s^z = 1$  triplon leads to a magnetically ordered phase between  $H_{c1}$  and  $H_{c2}$ . Figure modified from [67].

by the triplet state  $|\tilde{\uparrow}\rangle = b^\dagger|0\rangle$ , where  $b^\dagger$  is the boson creation operator [67]. The effective spin operators [69]

$$\begin{aligned}
 \sigma^z|\tilde{\downarrow}\rangle &= -\frac{1}{2}|\tilde{\downarrow}\rangle & \sigma^z|\tilde{\uparrow}\rangle &= +\frac{1}{2}|\tilde{\uparrow}\rangle \\
 \sigma^+|\tilde{\downarrow}\rangle &= |\tilde{\uparrow}\rangle & \sigma^+|\tilde{\uparrow}\rangle &= 0 \\
 \sigma^-|\tilde{\downarrow}\rangle &= 0 & \sigma^-|\tilde{\uparrow}\rangle &= |\tilde{\downarrow}\rangle
 \end{aligned} \tag{8.4}$$

can be mapped to boson annihilation and creation operators with the Holstein-Primakoff transformation [70]. Using this language, the low energy Hamiltonian

becomes

$$\mathcal{H} = t \sum_{i,j} (\mathbf{b}_i^\dagger \mathbf{b}_j + \mathbf{b}_j^\dagger \mathbf{b}_i) + V \sum_{i,j} \hat{n}_i \hat{n}_j + \mu \sum_i \hat{n}_i, \quad (8.5)$$

where the chemical potential is  $\mu = J - g\mu_B H$  and  $t - V = J'/2$ .  $\hat{n}_i = \mathbf{b}_i^\dagger \mathbf{b}_i$  is the number operator and is equal to 0 or 1 [71]. Equation 8.5 describes nearest-neighbor hopping and repulsive interactions between the bosons [71]. For magnetic fields smaller than  $H_{c1}$ , the ground state is empty due to a large and positive chemical potential. Inter-dimer coupling on nearest neighbor empty and occupied states switches their position, similar to triplet hopping [67]. Thus, the inter-dimer coupling leads to dispersion of the triplet states into bands of energy called triplons (Figure 8.2). At a magnetic field  $H_{c1}$ , the bottom of the  $s^z = 1$  triplon becomes degenerate with the disordered ground state, populating a finite number of bosons, and a magnetic phase transition is observed (Section 8.3). The particle density increases linearly with applied magnetic field from  $H_{c1}$  to  $H_{c2}$ , where every site is occupied by a boson and magnetic saturation occurs.

### 8.3 Temperature-Magnetic Field Phase Diagram

The temperature-magnetic field phase diagram of  $[\text{Cu}(\text{pyz})(\text{gly})](\text{ClO}_4)$  was studied with PDO (proximity detector oscillator) – an *rf* technique used to measure the magnetic susceptibility that has compatibility with pressure cells. The circuit, which typically oscillates in the frequency range of 10-50 MHz, must be mixed down before the measurement to a frequency below the 20 MHz card digitizer ( $\sim 2.3$  MHz in Figure 8.3). Magnetic field sweeps up to 10 T were performed at several temperatures ranging from 650 mK to 10 K. A shift in frequency is observed both upon entering and exiting the magnetically ordered phase at roughly 2 and 6 T (Figure 8.3). In zero magnetic field and up to the low field magnetic

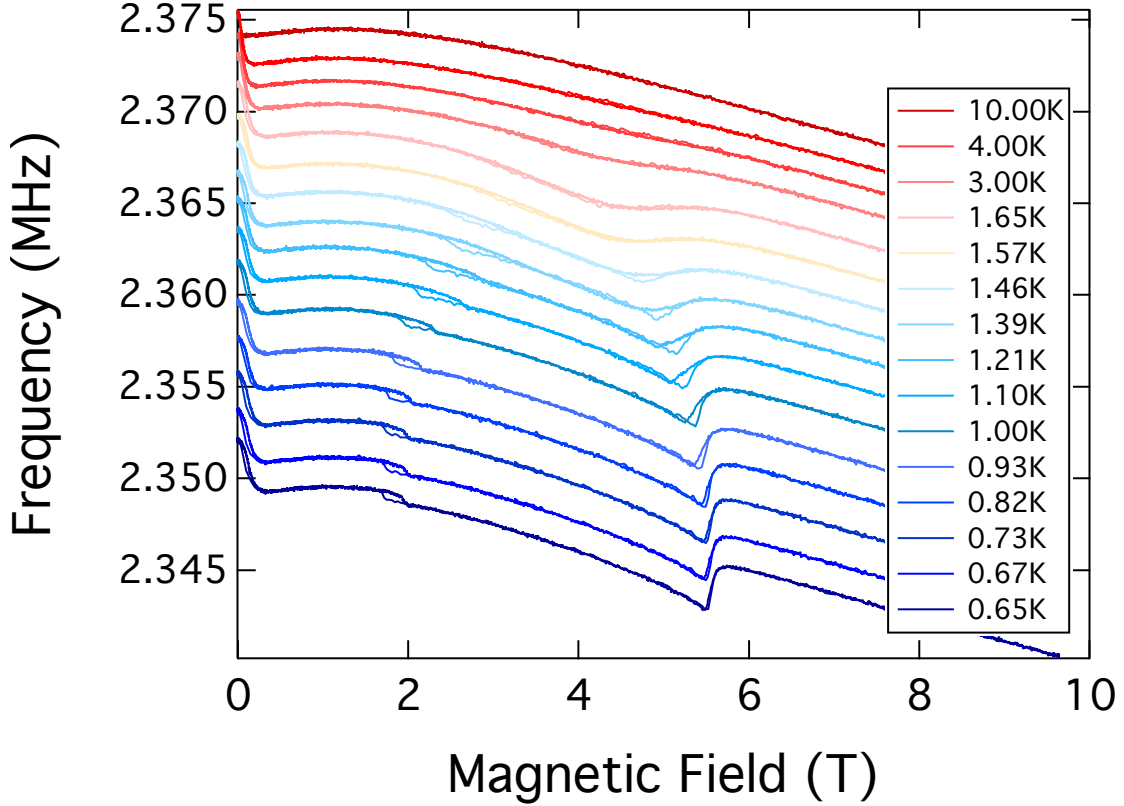


FIGURE 8.3: The magnetic phase boundary of  $[\text{Cu}(\text{pyz})(\text{gly})](\text{ClO}_4)$  as detected with PDO. The shift in frequency due to changes in the sample's magnetic response is plotted as a function of applied magnetic fields up to 10 T for several temperatures ranging from 650 mK to 10 K. The curves are offset vertically for clarity.

transition, the quantum state is a disordered one comprised of a direct product of singlets. The transition to magnetic order at  $H_{c1} \sim 2$  T coincides with the closing of the spin gap  $\Delta_1 = g\mu_B H_{c1}$  – the energy difference between the bottom of the triplon band and the singlet state at zero magnetic field (Figure 8.2). Thus,  $H_{c1}$  corresponds to a critical value of the chemical potential at which a finite number of bosons are being populated, after which point the particle density will increase linearly with magnetic field strength [68]. The ordered phase between  $H_{c1}$

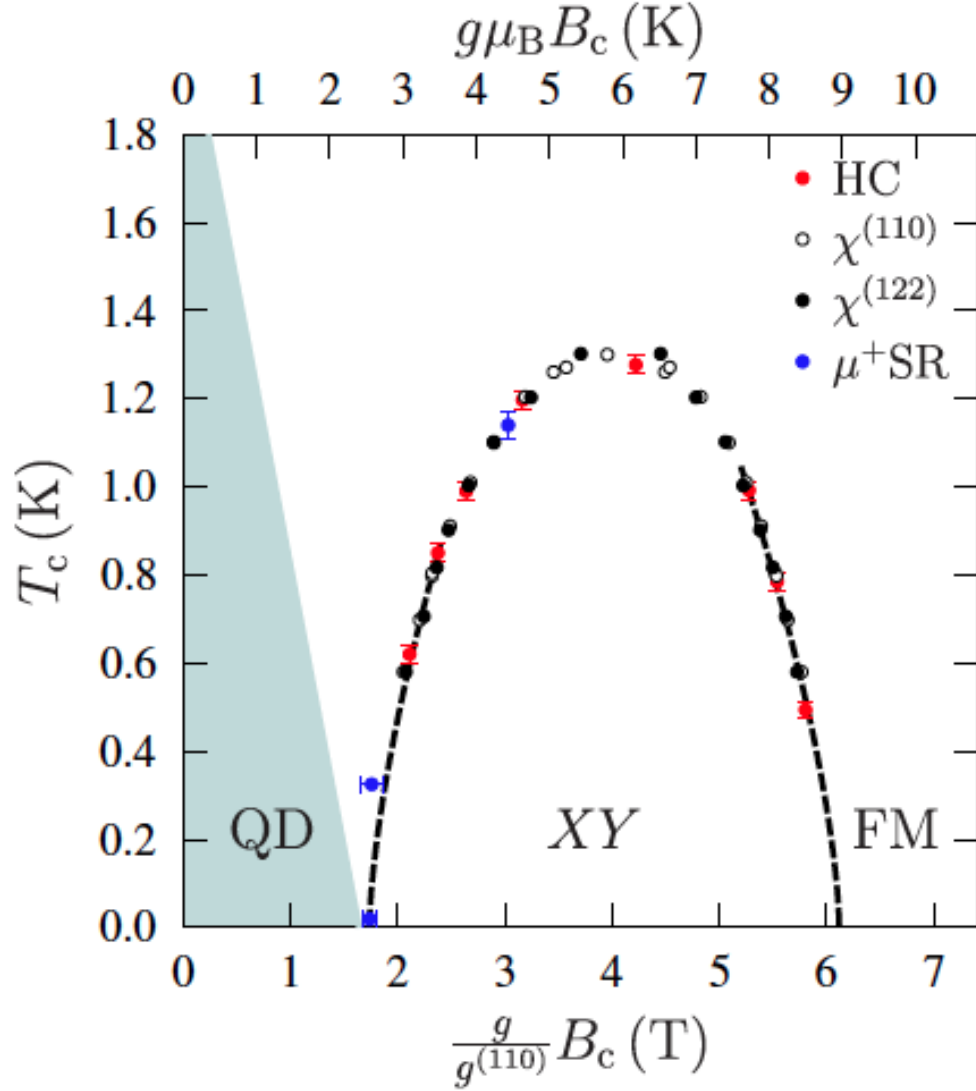


FIGURE 8.4: The temperature-field phase diagram for  $\text{Cu}(\text{pyz})(\text{gly})(\text{ClO}_4)$  showing quantum critical points at  $g\mu_B B_c = 2.5(1)$  and  $9.0(2)$  K. Dashed line shows the expected behavior of the phase boundaries with a power law exponent of  $2/3$  predicted for the BEC of magnons model. Figure and caption reproduced from [65].

and  $H_{c2}$  can then be described as a network of interacting bosons, which depends upon the kinetic energy and repulsive interactions of the bosons (Equation 8.5) [67]. The field-tunable increase in boson density will continue until saturation of

magnetization occurs at  $H_{c2} \sim 6$  T.

The temperature-magnetic field phase boundary depends slightly upon the crystal orientation with respect to the applied magnetic field, reflecting the effects of  $g$ -factor anisotropy (compare Figures 8.3 and 8.4). The phase diagram observed with PDO coincides with that observed in reference [65] by measurements of magnetic susceptibility, heat capacity, and muon-spin relaxation when the appropriate  $g$ -value is used (determined with EPR measurements – next section). The position of the phase boundary can be scaled for each measurement by plotting the temperature against  $g\mu_B B_c$  (Figure 8.4).

## 8.4 EPR Results

Many of the results in this section are published in the supplementary information of reference [65]. Because the constituent spins reside at the Cu sites, the  $g$ -factor was expected to be approximately 2, close to that of a free-electron spin with weak spin-orbit coupling. To check the  $g$ -value and determine whether the scaling of the phase boundary was a result of the  $g$ -factor anisotropy, electron paramagnetic resonance measurements were performed on a single crystal of  $[\text{Cu}(\text{pyz})(\text{gly})](\text{ClO}_4)$ . This also allowed us to investigate the possibility of two different Cu sites in the structure, which would show up as two absorption lines in the EPR spectra. To determine the  $g$ -factor, the field at which an EPR absorption occurs due to a spin excitation in  $[\text{Cu}(\text{pyz})(\text{gly})](\text{ClO}_4)$  is determined for several frequencies of the 10-40 GHz multi-moded cavity at a temperature of 1.75 K. The selected microwave frequency is plotted as a function of magnetic field where the EPR absorption occurs in Figure 8.5.

The frequency-magnetic field scaling is used to determine the  $g$ -factor by  $g = h\nu/\mu_B B$ . For magnetic field applied near the direction labelled  $\beta$  in the inset of

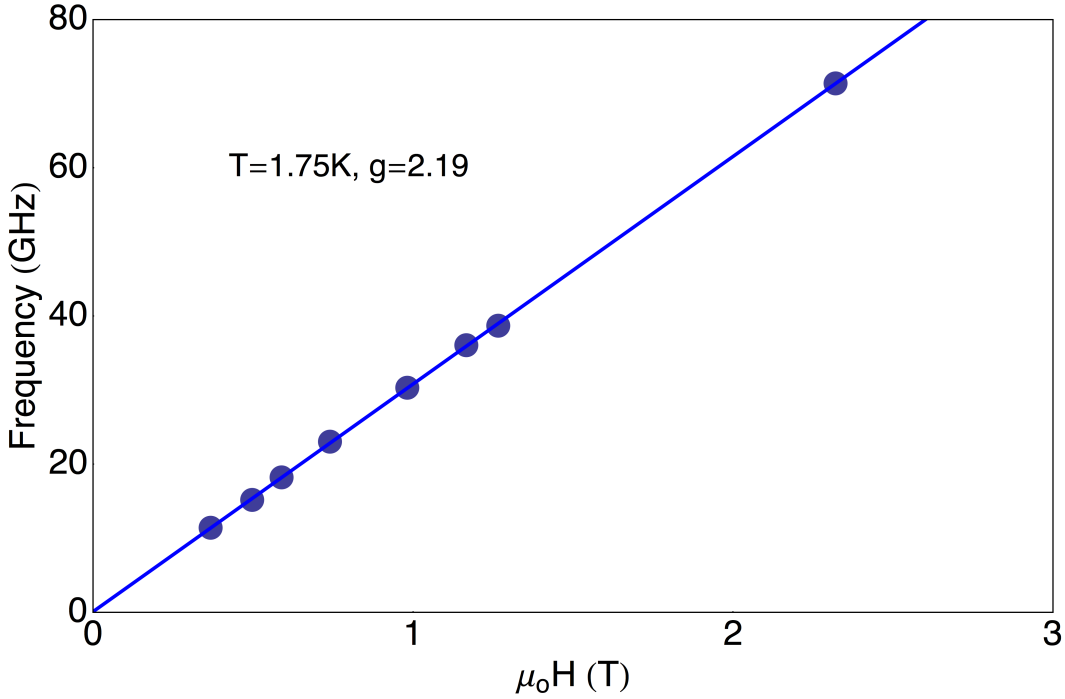


FIGURE 8.5: At a temperature of 1.75 K, frequency-magnetic field scaling determines a  $g$ -factor of 2.19 for magnetic field applied close to the  $\beta$  direction.

Figure 8.6, the  $g$ -factor is 2.19. Temperatures were regulated between 100 K and 1.5 K with no significant change in the  $g$ -factor detected [65]. Angle dependent EPR was measured with a mono-moded ( $\sim 71$  GHz) cavity that can be rotated with respect to the applied magnetic field without thermal cycling [65]. The EPR spectra at a temperature of 4 K for  $360^\circ$  rotation through one crystal plane of  $[\text{Cu}(\text{pyz})(\text{gly})](\text{ClO}_4)$  is shown in Figure 8.6. Each curve is offset vertically for clarity. The angle dependent  $g$ -factor for magnetic fields applied in the  $\beta - \gamma$  plane is shown in Figure 8.7 and is determined by the field at which the absorption occurs  $B$  in Figure 8.6 for each particular angle. The frequency  $\nu$  is  $\sim 71$  GHz.

The EPR absorption was measured for three sets of rotations through high symmetry directions of the crystal to determine the  $g$ -factor anisotropy (Figure 8.8). These measurements identified an approximately uniaxial nature of the  $g$ -tensor

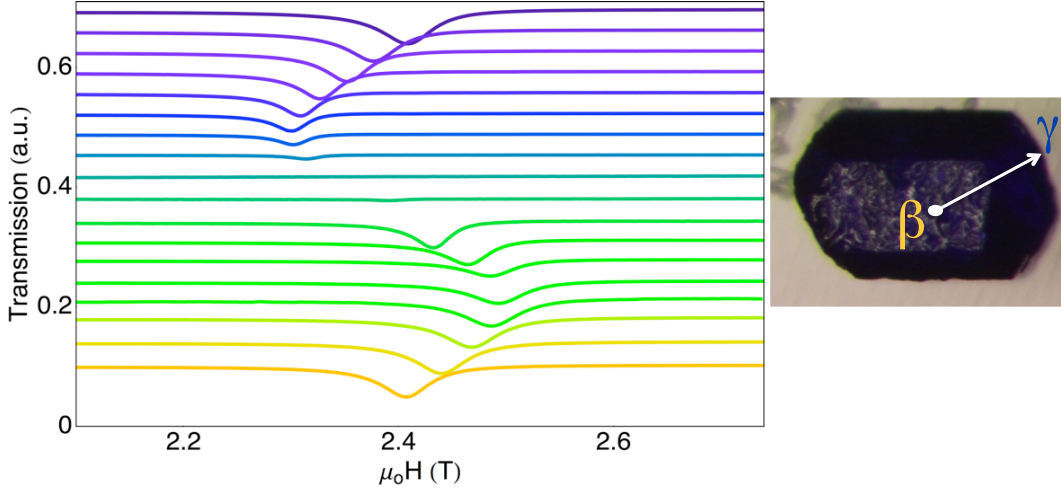


FIGURE 8.6: EPR spectra measured at a frequency of 71 GHz and a temperature of 4 K for different magnetic field orientations in the  $\beta - \gamma$  plane. The maximum  $g$ -factor is observed along the  $[-1, -1, 1]$  ( $\gamma$ ) direction.

and its principle axis, which is parallel to the  $[-1, -1, 1]$  direction ( $\gamma$ ) [65]. At temperatures greater than the exchange interaction energy scales, the EPR spectrum ( $g$ -tensor and number of lines) is dictated by the Cu environment [65]. The crystal plane exhibiting the largest  $g$ -factor anisotropy ( $\beta - \gamma$ ) indicates the direction of the Jahn-Teller distortion of the Cu octahedral environment [65]. At all measured temperatures, only a single EPR line is observed, indicating a common orbital orientation for all dimers [65]. The  $g$ -factor anisotropy ranges from approximately 2.05 to 2.22, typical of other Cu-based molecular magnets [65, 72].

With magnetic field applied perpendicular to the  $\gamma$  direction, the  $g$ -factor was measured as a function of temperature (Figure 8.9). A shift in the effective  $g$ -factor is observed at the antiferromagnetic ordering temperature at  $\sim 1.3$  K (Figure 8.4). The EPR intensity was also studied as a function of temperature at two different frequencies (11 GHz and 36 GHz). The intensity is taken as the area from a

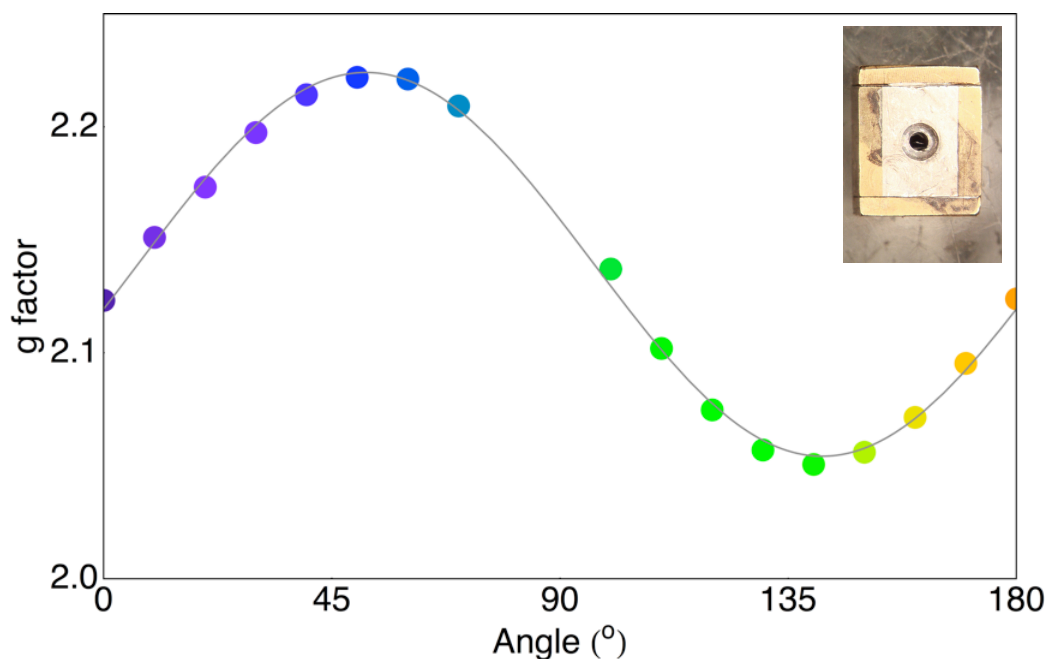


FIGURE 8.7: The angle dependence of the  $g$ -factor of  $[\text{Cu}(\text{pyz})(\text{gly})](\text{ClO}_4)$  for magnetic field applied at several angles in the  $\beta - \gamma$  plane (inset of Figure 8.6).

Lorentzian fit to the absorption lines at each frequency (blue and green data points in Figure 8.10). The behavior at both frequencies is quite similar. At very low temperatures, absorption is frozen out because the triplet states are not thermally populated and only inter-triplet excitations are allowed. A peak in the intensity occurs at a temperature of  $\sim 5\text{K}$ , which coincides with the energy at which the triplon density of states peaks.

A comparison of the thermal excitation gap  $\Delta_1$  to the energy at the top  $J + \frac{J'}{2}$  and bottom  $J - \frac{J'}{2}$  of the magnon bands indicates whether the dispersion is maximum or minimum at the Brillouin zone center. The temperature dependence of the EPR intensity can be modeled for isolated dimers of antiferromagnetically coupled spins

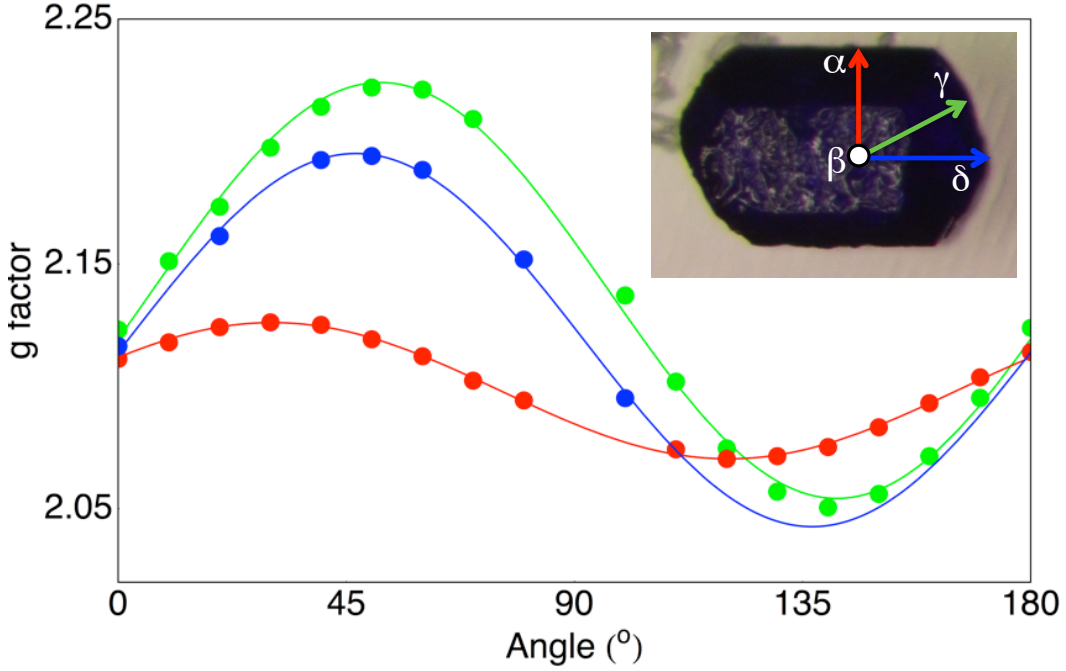


FIGURE 8.8: The angle dependence of the  $g$ -factor for three sets of rotations through high symmetry crystal faces. The color coding of the arrows in the inset indicates the relative anisotropic  $g$ -factor measured in those planes.

described by the Hamiltonian

$$\mathcal{H} = \sum_{ij} J_{ij} s_i s_j - g\mu_B \sum_i B_i s_i. \quad (8.6)$$

The energy spectrum for isolated dimers with  $g = 2.2$  (constrained by the frequency-field scaling) and singlet-triplet gaps given by the intra-dimer couplings  $\Delta_1 = J - \frac{J'}{2} = g\mu_B H_{c1} = 2.8$  K and  $\Delta_2 = J + \frac{J'}{2} = g\mu_B H_{c2} = 8.9$  K (constrained by  $H_{c1}$  and  $H_{c2}$  of the phase diagram) are calculated as a function of magnetic field in the inset of the Figure 8.10. The red and blue lines are the energy spectrum corresponding to the 2.8 K and 8.9 K zero-field gaps, respectively. The temperature dependence of the EPR intensity depends upon the number of particles occupying

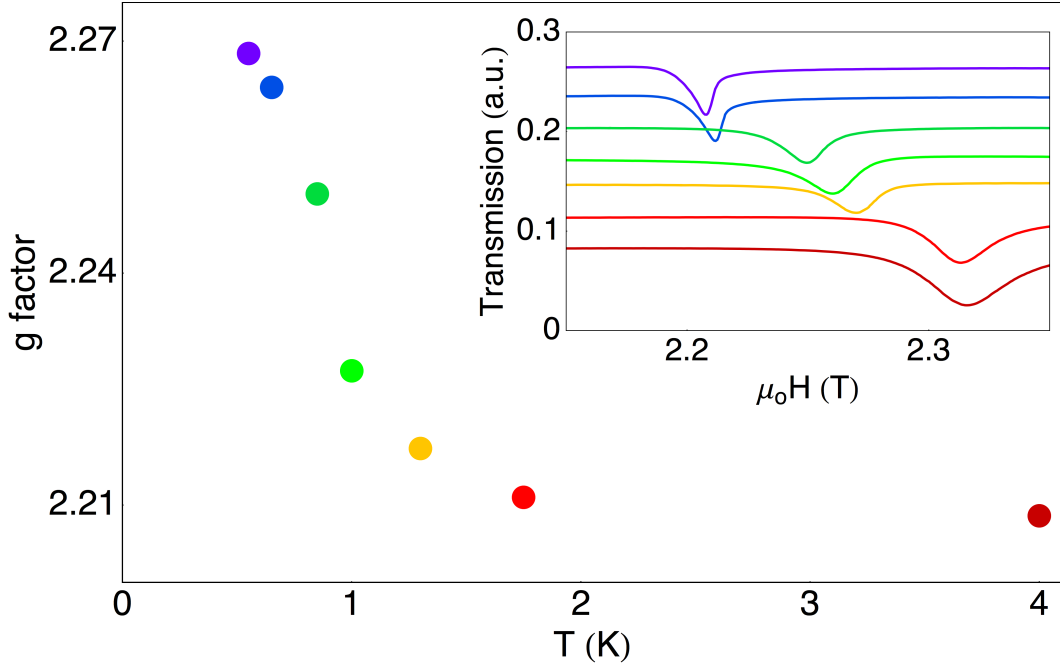


FIGURE 8.9: The  $g$ -factor plotted as a function of temperature with magnetic field applied perpendicular to the  $[-1, -1, 1]$  direction ( $\gamma$ ). An increase in the effective  $g$ -factor is observed at a temperature that coincides with the antiferromagnetic ordering temperature (Figure 8.4).

each state  $N_i$ , which is given by the boltzmann distribution

$$\frac{N_i}{N} = \frac{e^{-E_i/k_B T}}{\sum_i e^{-E_i/k_B T}}. \quad (8.7)$$

The energy of each state, dependent upon the frequency used (fixed field  $B = h\nu/g\mu_B$ ), is given by

$$\begin{aligned} E_1 &= 0 \\ E_2 &= J - g\mu_b B \\ E_3 &= J \\ E_4 &= J + g\mu_b B, \end{aligned} \quad (8.8)$$

where  $J$  can be one of two values depending upon the critical field taken ( $H_{c1}$  or  $H_{c2}$ ). The ground state singlet is  $E_1$  and the triplets  $s^z=+1$ ,  $s^z=0$ ,  $s^z=-1$  are represented by  $E_2$ ,  $E_3$  and  $E_4$ , respectively. Only inter-triplet transitions with  $\Delta s^z = \pm 1$  contribute to the EPR absorption. The absorption due to transitions made between  $E_2$  and  $E_3$  is equal to

$$I_{23} = N_2 * (1 - N_3) - N_3 * (1 - N_2) \quad (8.9)$$

and similarly for transitions between  $E_3$  and  $E_4$ ,

$$I_{34} = N_3 * (1 - N_4) - N_4 * (1 - N_3). \quad (8.10)$$

By recalling Fermi's golden rule  $I_{\text{total}} = I_{23} + I_{34}$ , the EPR intensity can be plotted as a function of temperature for each value of the single-triplet gap  $J$  and for each frequency. The red curves in Figure 8.10 show the calculated intensity for a 2.8 K zero-field singlet-triplet gap, corresponding to  $H_{c1}$ . However, the observed EPR intensity (data points) show best agreement with the calculated intensity (blue and green curves) for an 8.9 K gap corresponding to  $H_{c2}$ .

The temperature dependence of the EPR intensity in the isolated dimer model reflects the magnitude of the singlet-triplet splitting arising from the intra-dimer exchange coupling ( $J$  in Figure 8.2). Because the thermal evolution of the intensity is well-reproduced by the upper critical field  $H_{c2}$ , the coupling  $J = g\mu_B B$  is estimated as 8.9 K. The dispersing  $s^z = +1$  state, evident by the field range over which magnetization is induced between  $H_{c1}$  and  $H_{c2}$ , is due to the inter-dimer coupling  $J'$ . The magnitude of this coupling can be approximated in terms of a microscopic mean-field model, where  $g\mu_B H_{c1} = |J| - \alpha |J'|/2$ .  $\alpha$  describes the number of interacting nearest neighbors linked with a mean-field ferromagnetic inter-dimer exchange constant and is assumed to be 4 in this model [65].  $g\mu_B H_{c1}$

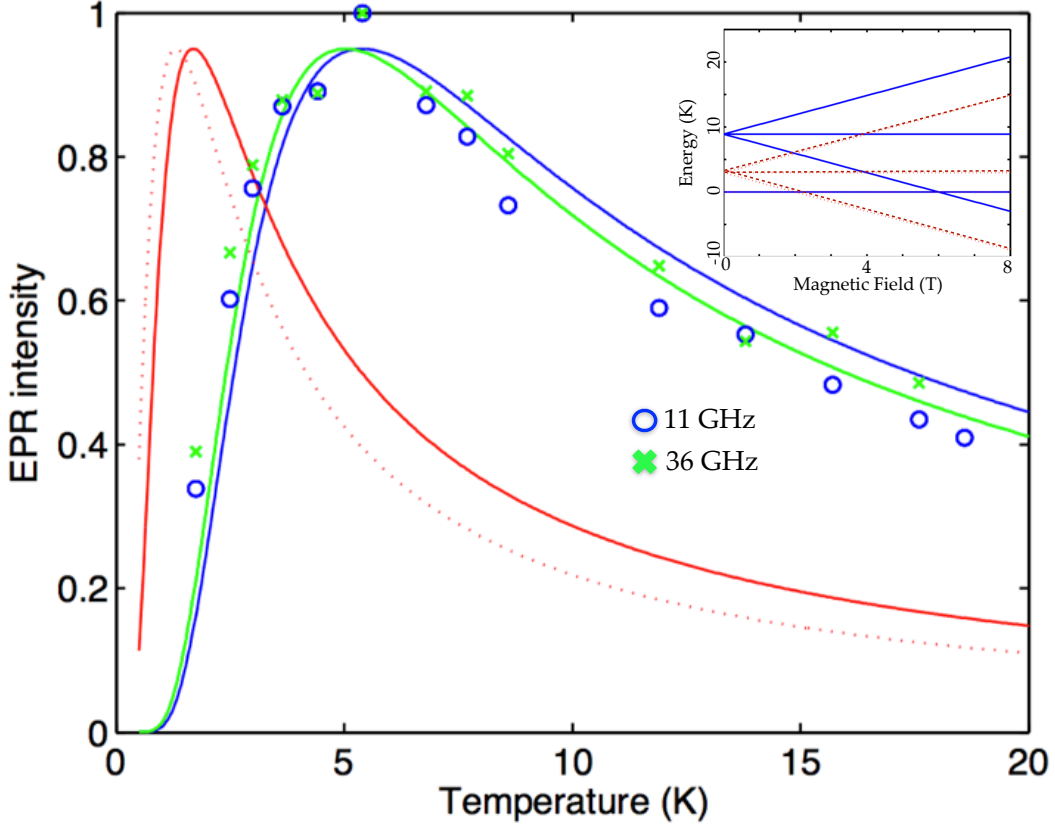


FIGURE 8.10: The temperature dependence of the EPR intensity extracted from Lorentzian fits to the absorption lines measured at 11 GHz (blue circles) and 36 GHz (green crosses). Boltzmann thermal population fits for each frequency with the singlet-triplet gaps constrained by the observed  $g$ -factor and critical magnetic fields.

$= 2.8$  K leads to a significant and ferromagnetic inter-dimer exchange  $J' \sim 3$  K. Furthermore, the EPR intensity is due to allowable  $\Delta \mathbf{k} = 0$  (momentum wavevector unchanged) transitions between the  $s^z = \pm 1$  states and a dispersionless  $s^z = 0$  state, suggesting that the magnon dispersion arising from inter-dimer exchange coupling must be maximum at the zone center [65].

$[\text{Cu}(\text{pyz})(\text{gly})](\text{ClO}_4)$  is an example of a gapped system, where the ground state singlet is a result of magnetic correlations which decay exponentially after some

finite distance. In such case, the energy levels are quantized and a disordered state is observed at zero temperature, which is a result of the low dimensionality of the system and not due to magnetic frustration. With pressure, the exchange couplings could be tuned towards a quantum critical point, where the lower critical field  $H_{c1}$  can be driven to zero magnetic field with increased inter-dimer exchange coupling. This would require accessible pressures and susceptibility could be measured simultaneously using the PDO circuit to observe quantum critical behavior.



where  $\mathbf{1}, \mathbf{2}$  is used to distinguish the two particles. To determine the Coulomb interaction of two particles occupying  $\Gamma_7$ , matrix elements  $a, b$  and  $d$  must be defined via two-particle orbital integrals (discussed in more detail in regards to Equation 2.15)

$$\int d\mathbf{1}d\mathbf{2} \eta_{\alpha}^{\dagger}(\mathbf{1})\eta_{\beta}^{\dagger}(\mathbf{2})V_{coul}(\mathbf{1}-\mathbf{2})\eta_{\gamma}(\mathbf{1})\eta_{\delta}(\mathbf{2}) \quad (\text{A.3})$$

where  $\mathbf{1}$  and  $\mathbf{2}$  represent the position of first and second electron respectively. In a cubic environment, only three integrals are non-zero. Indeed, the “density matrix”  $\rho_{\alpha,\beta} = \eta_{\alpha}^{\dagger}(\mathbf{1})\eta_{\beta}(\mathbf{1})$  can be decomposed into three components transforming under irreducible representations of the cubic group,

$$\begin{aligned} \rho_{\Gamma^1} &= \rho_{x,x} + \rho_{y,y} + \rho_{z,z} \\ \rho_{\Gamma^3} &= \rho_{x,x} - \rho_{y,y}, \quad 2\rho_{z,z} - \rho_{x,x} - \rho_{y,y} \\ \rho_{\Gamma^5} &= \rho_{x,y}, \quad \rho_{y,z}, \quad \rho_{z,x} \end{aligned} \quad (\text{A.4})$$

Since  $V_{coul}(\mathbf{1}-\mathbf{2})$  is fully rotationally symmetric, only matrix elements between  $\rho$  in the same representation are non-zero. A possible choice of three non-zero matrix elements is

$$\begin{aligned} a &= \int d\mathbf{1}d\mathbf{2} \rho_{x,x}^{\dagger}(\mathbf{1})V_{coul}(\mathbf{1}-\mathbf{2})\rho_{x,x}(\mathbf{2}) \\ b &= \int d\mathbf{1}d\mathbf{2} \rho_{x,x}^{\dagger}(\mathbf{1})V_{coul}(\mathbf{1}-\mathbf{2})\rho_{y,y}(\mathbf{2}) \\ d &= \int d\mathbf{1}d\mathbf{2} \rho_{x,y}^{\dagger}(\mathbf{1})V_{coul}(\mathbf{1}-\mathbf{2})\rho_{x,y}(\mathbf{2}) \end{aligned} \quad (\text{A.5})$$

Using the antisymmetrized product of the  $\Gamma_7$  states defined above, the Coulomb interaction between four electrons (two holes) shifts the energy by

$$\left\langle \begin{array}{c} \equiv \\ \equiv \\ \uparrow \downarrow \end{array} \middle| V_{Coul} \middle| \begin{array}{c} \equiv \\ \equiv \\ \uparrow \downarrow \end{array} \right\rangle = \frac{2a}{3} + \frac{4b}{3} \quad (\text{A.6})$$

When Coulomb repulsion is strong enough, the lowest energy state may be one electron occupying the  $\Gamma_7$  multiplet and one occupying  $\Gamma_8$  because such a two-particle state will have lower Coulomb repulsion. The 8 possible states originating from  $\Gamma_7 \times \Gamma_8$  split into three multiplets (a doublet and two triplets) according to

$$\Gamma_7 \times \Gamma_8 = \Gamma_3 + \Gamma_4 + \Gamma_5 \quad (\text{A.7})$$

In the presence of the Coulomb interaction, the condition for any of these states to be the ground state of the iridium  $d^4$  atom in an orthorhombic environment, is found using the distinct matrix elements defined above. The two-particle wavefunctions transforming under  $\Gamma_3$ ,  $\Gamma_4$ , and  $\Gamma_5$  are determined by group theory via the Clebsch-Gordan coefficients (just as the  $\Gamma_7$  and  $\Gamma_8$  wavefunctions were found in Chapter 3) for the product  $\Gamma_7 \times \Gamma_8$

$$\begin{aligned} |\Gamma^3\rangle_2 &= \sqrt{\frac{1}{2}} \begin{array}{|c|} \hline \bullet \\ \hline \hline \hline \hline \hline \\ \hline \end{array} + \sqrt{\frac{1}{2}} \begin{array}{|c|} \hline \hline \hline \hline \hline \hline \\ \hline \bullet \\ \hline \end{array} \\ |\Gamma^3\rangle_1 &= -\sqrt{\frac{1}{2}} \begin{array}{|c|} \hline \bullet \\ \hline \hline \hline \hline \hline \\ \hline \end{array} - \sqrt{\frac{1}{2}} \begin{array}{|c|} \hline \hline \hline \hline \hline \hline \\ \hline \bullet \\ \hline \end{array} \end{aligned} \quad (\text{A.8})$$

$$\begin{aligned} |\Gamma^4\rangle_3 &= i\sqrt{\frac{1}{2}} \begin{array}{|c|} \hline \bullet \\ \hline \hline \hline \hline \hline \\ \hline \end{array} - i\sqrt{\frac{1}{2}} \begin{array}{|c|} \hline \hline \hline \hline \hline \hline \\ \hline \bullet \\ \hline \end{array} \\ |\Gamma^4\rangle_2 &= \sqrt{\frac{3}{8}} \begin{array}{|c|} \hline \bullet \\ \hline \hline \hline \hline \hline \\ \hline \end{array} - \sqrt{\frac{1}{8}} \begin{array}{|c|} \hline \hline \hline \hline \hline \hline \\ \hline \bullet \\ \hline \end{array} + \sqrt{\frac{1}{8}} \begin{array}{|c|} \hline \bullet \\ \hline \hline \hline \hline \hline \\ \hline \end{array} - \sqrt{\frac{3}{8}} \begin{array}{|c|} \hline \hline \hline \hline \hline \hline \\ \hline \bullet \\ \hline \end{array} \\ |\Gamma^4\rangle_1 &= -i\sqrt{\frac{3}{8}} \begin{array}{|c|} \hline \bullet \\ \hline \hline \hline \hline \hline \\ \hline \end{array} - i\sqrt{\frac{1}{8}} \begin{array}{|c|} \hline \hline \hline \hline \hline \hline \\ \hline \bullet \\ \hline \end{array} - i\sqrt{\frac{1}{8}} \begin{array}{|c|} \hline \bullet \\ \hline \hline \hline \hline \hline \\ \hline \end{array} - i\sqrt{\frac{3}{8}} \begin{array}{|c|} \hline \hline \hline \hline \hline \hline \\ \hline \bullet \\ \hline \end{array} \end{aligned} \quad (\text{A.9})$$

$$\begin{aligned} |\Gamma^5\rangle_3 &= i\sqrt{\frac{1}{2}} \begin{array}{|c|} \hline \bullet \\ \hline \hline \hline \hline \hline \\ \hline \end{array} - i\sqrt{\frac{1}{2}} \begin{array}{|c|} \hline \hline \hline \hline \hline \hline \\ \hline \bullet \\ \hline \end{array} \\ |\Gamma^5\rangle_2 &= -\sqrt{\frac{1}{8}} \begin{array}{|c|} \hline \bullet \\ \hline \hline \hline \hline \hline \\ \hline \end{array} - \sqrt{\frac{3}{8}} \begin{array}{|c|} \hline \hline \hline \hline \hline \hline \\ \hline \bullet \\ \hline \end{array} + \sqrt{\frac{3}{8}} \begin{array}{|c|} \hline \bullet \\ \hline \hline \hline \hline \hline \\ \hline \end{array} + \sqrt{\frac{1}{8}} \begin{array}{|c|} \hline \hline \hline \hline \hline \hline \\ \hline \bullet \\ \hline \end{array} \\ |\Gamma^5\rangle_1 &= -i\sqrt{\frac{1}{8}} \begin{array}{|c|} \hline \bullet \\ \hline \hline \hline \hline \hline \\ \hline \end{array} + i\sqrt{\frac{3}{8}} \begin{array}{|c|} \hline \hline \hline \hline \hline \hline \\ \hline \bullet \\ \hline \end{array} + i\sqrt{\frac{3}{8}} \begin{array}{|c|} \hline \bullet \\ \hline \hline \hline \hline \hline \\ \hline \end{array} - i\sqrt{\frac{1}{8}} \begin{array}{|c|} \hline \hline \hline \hline \hline \hline \\ \hline \bullet \\ \hline \end{array} \end{aligned} \quad (\text{A.10})$$

The Coulomb interaction of energy shift for each multiplet is found

$$\begin{aligned}
 \langle \Gamma^3 | V_{Coul} | \Gamma^3 \rangle &= \frac{4a}{3} + \frac{2}{3}(b-d) - \frac{4}{3}d \\
 \langle \Gamma^5 | V_{Coul} | \Gamma^5 \rangle &= 2(b-d) + \frac{8d}{3} \\
 \langle \Gamma^4 | V_{Coul} | \Gamma^4 \rangle &= 2(b-d)
 \end{aligned} \tag{A.11}$$

It is generally true that  $a \gg b$  and  $a \gg d$  and that all three matrix elements are positive  $a, b, d > 0$ , suggesting that among the three multiplets  $\Gamma^4$  has the lowest Coulomb repulsion energy. In order for this state to be the true ground state of the  $d^4$  electron configuration of iridium, its energy must be lower than the energy of the two electrons on the  $\Gamma^7$  multiplet (Equation A.6). The inequality

$$\frac{2a + 4b}{3} > \frac{3}{2}\lambda_{SO} + 2(b-d) \tag{A.12}$$

will be satisfied if the largest Coulomb repulsion matrix element  $a$  is larger than spin-orbit splitting. It can be concluded that an iridium ion in the  $d^4$  state in a cubic environment will likely have a three-fold degenerate  $\Gamma^4$  multiplet, transforming as spin 1, as its ground state. Similar analysis can be carried on for two holes on  $\Gamma^8$  which form two-particle states according to  $\Gamma_8 \times \Gamma_8 = \Gamma^1 + \Gamma^3 + \Gamma^5$ .

## B

### One Electron on the Ir $d$ -shell in Empty Space

In Chapter 3, the wavefunctions of the  $\Gamma_7$  and  $\Gamma_8$  multiplets were found by first applying a cubic environment to the  $d^5$  configuration of Ir and then introducing the spin-orbit interaction. To check this result, a single electron can be considered on the  $d$  shell starting from empty space. One electron on the  $d$ -shell in a rotationally invariant space splits into two multiplets; a quadruplet

$$\begin{aligned} \left| +\frac{3}{2} \right\rangle_{\frac{3}{2}} &= -\sqrt{\frac{1}{5}} |1 \uparrow\rangle + \sqrt{\frac{4}{5}} |2 \downarrow\rangle \\ \left| +\frac{1}{2} \right\rangle_{\frac{3}{2}} &= -\sqrt{\frac{2}{5}} |0 \uparrow\rangle + \sqrt{\frac{3}{5}} |1 \downarrow\rangle \\ \left| -\frac{1}{2} \right\rangle_{\frac{3}{2}} &= \sqrt{\frac{2}{5}} |0 \downarrow\rangle - \sqrt{\frac{3}{5}} |-1 \uparrow\rangle \\ \left| -\frac{3}{2} \right\rangle_{\frac{3}{2}} &= \sqrt{\frac{1}{5}} |-1 \downarrow\rangle - \sqrt{\frac{4}{5}} |-2 \uparrow\rangle \end{aligned} \tag{B.1}$$

and a sextuplet

$$\begin{aligned}
 \left| +\frac{5}{2} \right\rangle_{\frac{5}{2}} &= |2 \uparrow\rangle \\
 \left| +\frac{3}{2} \right\rangle_{\frac{5}{2}} &= \sqrt{\frac{4}{5}} |1 \uparrow\rangle + \sqrt{\frac{1}{5}} |2 \downarrow\rangle \\
 \left| +\frac{1}{2} \right\rangle_{\frac{5}{2}} &= \sqrt{\frac{3}{5}} |0 \uparrow\rangle + \sqrt{\frac{2}{5}} |1 \downarrow\rangle \\
 \left| -\frac{1}{2} \right\rangle_{\frac{5}{2}} &= \sqrt{\frac{3}{5}} |0 \downarrow\rangle + \sqrt{\frac{2}{5}} |-1 \uparrow\rangle \\
 \left| -\frac{3}{2} \right\rangle_{\frac{5}{2}} &= \sqrt{\frac{4}{5}} |-1 \downarrow\rangle + \sqrt{\frac{1}{5}} |-2 \uparrow\rangle \\
 \left| -\frac{5}{2} \right\rangle_{\frac{5}{2}} &= |-2 \downarrow\rangle
 \end{aligned} \tag{B.2}$$

Spin-orbit interaction causes the 3/2 multiplet to be lower in energy than the 5/2 multiplet. In an octahedral crystal field, the 3/2 multiplet does not split further and becomes  $\Gamma_8$ . The wavefunctions, which were obtained straightforwardly from the Clebsch Gordan coefficients, are exactly those of Equation B.1 but are now referred to as  $\Gamma_8(a)$

$$\begin{aligned}
 \left| +\frac{3}{2} \right\rangle_{\Gamma_8(a)} &= -\sqrt{\frac{1}{5}} |1 \uparrow\rangle + \sqrt{\frac{4}{5}} |2 \downarrow\rangle \\
 \left| +\frac{1}{2} \right\rangle_{\Gamma_8(a)} &= -\sqrt{\frac{2}{5}} |0 \uparrow\rangle + \sqrt{\frac{3}{5}} |1 \downarrow\rangle \\
 \left| -\frac{1}{2} \right\rangle_{\Gamma_8(a)} &= \sqrt{\frac{2}{5}} |0 \downarrow\rangle - \sqrt{\frac{3}{5}} |-1 \uparrow\rangle \\
 \left| -\frac{3}{2} \right\rangle_{\Gamma_8(a)} &= \sqrt{\frac{1}{5}} |-1 \downarrow\rangle - \sqrt{\frac{4}{5}} |-2 \uparrow\rangle
 \end{aligned} \tag{B.3}$$

The  $5/2$  multiplet splits into a doublet  $\Gamma_7$  and a quadruplet  $\Gamma_8$ , which can be written in terms of the half-integral states defined above [53].

$$\begin{aligned}
 \left|+\frac{1}{2}\right\rangle_{\Gamma_7} &= \sqrt{\frac{1}{6}} \left|\frac{5}{2}\right\rangle_{\frac{5}{2}} - \sqrt{\frac{5}{6}} \left|-\frac{3}{2}\right\rangle_{\frac{5}{2}} \\
 \left|-\frac{1}{2}\right\rangle_{\Gamma_7} &= \sqrt{\frac{1}{6}} \left|-\frac{5}{2}\right\rangle_{\frac{5}{2}} - \sqrt{\frac{5}{6}} \left|+\frac{3}{2}\right\rangle_{\frac{5}{2}} \\
 \\ 
 \left|+\frac{3}{2}\right\rangle_{\Gamma_8(b)} &= -\sqrt{\frac{1}{6}} \left|\frac{3}{2}\right\rangle_{\frac{5}{2}} - \sqrt{\frac{5}{6}} \left|-\frac{5}{2}\right\rangle_{\frac{5}{2}} \\
 \left|+\frac{1}{2}\right\rangle_{\Gamma_8(b)} &= \left|\frac{1}{2}\right\rangle_{\frac{5}{2}} \\
 \left|-\frac{1}{2}\right\rangle_{\Gamma_8(b)} &= -\left|-\frac{1}{2}\right\rangle_{\frac{5}{2}} \\
 \left|-\frac{3}{2}\right\rangle_{\Gamma_8(b)} &= \sqrt{\frac{1}{6}} \left|-\frac{3}{2}\right\rangle_{\frac{5}{2}} + \sqrt{\frac{5}{6}} \left|+\frac{5}{2}\right\rangle_{\frac{5}{2}}
 \end{aligned} \tag{B.4}$$

The letters  $a$  and  $b$  are used to distinguish between the two different  $\Gamma_8$  states which result from the cubic environment. Substituting Equations B.1 and B.2 into Equation B.4 and using the following definition

$$\begin{aligned}
 |2_+\rangle &= |2\rangle + |-2\rangle \\
 |2_-\rangle &= |2\rangle - |-2\rangle
 \end{aligned} \tag{B.5}$$

and the identity,

$$ax + by = \frac{a+b}{2}(x+y) + \frac{a-b}{2}(x-y) \tag{B.6}$$

the  $\Gamma_7$  and  $\Gamma_8(b)$  states can be rewritten as

$$\begin{aligned}
 \left| +\frac{1}{2} \right\rangle_{\Gamma_7} &= -\sqrt{\frac{4}{6}} | -1 \downarrow \rangle + \sqrt{\frac{2}{6}} \frac{| 2_- \uparrow \rangle}{\sqrt{2}} \\
 \left| -\frac{1}{2} \right\rangle_{\Gamma_7} &= -\sqrt{\frac{4}{6}} | 1 \uparrow \rangle - \sqrt{\frac{2}{6}} \frac{| 2_- \downarrow \rangle}{\sqrt{2}} \\
 \\
 \left| +\frac{3}{2} \right\rangle_{\Gamma_8(b)} &= -\sqrt{\frac{2}{3 \cdot 5}} | 1 \uparrow \rangle - \sqrt{\frac{3}{2 \cdot 5}} | 2_+ \downarrow \rangle + \sqrt{\frac{2}{3 \cdot 5}} | 2_- \downarrow \rangle \\
 \left| +\frac{1}{2} \right\rangle_{\Gamma_8(b)} &= \sqrt{\frac{2}{5}} | 1 \downarrow \rangle + \sqrt{\frac{3}{5}} | 0 \uparrow \rangle \\
 \left| -\frac{1}{2} \right\rangle_{\Gamma_8(b)} &= -\sqrt{\frac{2}{5}} | -1 \uparrow \rangle - \sqrt{\frac{3}{5}} | 0 \downarrow \rangle \\
 \left| -\frac{3}{2} \right\rangle_{\Gamma_8(b)} &= \sqrt{\frac{2}{3 \cdot 5}} | -1 \downarrow \rangle + \sqrt{\frac{3}{2 \cdot 5}} | 2_+ \uparrow \rangle + \sqrt{\frac{2}{3 \cdot 5}} | 2_- \uparrow \rangle
 \end{aligned} \tag{B.7}$$

These wavefunctions for the 10 single electron states (one  $\Gamma_7$  and 2  $\Gamma_8$  multiplets) were found by starting with a single electron on the  $d$ -shell in empty space and then introducing the cubic environment. In Chapter 3, the same three multiplets were found by starting with the  $d$ -orbital in a cubic environment and then adding the spin-orbit interaction. Both the crystal field splitting and the spin-orbit interaction are crystallographic scalars, making it impossible for states in different representations of the cubic group to mix. Thus, the  $\Gamma_7$  states can be identified unambiguously as those which resulted from the direct product of  $\Gamma_5$  and  $\Gamma_6$  (Chapter 3) because they cannot mix with the states in  $\Gamma_8$ . However, mixing of two inequivalent  $\Gamma_8$  multiplets is not constrained by symmetry in any way. As a consequence, the  $\Gamma_8$  multiplets are not defined uniquely and actually both  $\Gamma_8$  multiplets contain an admixture of the  $\Gamma_3$  multiplet, which is high in energy in the iridium crystal field. This confirms that the  $\Gamma_7$  multiplet is lower in energy than

$\Gamma_{8(b)}$ . There is a unique linear superposition of  $\Gamma_{8(a)}$  and  $\Gamma_{8(b)}$  that has support only in the  $\Gamma_5$  multiplet.

$$\sqrt{\frac{3}{5}}\Gamma_{8(a)} + \sqrt{\frac{2}{5}}\Gamma_{8(b)} \quad (\text{B.8})$$

The  $\Gamma_7$  and  $\Gamma_8$  multiplets below are the states that arise when considering spin-orbit on the orbital  $\Gamma_5$  triplet (apart from a factor of i)

$$\begin{aligned} \left| +\frac{1}{2} \right\rangle_{\Gamma_7} &= -\sqrt{\frac{2}{3}}|-1 \downarrow\rangle + \sqrt{\frac{1}{6}}|2_- \uparrow\rangle \\ \left| -\frac{1}{2} \right\rangle_{\Gamma_7} &= -\sqrt{\frac{2}{3}}|1 \uparrow\rangle - \sqrt{\frac{1}{6}}|2_- \downarrow\rangle \end{aligned}$$

$$\begin{aligned} \left| +\frac{3}{2} \right\rangle_{\Gamma_8} &= -\sqrt{\frac{1}{3}}|1 \uparrow\rangle + \sqrt{\frac{1}{3}}|2_- \downarrow\rangle \\ \left| +\frac{1}{2} \right\rangle_{\Gamma_8} &= |1 \downarrow\rangle \\ \left| -\frac{1}{2} \right\rangle_{\Gamma_8} &= -|-1 \uparrow\rangle \\ \left| -\frac{3}{2} \right\rangle_{\Gamma_8} &= \sqrt{\frac{1}{3}}|-1 \downarrow\rangle + \sqrt{\frac{1}{3}}|2_- \uparrow\rangle \end{aligned}$$

(B.9)

## Bibliography

- [1] W. Witczak-Krempa, G. Chen, Y. B. Kim, and L. Balents. Correlated quantum phenomena in the strong spin-orbit regime. *Annu. Rev. Condens. Matter Phys.*, 5(57), 2014.
- [2] D. Shoenberg. *Magnetic oscillations in metals*. Cambridge University Press, 1984.
- [3] J. H. de Boer and E. J. W. Verwey. Semi-conductors with partially and with completely filled 3d-lattice bands. *Proc. Phys. Soc.*, 49 (4S)(59), 1937.
- [4] N. F. Mott. The basis of the electron theory of metals, with special reference to the transition metals. *Proc. Phys. Soc.*, 62(7), 1949.
- [5] J.R. Schrieffer J. Bardeen, L.N. Cooper. Theory of superconductivity. *Phys. Rev.*, 108(5), 1957.
- [6] R.B. Laughlin. Anomalous quantum Hall effect: An incompressible quantum fluid with fractionally charged excitations. *Phys. Rev. Lett.*, 50(18), 1983.
- [7] V.J. Goldman and B. Su. Resonant tunneling in the quantum Hall regime: Measurement of fractional charge. *Science*, 267(5200), 1995.

- [8] R. de Picciotto, M. Reznikov, M. Heiblum, V. Umansky, G. Bunin, and D. Mahalu. Direct observation of a fractional charge. *Nature*, 389(6647), 1997.
- [9] X.G. Wen and Q. Niu. Ground state degeneracy of the FQH states in presence of random potential and on high genus Riemann surfaces. *Phys. Rev. B*, 41(9377), 1990.
- [10] Markus König, Steffen Wiedmann, Christoph Brune, Andreas Roth, Hartmut Buhmann, Laurens W. Molenkamp, Xiao-Liang Qi, and Shou-Cheng Zhang. Quantum spin hall insulator state in HgTe quantum wells. *Science*, 318(5851): 766–770, 2007.
- [11] L. Wray, Y. Xia, Y.S. Hor, R.J. Cava, M.Z. Hasan, D. Hsieh, D. Qian. A topological Dirac insulator in a quantum spin Hall phase. *Nature*, 452(06843), 2008.
- [12] Dmytro Pesin and Leon Balents. Mott physics and band topology in materials with strong spin-orbit interaction. *Nature Physics*, 6(1606):376–381, 2010.
- [13] Maxim Dzero, Kai Sun, Victor Galitski, and Piers Coleman. Topological kondo insulators. *Phys. Rev. Lett.*, 104(106408), 2010.
- [14] Takafumi Suzuki, Takuto Yamada, Youhei Yamaji, and Suga Sei-ichiro. Dynamical properties of honeycomb-lattice iridates  $\text{Na}_2\text{IrO}_3$ . Arxiv.org, July 2015. URL <http://arxiv.org/abs/1507.06044>.
- [15] Ionnis Rousochatzakis, Johannes Reuther, Ronny Thomale, Stephan Rachel, and N. B. Perkins. Phase diagram and quantum order by disorder in the Kitaev K1-K2 honeycomb magnet. Arxiv.org, June 2015. URL <http://arxiv.org/abs/1506.09185>.

- [16] Eric Kin-Ho Lee, Jeffrey G. Rau, and Yong Baek Kim. Two iridates, two models, two approaches: a comparative study on magnetism in 3D honeycomb materials. Arxiv.org, June 2015. URL <http://arxiv.org/abs/1506.06746>.
- [17] Kaige Hu, Fa Wang, and Ji Feng. Computational study of the magnetic structure of  $\text{Na}_2\text{IrO}_3$ . Arxiv.org, April 2015. URL <http://arxiv.org/abs/1504.02699>.
- [18] Jiri Chaloupka and Giniyat Khaliullin. Hidden symmetries of the extended Kitaev-Heisenberg model: Implications for honeycomb lattice iridates  $\text{A}_2\text{IrO}_3$ . *Phys. Rev. B*, 92(024413), 2015.
- [19] Yuriy Sizyuk, Craig Price, Peter Wolffe, and Natalia B. Perkins. Importance of anisotropic exchange interactions in honeycomb iridates. minimal model for zigzag antiferromagnetic order in  $\text{Na}_2\text{IrO}_3$ . *Phys. Rev. B*, 90(155126), 2014.
- [20] Itamar Kimchi, Radu Coldea, and Ashvin Vishwanath. Unified theory of spiral magnetism in the harmonic-honeycomb iridates  $\alpha, \beta, \gamma \text{Li}_2\text{IrO}_3$ . *Phys. Rev. B*, 91(245134), 2015.
- [21] Eric Kin-Ho Lee and Yong Baek Kim. Theory of magnetic phase diagrams in hyperhoneycomb and harmonic-honeycomb iridates. *Phys. Rev. B*, 91(064407), 2015.
- [22] R. D. Johnson, S. Williams, A. A. Haghighirad, J. Singleton, V. Zapf, P. Manuel, I. I. Mazin, Y. Li, H. O. Jeschke, R. Valenti, and R. Coldea. The monoclinic crystal structure of  $\alpha\text{-RuCl}_3$  and the zigzag antiferromagnetic ground state. Arxiv.org, September 2015. URL <http://arxiv.org/abs/1509.02670>.

- [23] Heung-Sik Kim, V. Vijay Shankar, Andrei Catuneanu, and Hae-Young Kee. Kitaev magnetism in honeycomb  $\text{RuCl}_3$  with intermediate spin-orbit coupling. *Phys. Rev. B*, 91(241110), 2015.
- [24] M. Majumder, M. Schmidt, H. Rosner, A. A. Tsirlin, H. Yasuoka, and M. Baenitz. Anisotropic  $\text{Ru}^{3+} 4d^5$  magnetism in the  $\alpha\text{-RuCl}_3$  honeycomb system: susceptibility, specific heat and zero field NMR. *Phys. Rev. B*, 91(180401), 2015.
- [25] A. Banerjee, C. A. Bridges, J-Q. Yan, A. A. Aczel, L. Li, M. B. Stone, G. E. Granroth, M. D. Lumsden, Y. Yiu, J. Knolle, D. L. Kovrizhin, R. Bhattacharjee, S. Moessner, D. A. Tennant, D. G. Mandrus, and S. E. Nagler. Proximate Kitaev quantum spin liquid behaviour in  $\alpha\text{-RuCl}_3$ . Arxiv.org, April 2015. URL <http://arxiv.org/abs/1504.08037>.
- [26] J. C. Wang, J. Terzic, T. F. Qi, Feng Ye, S. J. Yuan, S. Aswartham, V. Streltsov, D. I. Khomskii, Kaul R. K., and G. Cao. Lattice-tuned magnetism of  $\text{Ru}^{4+}(4d^4)$  ions in single-crystals of the layered honeycomb ruthenates:  $\text{Li}_2\text{RuO}_3$  and  $\text{Na}_2\text{RuO}_3$ . *Phys. Rev. B*, 90(161110), 2014.
- [27] Alexei Kitaev. Anyons in an exactly solved model and beyond. *Annals of Physics*, 321, 2006.
- [28] G. Jackeli and G. Khaliullin. Mott insulators in the strong spin-orbit coupling limit: From Heisenberg to a quantum compass and Kitaev models. *Phys. Rev. Lett.*, 102(017205), 2009.
- [29] George Jackeli Jiri Chaloupka and Giniyat Khaliullin. Kitaev-heisenberg model on a honeycomb lattice: Possible exotic phases in iridium oxides  $\text{A}_2\text{RuO}_3$ . *Phys. Rev. Lett.*, 105(027204), 2010.

- [30] Yogesh Singh, S. Manni, J. Reuther, T. Berlijn, R. Thomale, W. Ku, S. Trebst, and P. Gegenwart. Relevance of the heisenberg-kitaev model for the honeycomb lattice iridates  $\text{A}_2\text{IrO}_3$ . *Phys. Rev. Lett.*, 108(127203), 2012.
- [31] Jiri Chaloupka, George Jackeli, and Giniyat Khaliullin. On the origin of zigzag magnetic order in iridium oxide  $\text{Na}_2\text{IrO}_3$ . *Phys. Rev. Lett.*, 110(097204), 2013.
- [32] A. Biffin, R. D. Johnson, Sungkyun Choi, F. Freund, S. Manni, A. Bombardi, P. Manuel, P. Gegenwart, and R. Coldea. Unconventional magnetic order on the hyperhoneycomb Kitaev lattice in  $\beta\text{-Li}_2\text{IrO}_3$ : Full solution via magnetic resonant x-ray diffraction. *Phys. Rev. B*, 90(205116), 2014.
- [33] A. Biffin, R.D. Johnson, I. Kimchi, R. Morris, A. Bombardi, J.G. Analytis, A. Vishwanath, and R. Coldea. Noncoplanar and counterrotating incommensurate magnetic order stabilized by Kitaev interactions in  $\gamma\text{-Li}_2\text{IrO}_3$ . *Phys. Rev. Lett.*, 113(197201), 2014.
- [34] S.K. Choi, R. Coldea, A.N. Kolmogorov, T. Lancaster, I.I. Mazin, S.J. Blundell, P.G. Radaelli, Yogesh Singh, P. Gegenwart, K.R. Choi, S.W. Cheong, P.J. Baker, C. Stock, and J. Taylor. Spin waves and revised crystal structure of honeycomb iridate  $\text{Na}_2\text{IrO}_3$ . *Phys. Rev. Lett.*, 108(127204), 2012.
- [35] K A Modic, Tess E Smidt, Itamar Kimchi, Nicholas P Breznay, Alun Biffin, Sungkyun Choi, Roger D Johnson, Radu Coldea, Pilanda Watkins-Curry, Gregory T McCandless, Julia Y Chan, Felipe Gandara, Z Islam, Ashvin Vishwanath, Arkady Shekhter, Ross D McDonald, and James G Analytis. Realization of a three-dimensional spin-anisotropic harmonic honeycomb iridate. *Nat. Commun.*, 5(4203), 2014.
- [36] Sae Hwan Chun, Jong-Woo Kim, Jungho Kim, H. Zheng, Constantinos C. Stoumpos, C. D. Malliakas, J. F. Mitchell, Kavita Mehlawat, Yogesh Singh,

- Y. Choi, T. Gog, A. Al-Zein, M. Moretti Sala, M. Krisch, J. Chaloupka, G. Jackeli, G. Khaliullin, and B. J. Kim. Direct evidence for dominant bond-directional interactions in a honeycomb lattice iridate  $\text{Na}_2\text{IrO}_3$ . *Nature Physics*, 11(3322), 2015.
- [37] Heung-Sik Kim, Eric Kin-Ho Lee, and Yong Baek Kim. Predominance of the Kitaev interaction in a three-dimensional honeycomb iridate: from ab-initio to spin model, January 2015. URL <http://arxiv.org/abs/1502.00006>. Arxiv.org.
- [38] Ralph Skomski. *Simple Models of Magnetism*. Oxford Graduate Texts, 2008.
- [39] Stephen Blundell. *Magnetism in Condensed Matter*. Oxford University Press, 2001.
- [40] P. W. Anderson. Antiferromagnetism. Theory of superexchange interaction. *Phys. Rev.*, 79(2), 1950.
- [41] P.W. Anderson. New approach to the theory of superexchange interactions. *Phys. Rev.*, 115(1), 1959.
- [42] B. Doucot, M.V. Feigel'man, L.B. Ioffe, and A.S. Ioselevich. Protected qubits and Chern-Simons theories in Josephson junction arrays. *Phys. Rev. B*, 71(024505), 2005.
- [43] Julien Dorier, Federico Becca, and Frederic Mila. The quantum compass model on the square lattice. *Phys. Rev. B*, 72(024448), 2005.
- [44] B. J. Kim, H. Ohsumi, T. Komesu, S. Sakai, T. Morita, H. Takagi, and T. Arima. Phase-sensitive observation of a spin-orbital Mott state in  $\text{Sr}_2\text{IrO}_4$ . *Science*, 323(5919):1329–1332, 2009.

- [45] Xiangang Wan, Ari M. Turner, Ashvin Vishwanath, and Sergey Y. Savrasov. Topological semimetal and Fermi-arc surface states in the electronic structure of the pyrochlore iridates. *Phys. Rev. B*, 83(205101), 2011.
- [46] Atsuo Shitade, Hosho Katsura, Jan Kunes, Xiao-Liang Qi, Shou-Cheng Zhang, and Naoto Nagaosa. Quantum spin Hall effect in a transition metal oxide  $\text{Na}_2\text{IrO}_3$ . *Phys. Rev. Lett.*, 102(256403), 2009.
- [47] X. Liu, T. Berlijn, W. G. Yin, W. Ku, A. Tselik, Young-June Kim, H. Gretarsson, Yogesh Singh, P. Gegenwart, and J. P. Hill. Long-range magnetic ordering in  $\text{Na}_2\text{IrO}_3$ . *Phys. Rev. B*, 83(220403), 2011.
- [48] Feng Ye, Songxue Chi, Huibo Cao, Bryan C. Chakoumakos, Jaime A. Fernandez-Baca, Radu Custelcean, T. F. Qi, O. B. Korneta, and G. Cao. Direct evidence of a zigzag spin chain structure in the honeycomb lattice: A neutron and x-ray diffraction investigation of single crystal  $\text{Na}_2\text{IrO}_3$ . *Phys. Rev. B*, 85(180403), 2012.
- [49] G. Cao, T. F. Qi, L. Li, J. Terzic, V. S. Cao, S. J. Yuan, M. Tovar, G. Murthy, and Kaul R. K. Evolution of magnetism in the single-crystal honeycomb iridates  $(\text{Na}_{1-x}\text{Li}_x)_2\text{IrO}_3$ . *Phys. Rev. B*, 88(220414), 2013.
- [50] T. Takayama, A. Kato, R. Dinnebier, J. Nuss, H. Kono, L. S. I. Veiga, G. Fabbris, D. Haskel, and H. Takagi. Hyperhoneycomb iridate  $\beta\text{-Li}_2\text{IrO}_3$  as a platform for Kitaev magnetism. *Phys. Rev. Lett.*, 114(077202), 2015.
- [51] Matthew J. O'Malley, Henk Verweij, and Patrick M. Woodward. Structure and properties of ordered  $\text{Li}_2\text{IrO}_3$  and  $\text{Li}_2\text{PtO}_3$ . *J. Solid State Chem.*, 181(8): 1803–1809, 2008.
- [52] A. W. Joshi. *Elements of Group Theory for Physicists*. Wiley Eastern Limited, 1975.

- [53] A. Abragam and B. Bleaney. *Electron Paramagnetic Resonance of Transition Ions*. Oxford Classic Texts, 1970.
- [54] A. Migliori. Pulsed field data acquisition. Presentation.
- [55] B. Ramshaw. *Shubnikov-de Haas Measurements and the Spin Magnetic Moment of  $YBa_2Cu_3O_{6.59}$* . PhD thesis, The University of British Columbia, 2012.
- [56] C. Rossel, P. Bauer, D. Zech, J. Hofer, M. Willemin, and H. Keller. Active microlevers as miniature torque magnetometers. *Journal of Applied Physics*, 79(8166), 1996.
- [57] E. Ohmichi and T. Osada. Torque magnetometry in pulsed magnetic fields with use of a commercial microcantilever. *Review of Scientific Instruments*, 73(8):5, 2002.
- [58] J. Brugger, M. Despont, C. Rossel, H. Rothuizen, P. Vettiger, and M. Willemin. Microfabricated ultrasensitive piezoresistive cantilevers for torque magnetometry. *Sensors and Actuators*, 73:235–242, 1999.
- [59] N. W. Ashcroft and N. D. Mermin. *Solid State Physics*. Holt, 1976.
- [60] M. M. Atarawneh, C. H. Mielke, and J. S. Brooks. Proximity detector circuits: an alternative to tunnel diode oscillators for contactless measurements in pulsed magnetic field environments. *Review of Scientific Instruments*, 80(066104), 2009.
- [61] S. Ghannadzadeh, M. Coak, I. Franke, P. A. Goddard, J. Singleton, and J. L. Manson. Measurement of magnetic susceptibility in pulsed magnetic fields using a proximity detector oscillator. *Review of Scientific Instruments*, 82(113902), 2011.

- [62] National Science Foundation Division of Materials Research and the State of Florida. National high magnetic field laboratory, June 2015. URL <https://nationalmaglab.org/user-facilities/pulsed-field-facility>.
- [63] Yogesh Singh and P. Gegenwart. Antiferromagnetic Mott insulating state in single crystals of the honeycomb lattice material  $\text{Na}_2\text{IrO}_3$ . *Phys. Rev. B*, 82(064412), 2010.
- [64] P.A. Goddard, J. Singleton, P. Sengupta, R.D. McDonald, T. Lancaster, S.J. Blundell, F.L. Pratt, S. Cox, N. Harrison, J.L. Manson, H.I. Southerland, and J.A. Schlueter. Experimentally determining the exchange parameters of quasi-two-dimensional Heisenberg magnets. *New J. Phys.*, 10(083025), 2008.
- [65] T. Lancaster, P. A. Goddard, S. J. Blundell, F. R. Foronda, S. Ghannadzadeh, J. S. Moller, P. J. Baker, F. L. Pratt, C. Baines, L. Huang, J. Wosnitza, R. D. McDonald, K. A. Modic, J. Singleton, C. V. Topping, T. A. W. Beale, F. Xiao, J. A. Schlueter, A. M. Barton, R. D. Cabrera, K. E. Carreiro, H. E. Tran, and J. L. Manson. Controlling magnetic order and quantum disorder in molecule-based magnets. *Phys. Rev. Lett.*, 112(207201), 2014.
- [66] T. Giamarchi. *Quantum physics in one dimension*. Oxford University Press, 2004.
- [67] Suchitra E. Sebastian. *Bose-Einstein condensation in spin dimer compounds*. PhD thesis, Stanford University, 2006.
- [68] T. Giamarchi and A. M. Tsvelik. Coupled ladders in a magnetic field. *Phys. Rev. B*, 59(17), 1999.
- [69] F. Mila. Ladders in a magnetic field: a strong coupling approach. *Eur. Phys. J. B*, 6(201), 1998.

- [70] T. Holstein and H. Primakoff. Field dependence of the intrinsic domain magnetization of a ferromagnet. *Phys. Rev.*, 58(1098), 1940.
- [71] M. Jaime, V. F. Correa, N. Harrison, C. D. Baptista, N. Kawashima, Y. Kazuma, G. A. Jorge, R. Stern, I. Heinmaa, S. A. Zvyagin, Y. Sasago, and K. Uchinokura. Magnetic-field-induced condensation of triplons in Han purple pigment  $\text{BaCuSi}_2\text{O}_6$ . *Phys. Rev. Lett.*, 93(8), 2004.
- [72] Paul A. Goddard, Jamie L. Manson, John Singleton, Isabel Franke, Tom Lancaster, Andrew J. Steele, Stephen J. Blundell, Christopher Baines, Francis L. Pratt, Ross D McDonald, Oscar E. Ayala-Valenzuela, Jordan F. Corbey, Heather I. Southerland, Pinaki Sengupta, and John A. Schlueter. Dimensionality selection in a molecule-based magnet. *Phys. Rev. Lett.*, 108(077208), 2012.